

Development of a PET-based Theranostic for Drug-Resistant BRAF^{V600E} Melanoma

by

Michael C. Bellavia

Bachelor of Science in Bioengineering, Binghamton University, 2013

Master of Science in Biomedical Engineering, Georgia Institute of Technology and Emory
University, 2018

Submitted to the Graduate Faculty of the
Swanson School of Engineering in partial fulfillment
of the requirements for the degree of
Doctor of Philosophy

University of Pittsburgh

2023

UNIVERSITY OF PITTSBURGH

SWANSON SCHOOL OF ENGINEERING

This dissertation was presented

by

Michael C. Bellavia

It was defended on

March 21, 2023

and approved by

Bryan N. Brown PhD, Associate Professor, Departments of Bioengineering, Obstetrics,
Gynecology, and Reproductive Services, and Clinical and Translational Science Institute

Joshua T. Mattila PhD, Assistant Professor, Department of Infectious Diseases and Microbiology
and Center for Vaccine Research, School of Public Health

Ravi B. Patel MD PhD, Assistant Professor, Departments of Bioengineering and Radiation
Oncology

Partha Roy PhD, Professor, Departments of Bioengineering and Pathology

Walter J. Storkus PhD, Professor, Departments of Dermatology and Immunology, School of
Medicine

Dissertation Director: Carolyn J. Anderson PhD, Professor, Departments of Chemistry and
Radiology, University of Missouri and Departments of Bioengineering, Medicine, and
Radiology, University of Pittsburgh

Copyright © by Michael C. Bellavia

2023

Development of a PET-based Theranostic for Drug-Resistant BRAF^{V600E} Melanoma

Michael C. Bellavia, PhD

University of Pittsburgh, 2023

Targeted radiopharmaceutical therapy (TRT) involving systemic administration of a tumor-selective agent labeled with a radionuclide has demonstrated considerable promise for cancer treatment, gaining traction recently with FDA approval of two agents since 2018. TRT agents bind tumor targets or accumulate within them, reducing toxicity to healthy cells relative to traditional external beam radiation therapy and allowing dose delivery to distant metastases. The radionuclides generate emissions that are both cytotoxic and suitable for non-invasive nuclear medicine imaging and/or have a diagnostic imaging/therapy isotope partner (“theranostic pair”), which allows pretherapy imaging to facilitate patient-individualized dosing. Current standard of care TRT is given with a fixed dosing regimen, despite evidence that individualization may improve outcomes. Combined TRT and immune checkpoint immunotherapy (ICI) has demonstrated remarkable responses even in poorly immunogenic tumors both preclinically and in patients. In ICI-resistant mouse models, an optimal low-dose TRT range was determined from subject-specific dosimetry for combined TRT + ICI that led to complete tumor regression in most mice.

Here, I aimed to translate positron-emission tomography (PET) for image-guided TRT in a clinically relevant BRAF-mutant mouse melanoma model. This mutation is druggable, but resistance develops rapidly. Combining this therapy with ICI may provide only modest benefit, and patients experiencing tumor progression have no reliable alternatives. I labeled the very late antigen (VLA-4) targeted LLP2A tracer with copper-64 for PET imaging (⁶⁴Cu-LLP2A) and

observed target-selective binding and internalization *in vitro*, as well as robust tumor uptake and retention *in vivo*. From longitudinal ^{64}Cu -LLP2A imaging in this model, subject- and timepoint-specific image segmentation of the tumor and other organs of interest were input into a Monte Carlo dosimetry software to predict absorbed doses with the corresponding therapy isotope, copper-67 (^{67}Cu -LLP2A). The tumor was predicted to receive significantly more ^{67}Cu dose than any other tissue, including the often dose-limiting kidneys. Predicted tumor dose per injected activity guided selection of two ^{67}Cu -LLP2A dose tiers for a therapy study in combination with dual ICI. Although the higher TRT dose and dual ICI showed the greatest benefit, the paradoxical benefit of the saline control versus all other remaining treatments necessitates replication and further scrutiny.

Table of Contents

Preface.....	xv
1.0 Introduction.....	1
1.1 Targeted Radiopharmaceutical Therapy (TRT).....	3
1.1.1 Radioimmunotherapy (RIT).....	9
1.1.2 Small Molecule Peptide TRT.....	13
1.1.2.1 ¹⁷⁷Lu-DOTATATE (Lutathera®).....	13
1.1.2.2 ¹⁷⁷Lu-PSMA-617 (Pluvicto®).....	16
1.1.2.3 LLP2A.....	18
1.2 ICI Therapy and Combination with ICI.....	20
1.2.1 Preclinical Studies of TRT + ICI.....	25
1.2.1.1 Antibody and Antibody Fragment TRT + ICI.....	25
1.2.1.2 Small Molecule Peptide TRT + ICI.....	26
1.2.1.3 Non-Peptide Small Molecule TRT + ICI.....	26
1.2.2 TRT Sensitizes ‘Cold’ Tumors to ICI.....	27
1.2.3 Clinical Trials of TRT + ICI.....	28
1.2.3.1 ¹⁷⁷Lu-DOTATATE (Lutathera®) + ICI.....	30
1.2.3.2 ¹⁷⁷Lu-PSMA-617 (Pluvicto®) + ICI.....	31
1.2.3.3 ²²³RaCl₂ (Xofigo®) + ICI.....	32
1.3 Radionuclide Dosimetry Towards Patient-Tailored TRT.....	32
1.3.1 Overview of Radionuclide Dosimetry.....	32
1.3.2 MIRD Dosimetry Formalism.....	35

1.3.3 Approaches to TRT Dosimetry	38
1.3.4 Phantom (OLINDA) vs Radiation Transport Dosimetry (ex. Torch).....	41
1.3.5 Radiation Dosimetry Software Packages	42
1.3.5.1 GE Dosimetry Toolkit and Q.Thera AI (GE Healthcare).....	42
1.3.5.2 MIM Software	43
1.3.5.3 PLANET Dose (DOSIsoft)	44
1.3.5.4 PMOD (PMOD Technologies LLC).....	45
1.3.5.5 Rapid.....	46
1.3.5.6 Torch (Voximetry Inc)	47
1.4 Motivation and Specific Aims.....	48
1.4.1 Specific Aim 1	50
1.4.2 Specific Aim 2	51
2.0 Specific Aim 1: Validate differential ^{64}Cu-LLP2A uptake and PET signal in BRAF^{V600E} mouse melanoma models that vary in VLA-4 expression.....	52
2.1 Introduction	52
2.2 Materials and Methods	54
2.2.1 Cell Line Generation.....	54
2.2.2 Peptide Synthesis and Radiolabeling.....	55
2.2.3 Flow Cytometry Validation of Cy3-LLP2A.....	55
2.2.4 Cell Binding Assays.....	56
2.2.5 ^{64}Cu -LLP2A Internalization Assays	57
2.2.6 Animal Studies.....	57
2.2.7 PET/CT Imaging and Analysis	58

2.2.8 Biodistribution Experiments	58
2.2.9 Statistics	59
2.3 Results.....	59
2.3.1 Generation of BPR α and Flow Cytometry Validation of Cy3-LLP2A	59
2.3.2 Radiolabeling Chemistry	61
2.3.3 ⁶⁴ Cu-LLP2A Cell Binding Assays in BPR and BPR α Cells.....	62
2.3.4 Internalization of ⁶⁴ Cu-LLP2A in BPR and BPR α Cells.....	63
2.3.5 Biodistribution of ⁶⁴ Cu-LLP2A in BPR and BPR α Tumor Models.....	64
2.3.6 PET/CT Imaging of BPR and BPR α Tumor Models.....	66
2.4 Discussion	67
3.0 Specific Aim 2: Compare therapeutic efficacy of ⁶⁷ Cu-LLP2A TRT + dual ICI at two TRT dose levels informed from ⁶⁴ Cu-LLP2A PET/CT imaging and evaluate TRT toxicity.....	71
3.1 Introduction	71
3.2 Materials and Methods	73
3.2.1 BPR α Tumor Model.....	73
3.2.2 PET/CT Imaging and Contouring of BPR α Tumors.....	73
3.2.3 Dosimetry Calculations.....	75
3.2.4 Copper-67 Radiolabeling of TE1A1P-LLP2A.....	76
3.2.5 ⁶⁷ Cu-LLP2A Biodistribution	76
3.2.6 Therapy Study Treatments and Timeline.....	76
3.2.7 Toxicity Evaluation	77
3.2.8 Statistics	78

3.3 Results.....	78
3.3.1 ⁶⁷Cu-LLP2A Dosimetry and Biodistribution Studies.....	78
3.3.2 Comparison of Subject-Specific and Phantom-Based ⁶⁷Cu-LLP2A Dosimetry	80
3.3.3 ⁶⁷Cu-LLP2A + Dual ICI Therapy in Subcutaneous BPRα Model.....	82
3.3.4 Sex Differences in Response to ⁶⁷Cu-LLP2A TRT + ICI Treatments.....	86
3.3.5 Toxicity of ⁶⁷Cu-LLP2A + Dual ICI Treatments	87
3.4 Discussion	89
4.0 Summary and Future Directions.....	92
4.1 Overall Summary	92
4.2 Summary of Challenges and Limitations	95
4.3 Future Directions.....	97
Appendix A ⁶⁴Cu-LLP2A Imaging in BPR and BPRα Tumor Models.....	100
Appendix A.1 Materials and Methods.....	100
Appendix A.1.1 Reagents.....	100
Appendix A.1.2 Instrumentation	100
Appendix A.1.3 Radio-HPLC Procedure.....	101
Appendix A.1.4 Bichinchoninic Acid (BCA) Procedure for Protein Quantification	101
Appendix A.2 Results	102
Appendix A.2.1 Control Conditions of ⁶⁴Cu-LLP2A Internalization Experiment	102
Appendix A.2.2 Biodistribution Timecourse in BPRα Tumors.....	103

Appendix A.2.3 Comparison of ⁶⁴ Cu-LLP2A Tumor-to-Muscle Standard Uptake Value Ratios in BPR α versus Previously Reported Values for B16F10.....	105
Appendix B Image-Guided ^{64/67} Cu-LLP2A Therapy in BPR α	106
Appendix B.1 Materials and Methods.....	106
Appendix B.1.1 Reagents.....	106
Appendix B.1.2 Instrumentation	106
Appendix B.1.3 Processing of PET/CT Images in VivoQuant.....	107
Appendix B.1.4 Contouring Rules	107
Appendix B.1.5 Torch Analysis Procedure.....	109
Appendix B.1.6 Mean Dose Rate Integration	109
Appendix B.1.7 Radio-HPLC Procedure for ⁶⁷ Cu-LLP2A	110
Appendix B.2 Results	111
Appendix B.2.1 Characteristics of imaging test mice	111
Appendix B.2.2 Activity Concentration of ⁶⁴ Cu-LLP2A in Test Mice ROIs.....	111
Appendix B.2.3 Mean ⁶⁷ Cu-LLP2A Absorbed Dose Comparison of Torch and OLINDA in Test Mice.....	113
Appendix B.2.4 Organ Masses in Torch and OLINDA.....	115
Appendix B.2.5 Copper-67 Radiolabeling of LLP2A	115
Appendix B.2.6 Comparison of ^{64/67} Cu-LLP2A Biodistribution and Torch Dosimetry	116
Bibliography	118

List of Tables

Table 1 List of FDA-approved TRT agents and their key characteristics	5
Table 2 Prescribed activity for 2 Gy tumor dose for each mouse from OLINDA and Torch	81
Table 3 Comparison of ROI prescribed mean doses \pm standard deviation (SD) for the OLINDA MOBY phantom and Torch.....	82
Table 4 <i>Ex vivo</i> biodistribution values for ^{64}Cu-LLP2A in mice bearing BPRα tumors at 4, 24, and 48h post-injection.	104
Table 5 Comparison of ^{64}Cu-LLP2A tumor-to-muscle standard uptake value ratios in mice bearing syngeneic B16F10 or BPRα tumors at 4 and 24h post-injection	105
Table 6 Contouring Rules for each ROI.....	108
Table 7 Imaged mouse characteristics	111
Table 8 Averaged Torch ROI masses (g) compared to those of the 25g OLINDA MOBY phantom	115
Table 9 Comparison of $^{64/67}\text{Cu}$-LLP2A biodistribution results at 4, 24, and 48h post-injection.	117

List of Figures

Figure 1 Clinical TRT is generally given with a fixed regimen despite heterogeneous tumor burden among patients.....	2
Figure 2 Decay chains of medically relevant alpha emitters to stable isotopes.....	8
Figure 3 Characteristics and relative DNA damage inflicted by each therapeutic particle type	9
Figure 4 Characteristics of common RIT vectors	12
Figure 5 Molecular structure and amino acid composition of ¹⁷⁷Lu-DOTATATE and PRRT mechanism of action.	15
Figure 6 Molecular structure of PSMA-617 and generalized PSMA inhibitor interaction with PSMA receptor.....	17
Figure 7 Molecular structure of ⁶⁴Cu-CB-TE1A1P-LLP2A (⁶⁴Cu-LLP2A) and <i>in vivo</i> performance.....	19
Figure 8 T cell activation, regulation, and reactivation following ICI therapy	21
Figure 9 TRT and ICI synergize via immune mechanisms.....	24
Figure 10 TRT sensitizes 'cold' murine tumor models to ICI	28
Figure 11 Dramatic improvement in a patient refractory to anti-PD-L1 (avelumab) receiving a single off-label dose of ¹⁷⁷Lu-DOTATATE for heavily metastatic Merkel cell carcinoma and resuming avelumab	29
Figure 12 Dosimetry scheme for radiopharmaceutical imaging agents	36
Figure 13 Generalized framework for TRT dosimetry from patient images.....	38

Figure 14 Hypothetical per-cycle dosimetry scheme for ^{177}Lu -DOTATATE NET treatment	39
Figure 15 Molecular structure of Cy3-PEG ₄ -LLP2A, the fluorescent counterpart to ^{64}Cu -LLP2A.....	55
Figure 16 BPR α cell selection by flow cytometry.....	60
Figure 17 Cy3-LLP2A staining of BPR and BPR α cells by flow cytometry.....	61
Figure 18 Radio-HPLC chromatogram of ^{64}Cu -LLP2A.....	62
Figure 19 Saturation binding data of ^{64}Cu -LLP2A in BPR α and BPR cells.....	63
Figure 20 VLA-4 expression is required for ^{64}Cu -LLP2A internalization.....	64
Figure 21 Biodistribution of ^{64}Cu -LLP2A in mice bearing BPR and BPR α tumors at 24h post-injection	65
Figure 22 Representative ^{64}Cu -LLP2A PET images and image quantification in subcutaneous BPR and BPR α tumor models	66
Figure 23 Screenshot of tumor and organ ROIs drawn in VivoQuant 2021, indicated by color	74
Figure 24 BPR α therapy study treatments and timeline.....	77
Figure 25 Representative timecourse of ^{64}Cu -LLP2A in BPR α tumor model	79
Figure 26 Comparison of ^{67}Cu -LLP2A dosimetry and biodistribution results.....	80
Figure 27 Tumor growth curves and survival for all treatment groups.....	84
Figure 28 Median survival and relevant survival curve pairings for treatment groups.....	85
Figure 29 Tumor growth curves from the ^{67}Cu -LLP2A TRT + ICI therapy study color-coded by mouse sex	86
Figure 30 Survival curves per treatment group plotted according to sex	87

Figure 31 Metrics of hematological toxicity in therapy study mice 88

Figure 32 Timecourse of ⁶⁴Cu-LLP2A activity (counts per minute) internalization for all conditions tested in BPR, BPR α , and B16F10 melanoma cells..... 103

Figure 33 Merged *ex vivo* biodistribution timecourse of ⁶⁴Cu-LLP2A in mice bearing BPR α tumors 104

Figure 34 Timecourse of ⁶⁴Cu-LLP2A in ROIs from imaging for each of the test mice (M1, M3, M4)..... 112

Figure 35 Absorbed ⁶⁷Cu-LLP2A doses in ROIs shared between Torch and the OLINDA MOBY 25g digital phantom for each of the test mice 114

Figure 36 Representative radio-HPLC trace of ⁶⁷Cu-LLP2A 116

Figure 37 Combined ^{64/67}Cu-LLP2A biodistribution assays and predicted ⁶⁷Cu-LLP2A dosimetry 117

Preface

My PhD journey was certainly not what I anticipated when I began my graduate studies in 2014. I started my PhD at the Georgia Institute of Technology looking to study biomaterials for cancer immunotherapy, with the goal to graduate by 2020 at the latest. Clearly that's not what happened, but for all the disappointment and pivots of the meandering path it has made me a more resilient and capable person and scientist. This is the culmination of a journey of more than 8 years, 4 universities, and 2,500 miles. Along the way I've been fortunate to meet so many warm, helpful, and talented people – many of whom I am blessed to call friends.

First, I want to thank my advisor, Dr. Carolyn Anderson. She gave me a chance despite my limited knowledge of chemistry while I was still working to complete my Master's in an unrelated area. She always told me the truth and provided encouragement whenever needed. She allowed me to take big but calculated risks to pursue my own scientific interests within this project. I came within inches of quitting when she left Pitt for the University of Missouri in April 2020, but stayed in the program at her urging. It was among the best decisions I've made in my life.

I am deeply grateful to the past members of the Anderson and Dr. Barry Edwards' labs as well as the current members of the In Vivo Imaging Facility under Dr. Jessie Nedrow at Pitt. Thank you to former postdocs Dr. Lea Nyiranshuti, Dr. Caline Abadjian, Dr. Xiaoxi Ling, Dr. Shubhanchi Nigam, and Dr. Michael Pun for training me and for your mentorship. Thank you to Kate Day for performing the imaging, assisting with the mouse experiments, and answering my continuous questions about image handling and the analysis software. To Joe LaToche, thank you for your guidance in all things animal study related and for sharing awful YouTube music videos. Thank you to Philip Mannes for your friendship, technical expertise, and solidarity. To Dr. Anders

Josefsson, thank you for conducting the OLINDA analysis and for helping to demystify radionuclide dosimetry.

I was fortunate to be pushed further with my scientific training and to get some understanding of the clinical perspective under the guidance of Dr. Ravi Patel following Carolyn's departure to Missouri. He urged me to think more systematically and to be fastidious in how I developed and supported my claims. Our interaction wasn't always smooth, but I know he wanted to help me grow to the highest caliber scientist I possibly could. He stayed awake until 5 am to help me complete an NIH F31 the night before the deadline. To enhance the significance and potential utility of my project, he introduced me to his former colleagues Dr. Joe Grudzinski and Dr. Ian Marsh at Voximetry, opening an entirely new avenue. This project is not half of what it is without his contributions. In the lab, I was able to continue working with Dr. Bob Edinger, who served as a third PI, confidant, and life coach.

Thank you to everyone at the University of Missouri Molecular Imaging and Theranostics Center (MITC). There's far too many of you to acknowledge individually, but just know that the "Welcome to the MITC family" written in the onboarding packet is more than just words to me. To Ejike Iweha, thank you for introducing me to an unexpected community in the Koinonia Soccer Club and for being my unauthorized hype man. To Claudia Chambers, thank you for lending an ear, for letting me borrow Buck/Betsy the Buick for an entire month while the Silver Bullet was out of order, and for being willing to inherit this project – looking forward to seeing where you take it. To Aidan Wirrick, thank you for your comedy, Gen Z-isms, and for helpful scientific discussions – I have no doubt you'll excel in this field. Lisa Watkinson, Terry Carmack, and Levi Strickland conducted the Aim 2 animal experiments and were instrumental in helping to make

them as comprehensive as possible. Thank you to Dr. Khanh-Van Ho for performing the saturation binding experiments with ^{64}Cu -LLP2A.

I am also grateful for the friendship and support I received in the lab of Dr. Todd Sulchek and others I met at the Georgia Institute of Technology. To Todd's Plan/the Toddlers, thank you for providing me an environment where I was able to regain my footing and finally learn to trust myself. The 6th (?) anniversary of the mis-cake has just passed, and I remember it fondly. In particular, I'd like to acknowledge Dr. Brandon Holt, Dr. Katie Young, Dr. Katily Ramirez, Kathryn Murray, Dr. Anna Liu, Dr. Aaron Enten, Dr. Nick Stone, and Dr. Betsy Campbell. I'm hopeful we can reconnect soon.

Thank you to friends both new and old for sustaining me in this adventure. My Binghamton friends have known of the ups and downs in this pursuit from my days of camping in the Bingham study lounge more than thirteen years ago: Rodrigo Caballero, Dr. Jon Jampel, Brian Jordan, Dan Trebach, Dr. Steve Lange, Ben Ramos, Shelby Lennon, Aly Jordan, and Elana Reiss. Special thank you to Dr. Josh Anbar for his endless encouragement and advice, especially as the end approached.

Lastly, I am incredibly fortunate to have the family I do. My parents, Kathy Jivoff and Charles Bellavia, were key sources of strength through the setbacks, and they did everything in their power and then some for me to realize this dream. Thank you to my stepmom Teresa Bellavia, who has also helped to guide me and mold me over the past 20 years into the man I am. Thank you to the Jivoff/Vincent/Watson and Rozen clans for your support and for taking an interest in my work. I dedicate this in part to the Jivoff family patriarch and matriarch, Dr. Leo and Natalie Jivoff, who inspired in me a wonder of science and a desire to care for others, respectively.

1.0 Introduction

Portions of this dissertation contain text and/or image reproduction from publications where I am the first author. Section 1.0 Introduction is related to a review article published in the Journal of Nuclear Medicine, Bellavia, M.C., Patel R.B., Anderson, C.J., "Combined Targeted Radiopharmaceutical Therapy and Immune Checkpoint Blockade: From Preclinical Advances to the Clinic", Copyright Society for Nuclear Medicine and Molecular Imaging [1]. Section 2.0 Specific Aim 1 is related to a research article from Bellavia et al 2022 in Molecular Imaging and Biology, "PET Imaging of VLA-4 in a New BRAF V600E Mouse Model of Melanoma", published 2021, Copyright Springer Nature [2].

Despite numerous treatment advances for metastatic cancers (chemotherapeutics, small molecule inhibitors, immune checkpoint inhibitors and combinations of these approaches), only a subset of patients benefit, and these improvements may be short-lived. External beam radiation therapy (EBRT) has been a mainstay of treatment for localized cancers for decades, where it induces catastrophic DNA damage in rapidly-proliferating cancer cells [3]. In addition to direct irradiation of DNA, ionization of water molecules in the tumor compartment generates free radicals that contribute the bulk of damage to DNA [4]. Recently, pairing EBRT and immune checkpoint inhibitors (ICI) has garnered considerable clinical interest as regression in non-irradiated metastases (the abscopal effect) has occurred in patients receiving this combined treatment [5-7]. However, EBRT is not suited to occult metastases and can damage nearby healthy tissue. Instead, there has been a growing effort to apply targeted radiopharmaceutical therapy (TRT) in metastatic cancers, in which a selective agent labeled with a radionuclide is administered systemically to destroy both the primary tumor and metastatic lesions. Recently, two such agents

have been approved by the United States Food and Drug Administration (FDA) and European Medicines Agency (EMA) - Lutathera® in 2017 and 2018 and Pluvicto™ in 2022.

In clinical practice, TRT is usually given with a fixed dosing regimen or scaled to patient weight/body surface area regardless of the individual patient's tumor burden or tumor uptake of the corresponding pretherapy imaging tracer (Figure 1) [8]. This is despite accumulating evidence that more tailored therapy may improve outcomes [9, 10]. As there is limited patient specificity, the dose given may result in toxicities or in undertreatment and/or the selection of TRT-resistant clones. Clinical TRT dosimetry, in which imaging is performed with a diagnostic companion radiopharmaceutical or with a subtherapeutic dose of the agent prior to TRT for individualizing patient therapy doses, is infrequently applied outside academic medical centers and may lack sensitivity [8].

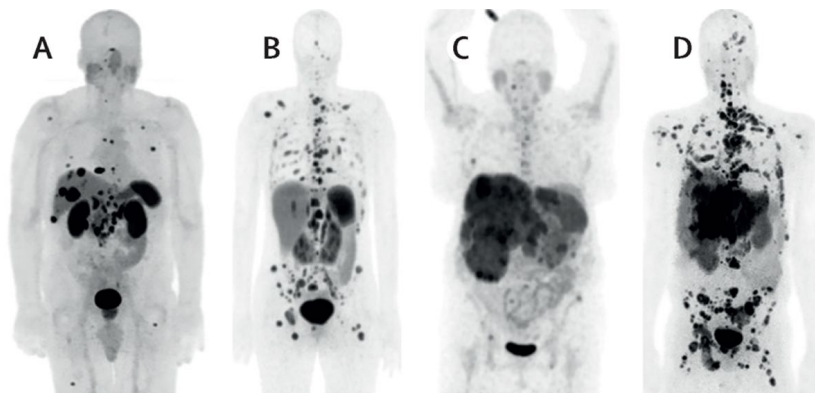


Figure 1 Pretreatment imaging indicates heterogenous tumor burden among these patients. Each was treated with a dose of 7.4 GBq lutetium-177-labeled DOTATATE (¹⁷⁷Lu-DOTATATE) TRT per cycle. Image reproduced from Lawhn-Heath et al., 2022.

This dissertation research applies the use of molecular imaging to inform radionuclide dosimetry towards dose selection for the same agent labeled with the corresponding therapy radioisotope. A tumor-targeting peptide was labeled with a positron-emitting radionuclide for positron emission tomography (PET) imaging in a novel subcutaneous mouse melanoma model

developed through the research described here. Dosimetry enabled by analysis of these PET images informed the dosing at several dose levels for the agent with the matched therapy radioisotope. To evaluate the promise of combined TRT determined via dosimetry and synergism with ICI, a therapy study was conducted. An overview of TRT, radionuclide dosimetry, and TRT with ICI applied both experimentally and in the clinic is presented to emphasize the value of this work.

1.1 Targeted Radiopharmaceutical Therapy (TRT)

Although low dose EBRT (2-3 Gy) can be administered safely to large fields or the whole body, it induces systemic lymphocyte depletion that may confound effective antitumor immunity [11]. Also, delivering higher targeted EBRT doses to multiple small tumors or micrometastatic disease may not be feasible. Given these drawbacks, systemic delivery of radiation with TRT via a peptide, antibody, or other ligand carrier targeted to a tumor receptor or antigen that accumulates due to the physiological features of a tumor may have distinct advantages over EBRT when there is known or potential metastatic disease. Cytotoxic radiation is delivered via the decay of the radionuclide coupled to these carriers and therefore its efficacy is much less reliant upon the disturbance of signaling pathways, as in the case of biologics, which frequently fail in clinical trials [12]. Although advancements have been made in novel chemotherapeutics, small molecule inhibitors, biologics, ICIs, and their combination, the outlook for patients with metastatic disease remains poor. Relative to many systemic cancer treatments, TRT provides therapeutic benefit with less toxicity [13]. Responses may be observed after the first or after several injections, whereas chemotherapy may require many cycles given over months [14]. Additionally, side effects from

TRT are typically milder. Further, certain TRT radionuclides have emissions suitable for nuclear medicine imaging, such as single photon emission computed tomography (SPECT). Some TRT radionuclides possess a diagnostic partner radionuclide with emissions suitable for much more sensitive positron emission tomography (PET) imaging (ex. copper-64 PET/copper-67 TRT). Apart from the number of neutrons in the nucleus, the radionuclides are chemically identical such that the same tracer labeled with either should have similar binding affinity and biodistribution, allowing for personalized TRT dosing from imaging (dosimetry), in a so-called ‘theranostic’ approach. A host of TRT agents are currently in use clinically having received FDA approval (Table 1), many of which will be discussed in detail in the sections that follow.

Radiation emitted in the context of TRT falls into three major classes: photons, electrons, and α -particles. Photons may be in the form of X-rays or γ -rays, which are apt to image TRT dissemination but do not direct radiation adequately to target cells [14]. Although their definition varies by discipline, γ -rays are generally of higher energy than X-rays (≥ 100 keV), and originate in the nucleus, whereas X-rays originate from orbital electron transitions or are machine-generated. Machine-generated X-rays are utilized for computed tomography (CT) to provide anatomical reference in nuclear imaging. Photon emission energies within 100-200 keV are ideal for imaging with γ -cameras and for SPECT [14]. Some radionuclides used for paired diagnostics with TRT also emit positrons (β^+ decay), the antiparticle of the electron. The annihilation event resulting from their meeting causes the characteristic emission of 511 keV photons detected by PET cameras that are used to reconstruct a 3D rendering of the activity distribution.

Cytotoxic TRT electron emissions consist mainly of β particles (high energy electrons, β^- decay) and low energy (Auger) electrons, which in certain radionuclides occur together. β particles are the most common emission type amongst TRT agents, and these are electrons originating from

Table 1 List of FDA-approved TRT agents and their key characteristics

TRT Agent	Indication	Mechanism of Action	Manufacturer (Current)	Year Approved
Iodine-131 sodium iodide (Hicon®)	Thyroid cancer	Active uptake into thyroid gland via Na-I symporter, β^- -emitter	Jubilant Radiopharma	1971
Samarium-153-labeled lexidronam (Quadramet®)	Cancer-related bone pain	Chelated ^{153}Sm , binds hydroxyapatite matrix of bone, β^- -emitter	Lantheus	1997*
Iodine-131-labeled anti-CD20 (Zevalin®)	Non-Hodgkin's lymphoma	Binds to CD20 on malignant B cells, β^- -emitter	Acrotech Biopharma	2002
Yttrium-90-labeled anti-CD20 (Bexxar®)	Non-Hodgkin's lymphoma	Binds to CD20 on malignant B cells, β^- -emitter	GlaxoSmithKline	2003*
Radium-223 dichloride (Xofigo®)	Bone metastases (metastatic prostate cancer)	Calcium mimetic absorbed by remodeling bone, α -emitter	Bayer	2013
Lutetium-177-labeled DOTATATE (Lutathera®)	Neuroendocrine tumors	Peptide binds to somatostatin receptors, β^- -emitter	Novartis	2018
Iodine-131-labeled iobenguane (Azedra®)	Adrenal gland tumors	Small molecule analogue of adrenaline, active uptake by adrenaline transporter, β^- -emitter	Lantheus	2020
Lutetium-177-labeled PSMA-617 (Pluvicto®)	Metastatic castration-resistant prostate cancer	Small molecule inhibitor of prostate specific membrane antigen (PSMA), β^- -emitter	Novartis	2022

*Discontinued due to market considerations (Bexxar® in 2014 and Quadramet® in 2021)

the nucleus [14]. β -emitters are the most widely available, and many of these emit photons suitable for γ imaging and SPECT. β -emitters such as yttrium-90, lutetium-177, and samarium-153 have been utilized over the past several decades, with iodine-131 for thyroid cancer introduced in the 1930s. Lutetium-177 has gained widespread appeal as it emits γ photons of 100-200 keV [15], possesses a half-life suitable for both peptide and antibody pharmacokinetics, and is reactor produced by carrier-added ($^{176}\text{Lu}(n, g)^{177}\text{Lu}$) and no-carrier-added ($^{176}\text{Yb}(n, g)^{177}\text{Yb} \rightarrow ^{177}\text{Lu}$) methods such that it is more readily available [16]. Other β -emitting radionuclides with advantages over Lu-177 are currently under study (ex. copper-67, terbium-161). However, barriers to translation of new radionuclides include challenging radiochemistry, difficulties in isotope production in part due to high cost, and the lack of commercial incentive to overcome the necessary regulatory obstacles involved [17]. Auger electrons are ejected upon suborbital transitions and are of short range according to their emission energy. Preclinical TRT with Auger emitters iodine-125 [18] and indium-111 [19] has shown promise, especially when in proximity to the cell nucleus or incorporated into DNA. Although few clinical studies have been conducted, particularly recently, results have demonstrated proof-of-concept towards further evaluation [20].

Alpha (α) particles are composed of two protons and two neutrons (a helium nucleus) emitted from the nucleus of the radionuclide, and these decay with much greater energy than electrons, leading to substantially more damage. These particles inflict numerous and generally irreparable DNA double-strand breaks. Cytotoxic effect can be achieved with only 1-20 α -particles crossing through the cell nucleus, and it is the number of crossing events that dictates absorbed dose [14]. This contrasts with β -emitters, which predominantly cause single-strand DNA breaks and as a result have 500-fold lower cytotoxic potential [21]. Given their short range,

toxicity to healthy tissue is limited. However, emission of the α particle imparts recoil energy to the daughter atom that far surpasses the binding energy of the strongest chemical bonds, freeing the isotope from the targeting vector [22]. The subsequent decay chain frequently results in the creation of further α - and β -emitting progeny, leading to untargeted irradiation of nearby tissues (Figure 2). This daughter redistribution is a highly complex process affected by the distance traversed during the recoil process, diffusion, and active transport as well as inherent affinity of the radionuclide for particular organs. As such, normal organ toxicity and the time needed to reach target cells are related to the half-life ($t_{1/2}$) of the daughter radionuclide. Therefore, a useful α radionuclide has a sufficiently long half-life to allow for production, radiolabeling, and preparation for administration to a patient, but its half-life, and that of any of its daughter decay products, must not be too long so that surplus dose is avoided. Also, γ emissions arising during the decay chain are of interest for imaging. Alpha particle emitters for TRT have been investigated since the early 1980s, and eight are considered medically relevant: actinium-225, astatine-211, bismuth-212, bismuth-213, lead-212, radium-223, terbium-149, and thorium-227. Unconjugated radium-223 (radium-223 dichloride, Xofigo®, Bayer) received FDA approval in May 2013 for castration-resistant prostate cancer that had metastasized to bone, an indication for which there were no effective treatments at the time [23]. Clinical trial results were impressive [23], sparking rekindled interest in α TRT; from 2008 to 2018, the number of PubMed listed studies utilizing α -emitters increased nearly sixfold [14].

TRT bound to adjacent cells [26]. As such, these are less likely to effectively target small tumor cell clusters or circulating tumor cells. However, recent preclinical evidence for the efficacy of α -emitters in bulky tumors challenges this view [27]. The two peptide TRT ligands that recently received regulatory approval utilize the β -emitter lutetium-177 - ^{177}Lu -DOTATATE (Lutathera®) to treat neuroendocrine tumors (NETs) and ^{177}Lu -PSMA-617 (Pluvicto™) for metastatic castration-resistant prostate cancer (mCRPC).

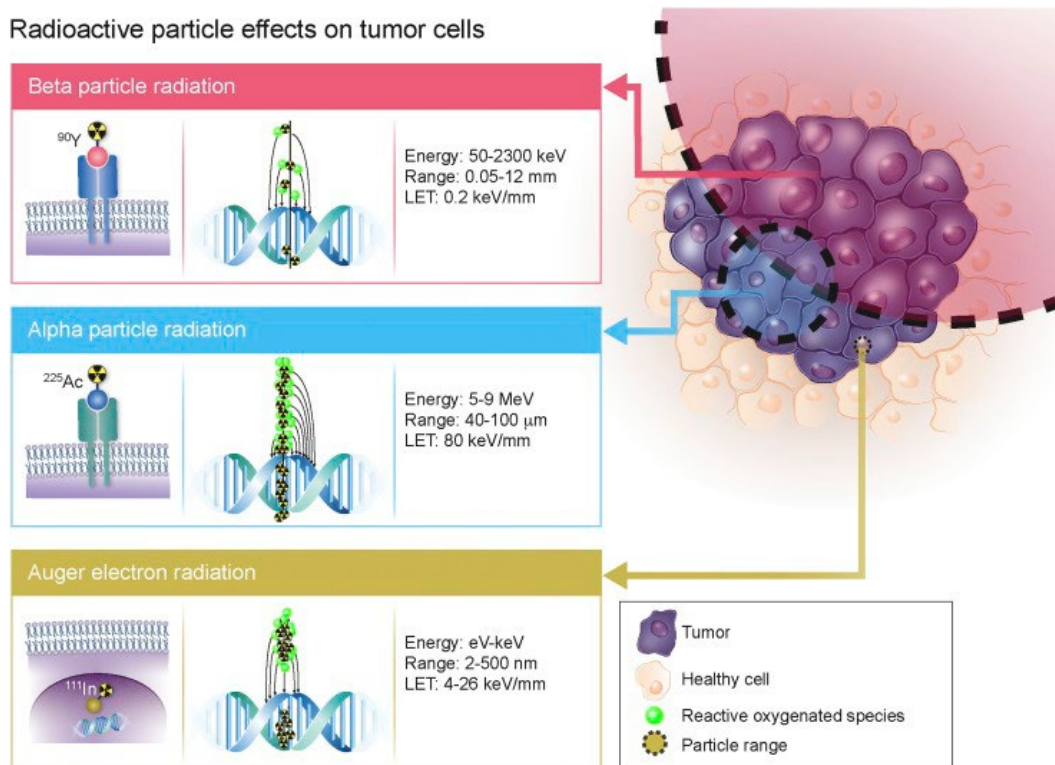


Figure 3 Characteristics and relative DNA damage inflicted by each therapeutic particle type. Image reproduced from Poty et al, 2018.

1.1.1 Radioimmunotherapy (RIT)

Monoclonal antibodies have been employed therapeutically in the clinic for more than 35 years, with nearly 100 approved by the FDA for both cancer and other indications [28]. As

monoclonal antibodies bind with high affinity and selectivity to their epitope, may prompt internalization of the bound antibody-antigen complex, and have wide commercial availability, they have been extensively implemented for TRT ('radioimmunotherapy', RIT). These are 150 kDa proteins almost entirely of the immunoglobulin G (IgG) class, which are cleared via the liver and reticuloendothelial system [14]. Maximum tumor accumulation and blood clearance is typically not achieved until 5-10 d post-injection [29]. As such, longer-lived radionuclides (lutetium-177, $t_{1/2}$: 6.7 d, iodine-131, $t_{1/2}$: 8 d, actinium-225, $t_{1/2}$: 9.9 d) may be optimal to deliver a therapeutic dose. To date, the most striking RIT benefit is in hematological malignancies, as these exist in the blood pool, where the RIT is administered, and the cancerous cells are vulnerable to radiation [28]. Two monoclonal antibody RIT agents that bind CD20 on B cells were approved by the FDA for relapsed, refractory non-Hodgkin lymphoma, both labeled with β -emitters: ^{90}Y -ibritumomab tiuxetan (Zevalin®) in 2002 and ^{131}I -tositumomab (Bexxar®) in 2003. In a landmark clinical trial, Zevalin® demonstrated significant improvement in overall response rate (80% vs 56%) and complete response rate (30% vs 16%) relative to the standard of care rituximab (chimeric anti-CD20 monoclonal antibody), with durable responses [30]. Results with Bexxar® were even more remarkable, with an overall response rate of 95% and a complete response rate of 75% [31]. Despite these successes, use of both agents continuously declined beginning shortly after approval due to difficulties with insurance reimbursement in the United States and logistical challenges, among other issues [32]. Zevalin® is administered rarely and Bexxar® was discontinued in 2014 as a cost-savings measure.

Development of RIT for solid tumors has been more incremental due to numerous tumor features that act as barriers to delivery. These antibodies must extravasate through leaky vasculature and then diffuse against an inhospitable interstitial fluid pressure gradient [33]. Given

that the tumor is antigen-positive, distribution of the antibody will be heterogenous, with higher antigen at the periphery reducing the amount that accumulates in the center of the lesion ('binding site barrier' effect) [34]. Also, a much larger absorbed dose is required for the treatment of solid tumors (50-80 Gy vs 3 Gy for certain lymphomas) [35]. Due to the long circulation time of full-length antibodies (serum half-life of 1-3 weeks [28]), non-target tissues may receive substantial radiation doses.

To mitigate toxicity and increase tumor dose delivery with intact antibodies, 'pre-targeting' (pRIT) strategies that separate the administration of the antibody and radionuclide have been investigated both preclinically and clinically [29, 36]. First, a non-radiolabeled antibody is injected that both binds the antigen of interest and is bound by a particular radionuclide conjugate. The antibody is then allowed to clear from non-specific sites prior to injection of the radionuclide conjugate. Earlier work employed the high affinity biotin-avidin pair or a bispecific antibody – radiolabeled complementary hapten (non-immunogenic antigen) [37]. However, immunogenicity can occur with both approaches [37, 38]. More recently, pRIT utilizing highly selective and rapid *in vivo* 'click' chemistry has gained traction. An antibody labeled with trans-cyclooctene (TCO) is administered and given sufficient time to home to the tumor and clear from blood and non-target organs, followed by a tetrazine (Tz)-radionuclide conjugate. When the Tz-radionuclide encounters bound TCO-antibody, an *in situ* ligation proceeds rapidly such that unbound Tz-radionuclide is quickly cleared. Substantial improvements in tumor dose delivery with reduced blood toxicity have been achieved. Keinänen et al demonstrated dose-dependent tumor response and survival (up to 1.5 mCi administered) with recoverable blood toxicities using a dual imaging/therapy ^{64/67}Cu pRIT system in colorectal cancer xenografts [29].

Alternatively, radiolabeled antibody fragments may be utilized. Full-length antibodies may be enzymatically cleaved to form F(ab')₂ (both antigen-binding regions only, ≈ 110 kDa) or Fab (single antigen-binding region only, 50-55 kDa) fragments [28]. Antibody fragments can also be genetically engineered, such as scFv or scFv-Fc (fusion protein of antigen-binding regions without or with Fc region for immune effector function, 28 kDa or 105 kDa), minibodies (connected pair of single chains responsible for antigen binding, 80 kDa), diabodies (dimer of two different antigen-binding chains, 55 kDa), or single domain antibodies (sdabs/nanobodies, single chain binding domain, 12-15 kDa) (Figure 4). Smaller fragments (< 55 kDa) exhibit accelerated tumor penetration due to higher diffusivity, albeit at the expense of lower tumor uptake due to more rapid blood clearance. Those > 40 kDa are able to extravasate into the tumor via the aberrant tumor vasculature independent of the target and accumulate (the enhanced permeability and retention effect, EPR), but the EPR effect does not necessarily improve RIT efficacy [39]. However, antibody fragments of molecular weight < 60 kDa clear primarily through the kidney, which can result in renal toxicity [28]. RIT diffusivity is also influenced by the extracellular matrix, namely the local concentration of collagen [39]. Antibody fragment RIT has demonstrated mixed results [28], which suggests that an RIT vector must be thoroughly characterized in preclinical models to determine the most well-suited tumor model and dosing.









	Enzymatic			Engineered					
									
Format	Intact	F(ab') ₂	Fab	scFv-Fc	Minibody	Diabody	scFv	Nanobody	
MW (kDa)	150	110	55	105	80	55	28	12-15	
Valency	Divalent	Bivalent	Monovalent	Bivalent	Bivalent	Bivalent	Monovalent	Monovalent	
Serum Half-life	1-3 weeks	8-10 h	12-20 h	8-80 h (Terminal)	5-10 h	5-6 h	2-4 h	0.5-1 h	
Clearance Route	Liver	Liver, Kidney	Kidney	Liver	Liver	Kidney	Kidney	Kidney	

Figure 4 Characteristics of common RIT vectors. Image adapted from White et al, 2021.

1.1.2 Small Molecule Peptide TRT

There has been recent interest in developing peptide TRT agents due to their greater solid tumor penetration and lower capacity for immunogenicity relative to antibodies or antibody fragments [40]. Additionally, peptide/peptidomimetic synthesis is generally straightforward and these molecules can be designed to resist proteolysis with the inclusion of unnatural or D amino acids [41]. Lutathera® to target somatostatin receptor subtype 2 (SSTr2) was the first peptide TRT agent to be FDA approved in 2018. These agents are selected to target overexpressed surface antigens particular to or found across multiple tumor histologies. For example, the targeting of receptors overexpressed in malignancy and that facilitate angiogenesis (integrin $\alpha_v\beta_3$) and/or metastatic spread (integrin $\alpha_4\beta_1$ /VLA-4) has received increased interest [42, 43]. Peptides containing the RGD (Arg-Gly-Asp) peptide motif bind integrin $\alpha_v\beta_3$, and a number of synthetic derivatives have been radiolabeled for both SPECT/PET imaging (^{111}In , ^{64}Cu) [44, 45] and TRT (^{177}Lu , ^{211}At) [44, 46]. A significant drawback of peptides for TRT is their relatively rapid clearance from the blood, limiting tumor accumulation and the duration of their effect [47]. To extend circulation lifetime, carrier PEGylation [48] and incorporation of small moiety serum albumin binders have been explored [47, 49, 50].

1.1.2.1 ^{177}Lu -DOTATATE (Lutathera®)

Peptide-based TRT (peptide receptor radionuclide therapy, PRRT) emerged in the early 1990s to target the somatostatin receptor (SSTr), which is overexpressed in neuroendocrine tumors (NETs) [14]. Upon binding the endogenous ligand, the ligand-receptor complex is internalized, leading to inhibition of multiple metabolic and secretory pathways [51]. The biological half-life of

the native peptide hormone somatostatin is very short (1-3 min) as it is degraded by peptidases found in both the plasma and in tissues [52]. As such, somatostatin analogs with improved pharmacokinetic properties were investigated (half-life from 1.5-12 hr), usually hexapeptides or octapeptides (containing 6 or 8 amino acids, respectively) that retained the biologically-active motif of endogenous somatostatin (Figure 5) [51]. Of these, octreotide labeled with In-111 was the first SSTR agonist to receive FDA approval [51] for SPECT imaging ($^{111}\text{In-DTPA}^0\text{-D-Phe}^1$ or $^{111}\text{In-pentetreotide}$). This agent was investigated in a few clinical trials as a therapeutic due to emission of Auger/conversion electrons [14]. Patient benefit was limited, leading to the adoption of high-energy β -emitters yttrium-90 and lutetium-177 [53]. Octreotide was first labeled with yttrium-90 ($^{90}\text{Y-DOTATOC}$) and clinical results were promising, yet toxicity in the dose-limiting bone and kidneys was observed [51]. Reduced nephrotoxicity was later noted with lutetium ($^{177}\text{Lu-DOTATOC}$) yet tumor retention time was improved with the related octreotate (same amino acid sequence, but difference in redox state of terminal residue, $^{177}\text{Lu-DOTATATE}$) [54]. Disease control rates for patients receiving $^{90}\text{Y-octreotide}$ or $^{177}\text{Lu-DOTATATE}$ were 68-94%, with progression-free survival rates improved relative to chemotherapy, “cold” somatostatin analogues, and targeted small molecule therapies (sunitinib, everolimus) [53]. The phase III NETTER-1 (NCT01578239) trial with $^{177}\text{Lu-DOTATATE}$ and long-acting octreotide versus double the dose of long-acting octreotide demonstrated progression-free survival and quality of life benefits in patients with unresectable or metastatic midgut NETs, which was pivotal to EMA and FDA approval of $^{177}\text{Lu-DOTATATE}$ (Lutathera®) in 2017 and 2018, respectively [55, 56].

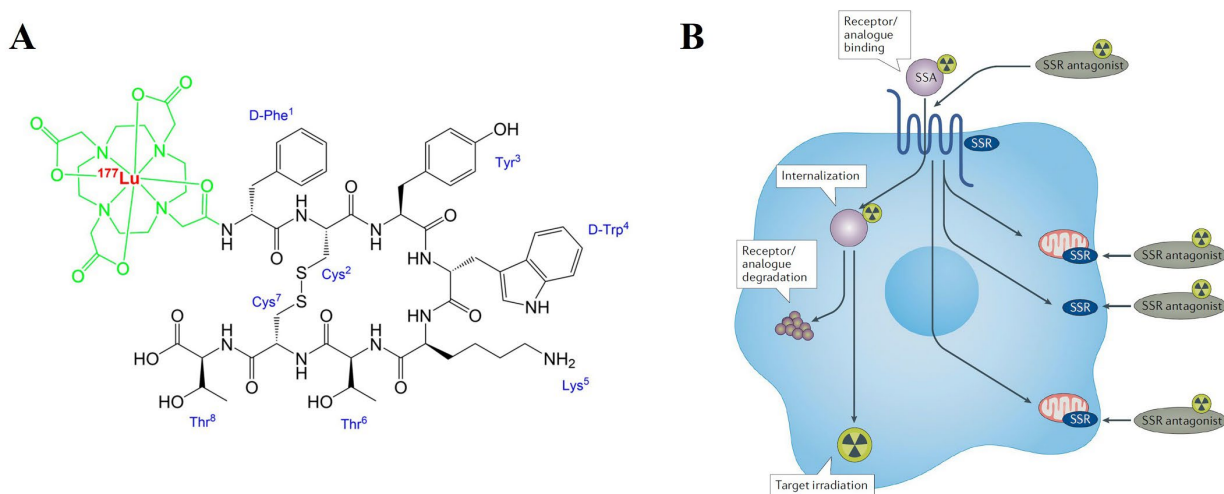


Figure 5 (A) Molecular structure and amino acid composition of ^{177}Lu -DOTATATE. The chelator DOTA is shown in green. (B) Scheme of PRRT mechanism of action. A somatostatin analogue (SSA, typically a radiolabeled octreotide, ex. ^{177}Lu -DOTATATE) first binds the somatostatin receptor (SSR). The SSA is internalized and the receptor is recycled. Newer SSR antagonists bind more extensively and can irradiate internal targets but are internalized to a lesser extent. (A) is reproduced from Hennrich and Kopka, 2019, and (B) is reproduced from Sgouros et al, 2020.

Meta-analyses have demonstrated that SSTR2 PRRT is generally well-tolerated in patients, with moderate bone marrow and renal toxicity frequently observed [51, 57]. Hematological toxicity is mild and transient in 90% of cases, and modest renal impairment can occur. Myelodysplastic syndromes and leukemias are rare, arising in about 2% of reported cases.

Trials since NETTER-1 have sought to expand the indication for Lutathera® to poorly-differentiated and adrenergic NETs [51] as well as to further optimize the PRRT paradigm using radiolabeled somatostatin analogs. In contrast to previous work, studies utilizing somatostatin receptor antagonists have been conducted – these can additionally engage inactive membrane SSTRs, leading to increased radiation dose despite reduced internalization (Figure 5B) [14]. A phase I trial with ^{177}Lu -DOTA-JR11 resulted in a 45% overall response rate and 85% disease control rate after two PRRT cycles, compared to the usual four cycles of agonist octreotide PRRT [58]. To increase the therapeutic index of octreotate, it has been labeled with the α -emitters

actinium-225 (^{225}Ac -DOTATATE) and lead-212 (^{212}Pb -DOTAMTATE). Preliminary studies have shown encouraging efficacy in both PRRT naïve [59, 60] and β PRRT-refractory patients [60-62].

1.1.2.2 ^{177}Lu -PSMA-617 (Pluvicto[®])

Much of the current work with small molecule peptide TRT over the past decade involves optimizing prostate specific membrane antigen (PSMA)-targeted ligands to maximize tumor uptake while diminishing toxicity. PSMA is a hallmark antigen expressed by most prostate cancers, and its upregulation is associated with castration resistance and metastasis (mCRPC) [63]. PSMA inhibitors are generally dipeptide-based agents containing the Glu-ureido-Lys motif (^{177}Lu -PSMA-R2 and ^{177}Lu -PSMA-617) or are phosphoramidate-based (^{177}Lu -CTT-1403) mimics of the natural substrates N-acetylaspartylglutamate and γ -glutamyl folic acid derivatives (Figure 6A) [14, 63]. Zinc (II) in the PSMA active site interacts with the urea and phosphoramidate functionalities of the inhibitors, as does the S1 glutamate residue and entrance funnel of PSMA (Figure 6B) [14]. The presence of the entrance funnel provides flexibility in the selection of pendant group and chelator molecular structure. Compounds that interact favorably with this entrance funnel are likely to be internalized [64]. Recently it was discovered that low-molecular weight inhibitors that display similar efficacy to PSMA-617 are released into the cytoplasm prior to recycling of the receptor [65], which is advantageous for both imaging and therapy applications.

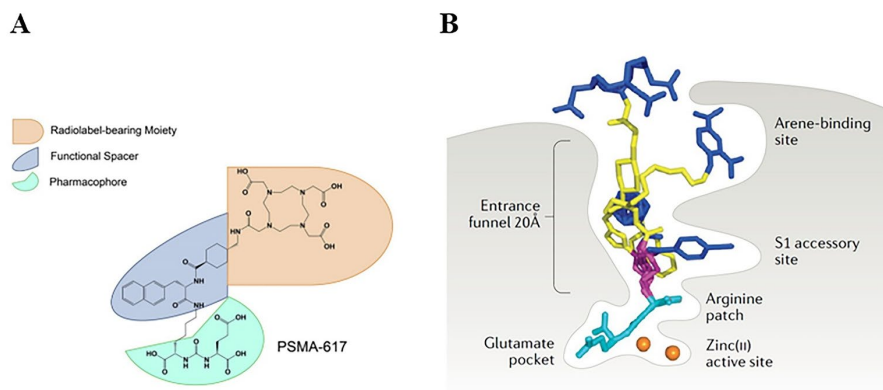


Figure 6 PSMA-617 and generalized PSMA inhibitor interaction with PSMA receptor. (A) Molecular structure and arrangement of PSMA-617. (B) Components of PSMA receptor and composite of 5 Glu-ureido PSMA ligands, including PSMA-617. The shared pharmacore overlap is shown in light blue, but the orientation of the linker (magenta), functional spacer (yellow), and radionuclide chelator (dark blue) are variable within and outside the receptor. Adapted from Kopka et al, J. Nucl. Med. 2017.

PSMA-617 is the lead TRT candidate under study preclinically and was FDA-approved by both the FDA and EMA in 2022. Although Phase III clinical results of ^{177}Lu -PSMA-617 in mCRPC were impressive [66], from a meta-analysis, 30% of patients are refractory to β therapy (no decline in serum prostate specific antigen, PSA) [67]. Causes of treatment failure may fall within two main categories – radioresistance (DNA damage repair mechanisms, tumor biology, somatic or germline mutations) and inadequate radiation dose delivery (insufficient administered activity, low or heterogenous PSMA expression, insufficient tumor retention time) [68-70]. Prolonging circulation time to increase tumor accumulation via the incorporation of the albumin-binding moiety of Evans blue dye (^{177}Lu -EB-PSMA-617) provided a twofold to sixfold increase in tumor lesion accumulated activity versus ^{177}Lu -PSMA-617 [71]. The effectiveness of targeted α therapy (^{225}Ac -PSMA-617) can vary among patients progressing with β therapy, given the disease state (early vs. late mCRPC), the extent of pretreatment, and metastatic profile [72, 73]. PSA reduction with ^{225}Ac -PSMA-617 in TRT-naïve tumors can be more substantial than those reported for ^{177}Lu -PSMA-617, as expected given the greater LET of ^{225}Ac [73].

1.1.2.3 LLP2A

The $\alpha_4\beta_1$ integrin or very late antigen-4 (VLA-4) is a heterodimeric transmembrane receptor that binds to fibronectin and vascular cell adhesion molecule 1 (VCAM-1) [41]. Although restricted to hematopoietic cells involved in lymphocyte trafficking in healthy adults, VLA-4 has roles in tumor promotion, angiogenesis, and metastasis. VLA-4 expression is observed in both solid (melanomas, sarcomas) and hematologic malignancies (leukemias, lymphomas). Tumor VLA-4 upregulation is correlated to the development of metastasis in melanoma patients [74]. This is of particular interest as melanoma is well-managed by surgical excision when localized [75], but prognosis worsens substantially once metastatic [76].

Screening of a one-bead-one-compound combinatorial library of more than 1500 variants identified LLP2A, a high affinity ($IC_{50} = 2$ pM) peptidomimetic selective to VLA-4 [41]. LLP2A showed no apparent binding to similar integrins or those containing only one of the subunits. Further, LLP2A preferentially bound the active conformation of VLA-4 such that leukemia and lymphoma cells were targeted but not healthy lymphocytes. Previous work in the Anderson Lab has demonstrated the utility of LLP2A for PET imaging of preclinical melanoma with gallium-68 and copper-64 [42, 77], as well as its therapeutic efficacy when labeled with lutetium-177 [42, 78]. Towards optimization of LLP2A as a theranostic, improvements in the pharmacokinetics and efficacy of LLP2A imaging/therapy is a major thrust of our lab. Copper-64 ($t_{1/2} = 12.7$ h, β^+ , 0.653 MeV [17.8%]) is well-suited for PET imaging as its relatively long half-life allows for the monitoring of fast-clearing small molecules as well as larger proteins and nanoparticles [79]. Copper coordination chemistry has been thoroughly investigated such that it is amenable to a wide array of chelators that can be conjugated to diverse vectors for imaging and/or therapy. The

Anderson Lab has pioneered the cross-bridged cyclam chelator CB-TE1A1P for copper radionuclides (Figure 7A), which possesses excellent *in vivo* stability and can be labeled at high specific activity under mild conditions [79]. Biodistribution of the vector is greatly influenced by the chelator selection – unconjugated ^{64}Cu -CB-TE1A1P displayed similar or improved *in vivo* characteristics compared to the more established CB-TE2A (^{64}Cu -CB-TE2A) [80], and ^{64}Cu -CB-TE1A1P-LLP2A demonstrated significantly greater tumor-to-nontarget organ ratios in a mouse melanoma model than the standard radionuclide chelator NODAGA (^{64}Cu -NODAGA-LLP2A, Figure 7B) [42].

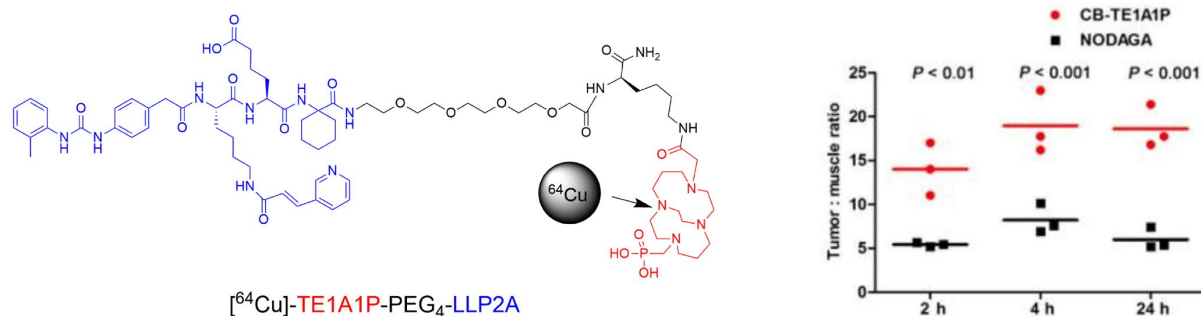


Figure 7 Molecular structure of ^{64}Cu -CB-TE1A1P-LLP2A (A) and comparison of tumor: muscle ratios of ^{64}Cu -CB-TE1A1P-LLP2A and ^{64}Cu -NODAGA-LLP2A in a murine B16F10 melanoma model (B). Plot reproduced from Beaino and Anderson, 2014.

Others have utilized ^{64}Cu -CB-TE1A1P-LLP2A for PET imaging of multiple myeloma, a generally incurable hematological cancer characterized by unregulated proliferation of plasma cells in the bone marrow [81, 82]. VLA-4 facilitates the adherence of myeloma cells to the bone marrow extracellular matrix via fibronectin and VCAM-1 [82]. ^{64}Cu -CB-TE1A1P-LLP2A demonstrated high *in vivo* specificity for myeloma lesions with signal contribution from inflammatory cells in the lesion microenvironment [82]. These results spurred a clinical trial (NCT03804424) that is currently ongoing. From a preliminary report, ^{64}Cu -CB-TE1A1P-LLP2A

was well-tolerated in both multiple myeloma and healthy subjects, with promising dosimetry (rapid blood clearance, longest residence time in the red marrow) [81]. Given the role of VLA-4 in immune cell trafficking to areas of inflammation, ^{64}Cu -CB-TE1A1P-LLP2A has also been utilized preclinically to image acute lung injury [83] and vaso-occlusive episodes in sickle cell anemia [84]. Encouraging preclinical results in ^{64}Cu -CB-TE1A1P-LLP2A PET imaging of sickle cell disease have led to a phase I clinical trial that is currently recruiting (NCT04925492).

1.2 ICI Therapy and Combination with ICI

T cells are the main weapons of the antitumor immune system armamentarium, which are targeted to a specific antigen. T cells express the T-cell receptor (TCR), which upon interaction with major histocompatibility complex (MHC) bound to the cognate antigen on antigen-presenting cells (APC) signals through the T cell characteristic CD3 complex (Figure 8) [85]. The CD28 costimulatory receptor is constitutively expressed by T cells, and this binds the B7 family of costimulatory molecules expressed mainly by professional APCs. T cell activation requires two essential signals: 1) TCR engagement for CD3 signaling, and then 2) CD28-B7 costimulatory interaction. Antigen presentation to T cells with the TCR specific to the antigen activates T cells and prompts T cell-mediated functions. These T cells differentiate, proliferate, and secrete immunomodulatory cytokines, with the eventual creation of memory T cells able to respond to rechallenge. CD8^+ T cells are the broadly cytotoxic effector population. However, to restrict collateral damage to healthy cells, T cell activation is accompanied by the upregulation of inhibitory molecules that reduce their activity such that their functional lifetime is limited. There

are multiple intricate cell-intrinsic and extrinsic means by which T-cell function is regulated such that a duality of antitumor immunity and immune suppression exist.

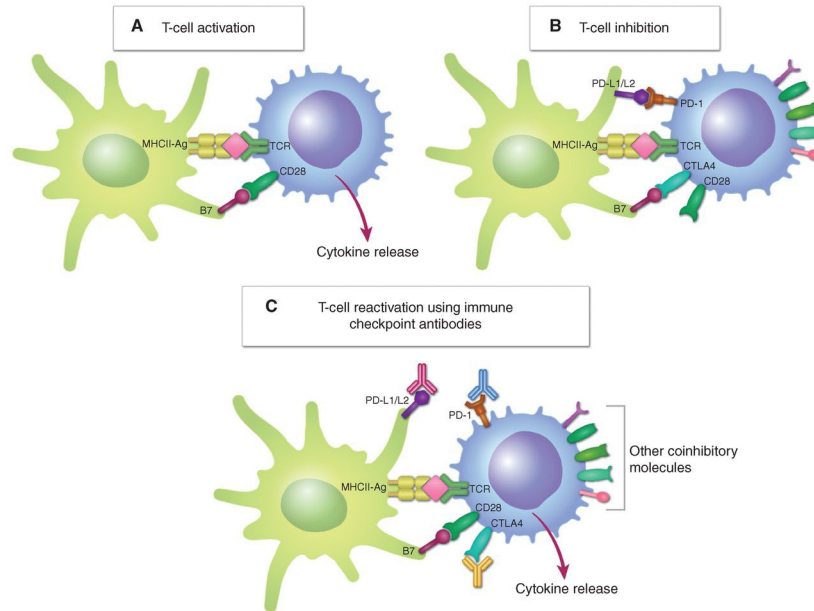


Figure 8 T cell activation, regulation, and reactivation following ICI therapy. (A) Interaction of the TCR and the MHC-antigen peptide complex (MHC-Ag) presented by the APC (yellow and pink, signal 1) and engagement of CD28, the costimulatory receptor on T cells by B7 costimulatory ligands on the APC (CD80/CD86, signal 2), prompts proinflammatory CD8⁺ T cell activation. (B) T cell activation also causes the upregulation of immune checkpoint molecules such as PD-1 and CTLA-4 that dampen T cell activity upon binding to PD-L1/L2 and B7, respectively. (C) Antibodies to PD-1/PD-L1 and CTLA-4 prevent inhibitory interactions, allowing for T cell reinvigoration. Image reproduced from Sharma et al, 2021.

Blocking suppressive interactions that inhibit antitumor immune activation with antibody-based immune checkpoint inhibitors (ICI) has led to unprecedented and durable responses in patients with numerous cancer types [86]. Most notable of these are antibodies to CTLA-4 (cytotoxic T lymphocyte antigen 4) and to the PD-1/PD-L1 axis (programmed death receptor 1 and its ligand), which may be used together to maximize therapeutic efficacy given the non-redundant roles of these mediators in tumor immune evasion [87]. CTLA-4 expressed by regulatory T cells and activated CD8⁺ effector T cells is a homolog of CD28 and binds B7

costimulatory molecules with greater affinity, dampening T cell activity [85]. Anti-CTLA-4 functions to maintain effector T-cell priming by CD4⁺ ‘helper’ T cells and to increase clonal diversity. Ipilimumab, the first anti-CTLA-4 ICI in widespread clinical use, was FDA approved for advanced melanoma in 2011. PD-1 is expressed by activated CD8⁺ effector T cells and binds PD-L1 or PD-L2, which are extensively expressed in non-lymphoid tissues [85]. This leads to a deactivation signal propagated through the TCR. Tumor PD-L1 expression in tumors may be inherent or induced due to an antitumor response [86]. As such, anti-PD-1/L1 reactivates exhausted CD8⁺ T cells. In clinical trials, anti-PD-1/L1 prompted longstanding tumor regression in multiple tumor histologies, even in those previously considered to be resistant to immunotherapy [86]. As a result, two anti-PD-1 antibodies (nivolumab, pembrolizumab) and an anti-PD-L1 antibody (atezolizumab) have been FDA approved for advanced melanoma, head and neck squamous carcinoma, bladder cancer, non-small-cell lung cancer, and renal cell carcinoma, among others [85]. However, poorly immunogenic tumors may not respond to ICI, and for those that do eventual immune escape often occurs [86, 88].

In rare cases, combining EBRT and ICI has prompted regression of non-irradiated metastases (the abscopal effect) in patients [7]. Further, preclinical studies demonstrate that EBRT can induce responses in tumors initially refractory to ICI and improve ICI effectiveness in responsive 'hot' tumors [87, 89]. EBRT causes accumulation of damaged DNA in the tumor cell cytosol, which prompts a type I interferon response via activation of the stimulator of interferon genes (STING) adaptor protein [90]. These signals, with concurrent upregulation or secretion of damage-associated molecular patterns (e.g. high mobility group box protein 1) due to tumor cell death [91], may stimulate dendritic cells (DCs) to cross-prime naïve CD8⁺ T cells with released tumor antigens [92]. The irradiated tumor and tumor draining lymph nodes become hubs for

antigen presentation [93], leading to diversification and clonal expansion of the TCR repertoire [87]. Surviving tumor cells are sensitized to immune elimination via upregulation of immune susceptibility markers (e.g. MHC-I) and the display of tumor neoantigens [94] as well as altered expression of checkpoint molecules such as PD-L1 [95, 96]. Together, these TME modifications increase ICI efficacy when combined with radiotherapy. Importantly, it has been demonstrated *ex vivo* that dose-equivalent β TRT can achieve comparable STING activation to EBRT [97], which is crucial to its translational potential in combination with ICI. However, TRT-induced alterations to antitumor immunity have only begun to be elucidated [98, 99]. From our understanding of EBRT-mediated effects and preliminary studies with TRT, a putative mechanism for TRT and ICI cooperation is shown in Figure 9.

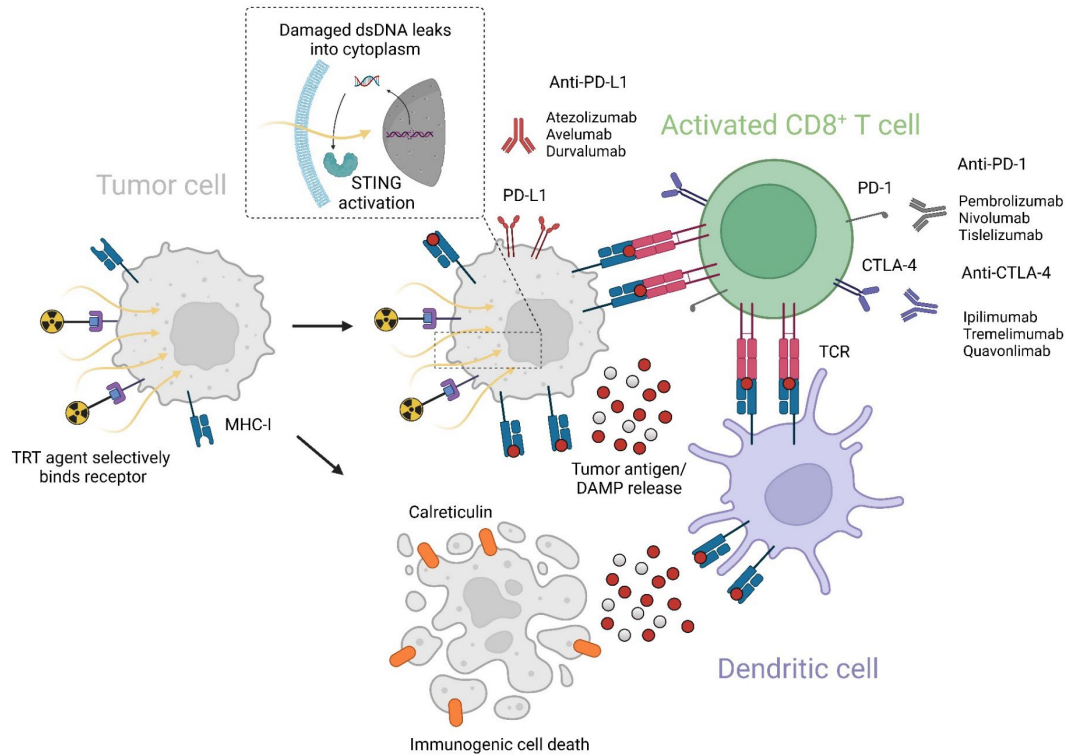


Figure 9 TRT and ICI synergize via immune mechanisms. The TRT agent binds a tumor cell target receptor, and emitted radiation induces release of tumor-associated antigens and damage-associated molecular patterns (DAMPs), causes DNA damage, and potentially prompts immunogenic cell death. Damaged cytoplasmic DNA stimulates STING, leading to a type I interferon response. Tumor MHC-I expression is increased as is neoantigen processing and presentation on MHC, and stimulated activation of dendritic cells (DCs) correspondingly increases antigen cross-presentation to T cells. The expression of immune checkpoint molecules is modulated, allowing for maintained immune activation with ICI. As a DAMP, calreticulin is newly expressed on the outer membrane of tumor cells undergoing immunogenic cell death, leading to phagocytosis by DCs that is central to their activation. dsDNA = double-stranded DNA; TCR = T-cell receptor. Adapted from Bellavia et al, J. Nucl Med, 2022.

At present, most studies involving combined TRT and ICI have been conducted preclinically, with minimal Phase I and case report data available, although numerous clinical trials are ongoing.

1.2.1 Preclinical Studies of TRT + ICI

1.2.1.1 Antibody and Antibody Fragment TRT + ICI

Jiao *et al* observed notable tumor growth delay and improved survival for melanoma-bearing mice receiving an anti-melanin antibody (h8C3) labeled with the α -emitter ^{213}Bi + anti-PD-1 relative to anti-PD-1 alone [100]. In a follow-up study with longer-lived isotopes (^{177}Lu , ^{225}Ac) and to deduce the mechanisms involved, ^{225}Ac -h8C3 provided no improvement \pm anti-PD-1 [101]. Although low-dose ^{177}Lu -h8C3 + anti-PD-1 significantly slowed tumor growth and improved survival, no difference was observed in tumor-infiltrating T cells (TILs) versus untreated controls. A fully-human anti-mesothelin antibody labeled with the α -emitter ^{227}Th (^{227}Th -TTC) spurred multiple immunostimulatory pathways in murine colorectal cancer expressing human mesothelin that increased CD8^+ T cell infiltration while reducing CD4^+ T cells, the effects of which were augmented by anti-PD-L1 [102]. Depletion of suppressive cells in the TME by β RIT (^{177}Lu -anti-CD11b) increased dual ICI (anti-CTLA-4 and anti-PD-1) efficacy in a glioma model, without other significant alterations to the TME immune cell composition [103]. Others have utilized ICIs themselves as radioimmunotherapy agents, particularly anti-PD-L1 given its demonstrated clinical prognostic value in determining responsiveness to PD-1/L1 therapy [104]. PD-L1 monoclonal antibodies have been labeled with both α (^{213}Bi [105])- and β (^{177}Lu [106])-emitters to simultaneously invigorate an antitumor TME milieu and deplete tumor cells. Enhanced therapeutic efficacy versus the isotype or unlabeled control was evidenced against human melanoma xenografts [105] and mouse colorectal cancer [106].

1.2.1.2 Small Molecule Peptide TRT + ICI

Recently, pioneering peptide TRT studies directed to overexpressed integrins improved therapeutic outcomes in combination with ICI in B16F10 melanoma [78, 107] and MC38 colorectal cancer [49]. Choi *et al* demonstrated in B16F10 melanoma that lutetium-177 labeled LLP2A with dual ICI (anti-CTLA-4 and anti-PD-1 or anti-PD-L1), significantly improved survival relative to either TRT or dual ICI [78]. Combining a modified RGD peptide to bind integrin $\alpha_v\beta_3$ labeled with lutetium-177 paired with anti-PD-L1, Chen *et al* showed that concurrent administration significantly reduced tumor volume and extended survival versus a sequential approach in MC38 colorectal cancer [49]. In a murine prostate cancer model, Czernin *et al* aimed to exploit potentially increased tumor immunogenicity spurred by ^{225}Ac -PSMA-617 by adding anti-PD-1 [108]. The combination synergized to improve survival and delay time to progression, but the immune correlates were not reported.

1.2.1.3 Non-Peptide Small Molecule TRT + ICI

Directing α -therapy to the tumor cell nucleus prompts extensive DNA double strand breaks, inducing antitumor T cell activation that can be invigorated by ICI. Dabagian *et al* utilized an astatine-211 (^{211}At)-labeled small molecule inhibitor of PARP, a class of nuclear enzymes that facilitate double strand break repair [109]. With anti-PD-1 in a mouse glioblastoma model, the combination nearly doubled the mean progression free duration of ICI (65d vs. 36d) and led to complete response in all mice, compared to 60% of mice receiving ICI alone. Interestingly, TRT increased macrophage recruitment while depleting circulating T cells. The authors postulate that

the improved therapeutic effect of the combination is due to activated macrophage proinflammatory signaling maintained by blocking PD-1.

1.2.2 TRT Sensitizes ‘Cold’ Tumors to ICI

The key promise of TRT + ICI is the capability to render immunologically 'cold' tumors (unresponsive to ICI alone) vulnerable to ICI via radiation-induced immune activation. Major cancer types resistant to ICI include colon, prostate, and breast cancer, although varied responses can occur even amongst tumors within the same patient [86]. These tumors display minimal T cell infiltration and substantially impaired preexisting antitumor immunity. Radiation has been shown to elicit antitumor immune responses through induction of a cGAS-STING mediated type I interferon response, which is dose-dependent [98]. From preclinical experiments, antitumor immunomodulation via EBRT occurs even at low doses (2-5 Gy) [110]. This observation could be leveraged by rationally designed TRT to deliver low dose sufficient for immunostimulation while sparing radiosensitive lymphocytes systemically.

Patel *et al* recently employed this approach to evaluate the alkylphosphocholine analog NM600 labeled with the β -emitter ^{90}Y in combination with anti-CTLA-4 in multiple ICI-resistant tumor models (Figure 10) [98]. When low dose (2.5-5 Gy) ^{90}Y -NM600 was received by the tumor as determined from ^{86}Y -NM600 PET via a Monte Carlo dosimetry software, survival was significantly improved compared to ICI alone. Dramatic responses were observed, with up to two-thirds of mice receiving the combination experiencing complete response and tumor-specific T cell memory, compared to none in either single treatment group. No signs of toxicity were seen. The combined treatment increased T cell infiltration and mitigated exhaustion. Intriguingly, the authors showed that unlike a previous report utilizing moderate dose, single-tumor directed EBRT

[87], low dose TRT did not expand TCR diversity despite the clonal expansion of TILs. By combining these modes of EBRT and TRT, their non-redundant effects better potentiated response to anti-CTLA-4, allowing for control of a secondary (received no EBRT) tumor and optimal survival relative to either TRT or EBRT + anti-CTLA-4.

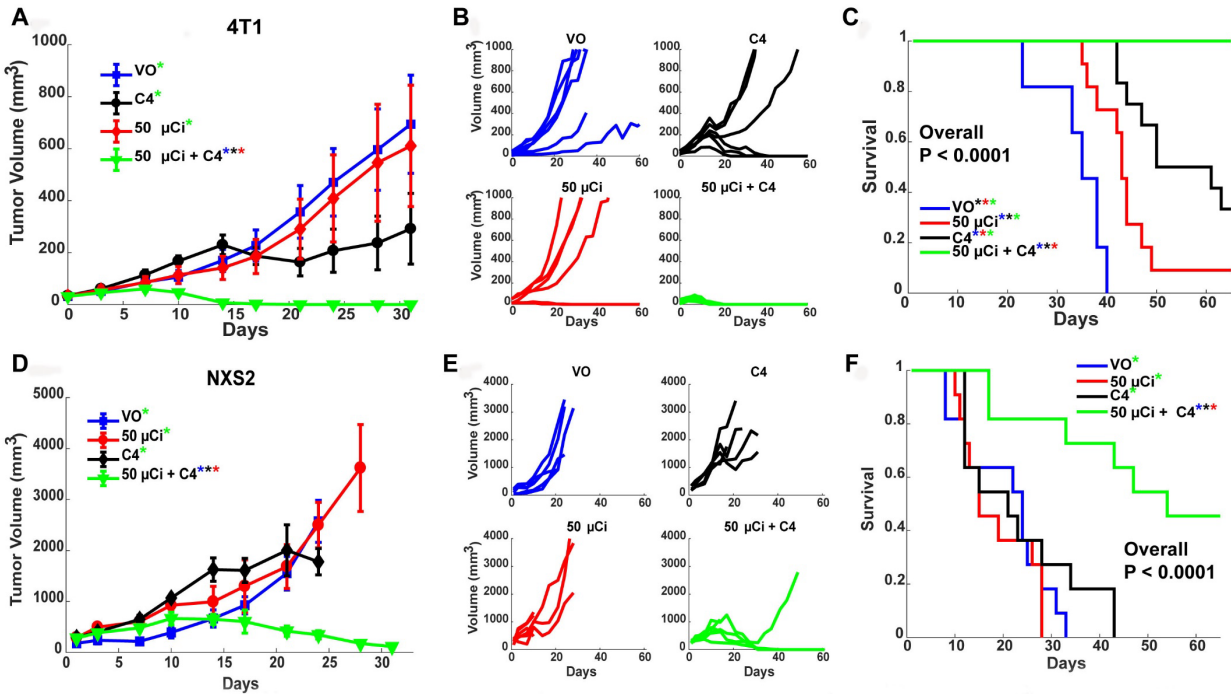


Figure 10 TRT sensitizes 'cold' murine tumor models to ICI. Tumor volume and survival in 4T1 breast cancer (A-C) and NXS2 neuroblastoma (D-F) in mice receiving 200 μg CTLA-4 (C4, 3x) with or without 50 μCi ⁹⁰Y-NM600 or saline control (vehicle only, VO) (n=5-6 each). Image adapted from Patel et al, 2021.

1.2.3 Clinical Trials of TRT + ICI

Although combination TRT + ICI clinical trials are ongoing, there are few recent reports of intentional TRT sensitization to ICI in the available clinical literature, enabled by compassionate use authorization. Two case reports demonstrate impressive therapeutic efficacy with TRT+ ICI

in patients with metastatic Merkel cell carcinoma (MCC), an aggressive skin cancer, who progressed on first-(avelumab/anti-PD-L1) and/or second-line (ipilimumab/anti-CTLA-4 + nivolumab/anti-PD-1 + EBRT) therapies [111, 112]. Half of MCC patients may not respond or acquire resistance to ICI [112], yet MCC often expresses somatostatin receptors, allowing for targeting via ^{177}Lu -DOTATATE. A patient with heavy MCC metastatic burden who received ^{177}Lu -DOTATATE and resumed anti-PD-L1 demonstrated a response within days, with near complete response observed one month after initiation (Figure 11) [111]. In a separate report, a patient receiving the related ^{177}Lu -DOTATOC and resuming ipilimumab + nivolumab experienced partial response that was maintained through the time of the manuscript submission (5 months) [112]. Although the GoTHAM trial (NCT04261855) to evaluate ^{177}Lu -DOTATATE + avelumab for metastatic MCC has begun, survival data is unlikely to be available until 2024.

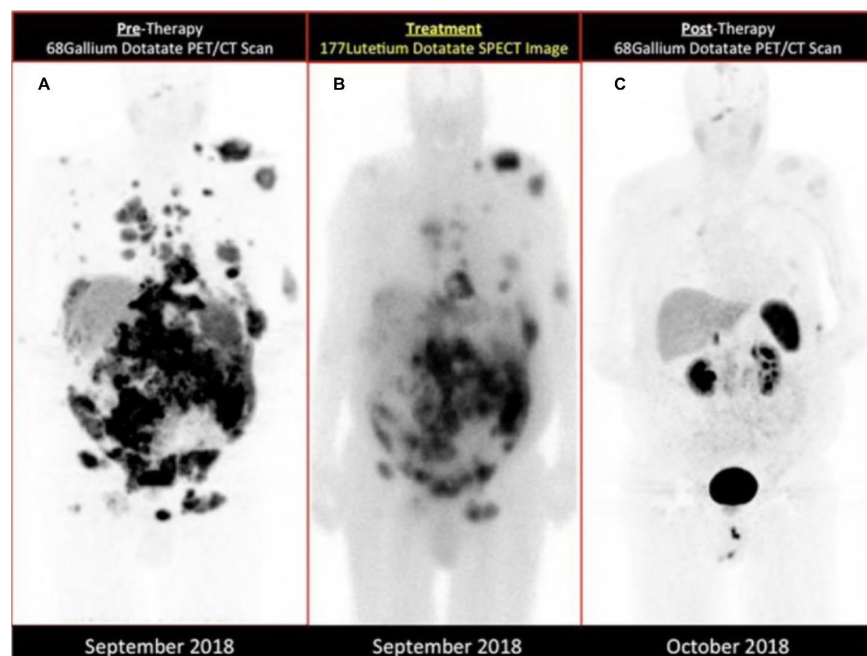


Figure 11 Dramatic improvement in a patient refractory to anti-PD-L1 (avelumab) receiving a single off-label dose of ^{177}Lu -DOTATATE for heavily metastatic Merkel cell carcinoma and resuming avelumab. (A) Pre-treatment ^{68}Ga -DOTATATE PET/CT scan, (B) ^{177}Lu -DOTATATE SPECT/CT scan during TRT, and (C) ^{68}Ga -DOTATATE PET/CT scan 1 month post-treatment. Image reproduced from Kasi et al, 2019.

Despite the rapid pace of TRT development, most exploratory clinical trials combining TRT and ICI utilize established TRT agents (^{177}Lu -DOTATATE, ^{177}Lu -PSMA-617, $^{223}\text{RaCl}_2$). Those that are ongoing/have published results within the past several years are highlighted.

1.2.3.1 ^{177}Lu -DOTATATE (Lutathera[®]) + ICI

^{177}Lu -DOTATATE is the culmination of more than 20 years of somatostatin analog development for NET treatment, with wide clinical adoption following the phase III NETTER-1 trial (NCT01578239) [113]. Somatostatin receptor expression has also been identified in a minority of small-cell lung cancer (SCLC) [114]. Due to its aggressiveness (5-year overall survival rate <10%), SCLC often presents once disseminated and is ultimately refractory to chemotherapy [115]. As a subset of extensive-stage SCLC patients display durable responses to nivolumab, Kim *et al* conducted a phase I trial (NCT03325816) combining ^{177}Lu -DOTATATE and nivolumab at two TRT dose levels in patients with relapsed/refractory SCLC, SCLC remaining stable following first-line chemotherapy, or pulmonary NETs [115]. Of the 7 patients with disease measurable by CT, one with extensive-stage SCLC showed partial response, and two others with atypical carcinoid displayed stable disease. The SCLC patient who experienced partial response showed avid tumor uptake of ^{68}Ga -DOTATATE. However, unlike observations mainly from extrapulmonary NETs [113], the extent of ^{68}Ga -DOTATATE uptake may not predict TRT efficacy in lung NETs/SCLC [114].

1.2.3.2 ^{177}Lu -PSMA-617 (Pluvicto[®]) + ICI

Approximately one-third of patients do not respond to ^{177}Lu -PSMA-617 despite extensive PSMA expression evident from PET [116]. In a recent phase II trial (NCT02787005), pembrolizumab (anti-PD-1) demonstrated encouraging efficacy in pre-treated, bone-predominant mCRPC [117]. Prasad *et al* observed 40% PSA decline in a 90-year-old patient with advanced mCRPC who initiated ^{177}Lu -PSMA-617 while receiving pembrolizumab for locally advanced squamous cell carcinoma [116]. To interrogate potential synergy between ^{177}Lu -PSMA-617 and pembrolizumab, the phase Ib/II PRINCE trial (NCT03658447) was initiated. Although the study is ongoing, an interim report details a $\geq 50\%$ PSA decline rate of near 75% among 37 patients [118]. Seven of nine patients with measurable disease exhibited partial responses. Therapy with ^{225}Ac -PSMA-617 has shown remarkable efficacy (70% rate of PSA decline $\geq 50\%$, 29% complete response rate from ^{68}Ga -PSMA PET) in heavily-pretreated, TRT-naïve patients [73], but can be hampered by dose-limiting xerostomia (PSMA is expressed in the salivary glands) [119]. This may be only partially resolvable [72, 73]. TRT via a PSMA-targeted antibody (J591) has circumvented this issue in patients [120], and a clinical trial to assess ^{225}Ac -J591 + pembrolizumab (NCT04946370) is now recruiting. Similarly, Hammer and colleagues demonstrated impressive antitumor efficacy with another PSMA-targeted antibody labeled with ^{227}Th (^{227}Th -BAY2315497) in patient-derived xenograft models, including one simulating bone metastasis [121]. These results led to a clinical trial (NCT03724747) that is currently ongoing. Compared to ^{225}Ac , ^{227}Th possesses the advantage of being the parent radionuclide of ^{223}Ra , which has a well-established efficacy and safety profile in patients with prostate cancer that has metastasized to bone [23, 122].

1.2.3.3 $^{223}\text{RaCl}_2$ (Xofigo[®]) + ICI

Xofigo[®] is non-chelated ^{223}Ra , an α -emitter with chemical similarity to calcium selectively trafficked to areas of increased bone stroma formation, as occurs within sclerotic or osteoblastic bone metastases [23]. The vast majority (> 90%) of mCRPC patients display bone metastases radiographically, and a substantial fraction of mCRPC deaths result from these metastases and their complications. Due to the short range of α radiation, cytotoxicity is constrained to the target region, limiting myelotoxicity. From a landmark phase III clinical trial (NCT00699751), Xofigo[®] was demonstrated to significantly extend time to the first symptomatic skeletal event and overall survival [23]. To investigate whether ^{223}Ra -mediated cell death potentiates pembrolizumab in intractable cancers, a phase II trial in mCRPC (NCT03093428) and a phase I/II trial in metastatic NSCLC (NCT03996473) patients with bone metastases are ongoing. Preliminary results from the mCRPC trial have not shown therapeutic benefit for the combination [123]. A phase Ib trial of Xofigo[®] + atezolizumab (anti-PD-L1) in mCRPC (NCT02814669) demonstrated increased toxicity without appreciable clinical benefit versus either alone [124].

1.3 Radionuclide Dosimetry Towards Patient-Tailored TRT

1.3.1 Overview of Radionuclide Dosimetry

From decades of EBRT studies, the absorbed dose, or the energy absorbed per mass of tissue, has been established to predict biologic effects [125]. Yet unlike EBRT, TRT dose is dispersed heterogeneously at both the cellular and tumor/organ levels, resulting in 'hotspot' regions

of absorbed dose [24]. TRT dose distribution in tumors is influenced by numerous factors related to the tumor itself (ex. permeability, perfusion), targeting molecule (ex. affinity for cell-surface receptors/molecules, stability in serum), and radionuclide decay profile. The resulting biological effects are impacted by an array of additional variables such as the radionuclide location within the tumor, hypoxia, and the presence of neighboring normal tissues vulnerable to radiation. TRT toxicity to normal organs generally manifests as absorbed dose hotspots in a particular compartment(s), especially those required for proper organ function [14]. For example, peptide-based TRT agents tend to accumulate in the renal cortex, so the renal cortex absorbed dose is a more reliable predictor of toxicity than that of the entire kidney volume [126].

Compared to other treatment modalities, TRT offers an important advantage. Either with an isotope that has imageable emissions (^{177}Lu) or via a diagnostic imaging/therapy pair ($^{68}\text{Ga}/^{177}\text{Lu}$ in clinical PSMA-617 and DOTATATE therapy), longitudinal 2D (planar γ -camera imaging) or preferably 3D imaging can inform patient-specific therapy via estimation of tumor and normal organ absorbed doses (dosimetry). When paired radionuclides are used, it is critical that their biodistribution matches as closely as possible. Depending upon the decay mode/energy of the imaging radionuclide, SPECT or PET is performed to image tracer pharmacokinetics, with computed tomography [120] co-registered to provide anatomical reference (SPECT/CT or PET/CT). Dosimetry tools (e.g. OLINDA/EXM software) have been developed from formalized mathematical summations of radiobiology to gauge toxicity risk for nuclear medicine agents. The current iteration of the most employed dosimetry software, OLINDA/EXM 2.0, utilizes Monte Carlo simulation of voxel-level (3D analog of pixel) radiation transport within simulated reference or population-average patient geometries ("phantoms") to calculate absorbed doses organs experience. Tumors are modeled as separate unit-density spheres [127]. Monte Carlo simulation

involves the repeated random sampling of a variable with inherent uncertainty from a probability distribution many thousands or millions of times to output a single averaged value. Given a particular isotope and voxel dimensions, the mean absorbed dose per voxel is estimated via a standardized matrix, in which each voxel is a uniform source and neighboring voxels are targets [128]. Because homogenous dose distribution and uptake are assumed within a reference organ rather than bounded from patient CT images, OLINDA/EXM may significantly underestimate absorbed doses relative to patient-specific Monte Carlo simulations [129]. Numerous voxel-level internal dosimetry programs are available, but those that utilize Monte Carlo simulation of direct radiation transport (i.e. 3D dose distribution calculated without summing concentric spherical shells from a point source or without pre-determined values for absorbed dose variables) best account for tissue heterogeneity [130]. Individualized Monte Carlo-based dosimetry has demonstrated improved accuracy relative to standardized phantom-based methods in small patient cohorts [131]. Further, this pretherapy dosimetry could reliably predict tumor and/or at-risk organ doses for TRT [132].

Imaging modalities in clinical use such as PET and SPECT cannot achieve the resolution necessary to map radioactivity distribution at the microscale (< 1 mm), and this likely impedes sufficient dose delivery and the effective assessment of safety [14]. This issue can be circumvented by combining information from PET/CT or SPECT/CT patient images with information obtained by corresponding preclinical tissue analysis [14]. Contours defining organs or macroscale organ compartments can be drawn upon patient PET/CT or SPECT/CT images from which time-activity curves can be generated. Corresponding preclinical tissues can be harvested and microscale substructure dose distribution analyzed with emerging high-resolution imagers. Time-activity curves can be determined for these microscale features, and the integral per curve provides total

radionuclide disintegrations for the entire organ or subcompartments of interest. From these, scaling factors can be derived and extrapolated to determine total disintegrations per subcompartment in the corresponding human organs.

1.3.2 MIRD Dosimetry Formalism

Absorbed dose to a tissue is dependent upon the number of decays within the source region, the energy per decay, and the fraction of the emitted energy absorbed. To determine these metrics, the anatomy of the organs of interest must be established as well as the time-dependent activity distribution within these organs, which is known or extrapolated. The duration of activity retention is quantified as the time-integrated activity (or residence time), which is determined from imaging of the radiopharmaceutical pharmacokinetics. By reframing the definition of the absorbed dose, D , it can be described as the differential of the average energy imparted to matter (ε) divided by the mass (m) that absorbs ε (Eq. 1-1):

$$D = \frac{d\varepsilon}{dm} \quad (1-1)$$

Suggestions from the Medical Internal Dose (MIRD) Committee of the Society of Nuclear Medicine and Molecular Imaging to standardize the assessment of internal radiation dose from imaging radiopharmaceuticals led to the reformulation of Equation 1-1 [133]. The absorbed dose, D , is instead calculated as the product of two values, one that considers the pharmacokinetics of the radiopharmaceutical in the patient, and the one that considers the energy deposition specific to the radionuclide as well as the anatomy of the patient used for the calculation (Eq. 1-2). The absorbed dose, D , is calculated for a target region r_T from the total number of decays $\tilde{A}(r_S)$ within

the source region r_s . The S -value refers to the energy deposited in the target region per decay within the source region and is radionuclide-specific.

$$D(r_T \leftarrow r_S) = \tilde{A}(r_S)S(r_T \leftarrow r_S) \quad (1-2)$$

$\tilde{A}(r_s)$ is determined by integrating the activity in r_s from the time of injection, $t=0$ (Eq. 1-3) to a point where all activity is assumed to have either cleared or decayed – usually infinity.

$$\tilde{A}(r_S) = \int_0^{\infty} \tilde{A}(r_S, t) dt \quad (1-3)$$

To calculate time-integrated activity, the activity in a source region is quantified (for instance, via imaging) at various points in time (Figure 12). $\tilde{A}(r_s, t)$ is approximated as an exponential equation fit to the tissue accumulation and clearance data, with an effective clearance rate λ_e , which is the sum of the biological clearance rate λ_b and the physical decay rate of the radionuclide λ_p . \tilde{A}_0 is the administered activity and f_s is the extrapolated activity fraction in the source region at $t=0$. The time-integrated activity (TIA) or total decays is quantified as the area under this so-called time-activity curve. The S -value encompasses the product of the total energy emitted per decay, Δ , and the energy fraction originating in the source region that is absorbed by the target ($\phi(r_T \leftarrow r_S)$), divided by the mass of the source region $M(r_s)$.

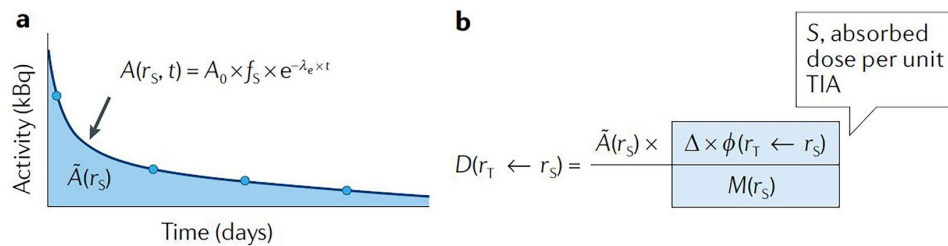


Figure 12 Dosimetry scheme for radiopharmaceutical imaging agents. Representation of factors involved in (A) $\tilde{A}(r_s)$ and TIA determination as well as (B) the S -value and adsorbed dose D within the target region r_T . Image reproduced from Sgouros et al, 2020.

The preceding dosimetry scheme is inadequate for TRT as it is predicated on the use of standardized, reference organ geometries for tumor dosimetry. Instead, a voxelized approach in

which the activity from patient PET/CT or SPECT/CT imaging is integrated over the patient anatomy defined from the CT scan per volume element (voxel) is more suitable. The distribution of the absorbed dose is calculated via Monte Carlo or dose point kernel methods. Dose point kernel tabulation of the absorbed dose involves the averaging of the absorbed dose (energy per mass) of concentric thin spherical shells within the reference geometry given their distance from a point source of radioactivity in water [134]. As shown in Figure 13, the activity distribution from longitudinal imaging is integrated (by voxel or a larger defined region) with respect to time to calculate the TIA per volume element ($\tilde{A}(x,y,z)$). Using a dose point kernel method, the absorbed dose per volume element is calculated as shown for a region within the kidney (Fig. 13b). The TIA of the volume element is multiplied by an established source-to-target distance-dependent absorbed dose per unit TIA factor ($K(r)$), and this value is summed for all volume elements to provide the total dose to the target region of interest (ROI).

Absorbed dose can also be determined by dose rate integration, where dose estimates from imaging are integrated with respect to the dose rate of the therapy radionuclide rather than the

activity. Given the processing of ROI inputs required for dose calculation in the software used for this work, mean dose rate integration was used rather than time-integrated activity.

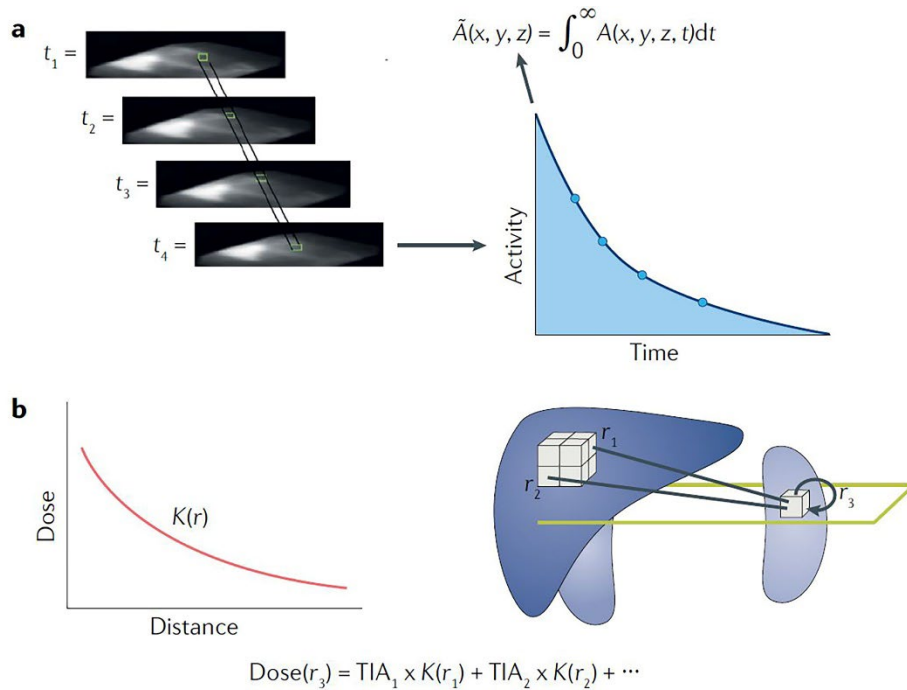


Figure 13 Generalized framework for TRT dosimetry from patient images. (A) Tracer distribution determined from longitudinal imaging is assessed per voxel or volume element and is integrated to determine the TIA in the voxel or volume element. (B) Representation of dose point kernel calculation of absorbed dose for a particular volume element in the kidney (r_3). Image reproduced from Sgourous et al, 2020.

1.3.3 Approaches to TRT Dosimetry

Dosimetry for TRT can roughly be classified according to two considerations – whether it is conducted before or after therapy, and whether the goal is to deliver a particular dose to the tumor or maximize administered activity while aiming to prevent off-target toxicities [8]. Pre-therapy dosimetry utilizes imaging to estimate the biodistribution of the therapeutic dose such that adjustments can be made if a fixed therapy dose was planned. Post-therapy dosimetry utilizes imaging after each TRT cycle to determine the true absorbed dose from the administered therapy. Here, the ensuing cycle can be adjusted if necessary or treatment can be ended if the intended dose

threshold is reached (Figure 14). Dosimetry following each TRT cycle to adjust the number or activity of the cycles is generally not conducted in the clinic, but preliminary prospective trials with ^{177}Lu -DOTATATE have been encouraging [9, 135].

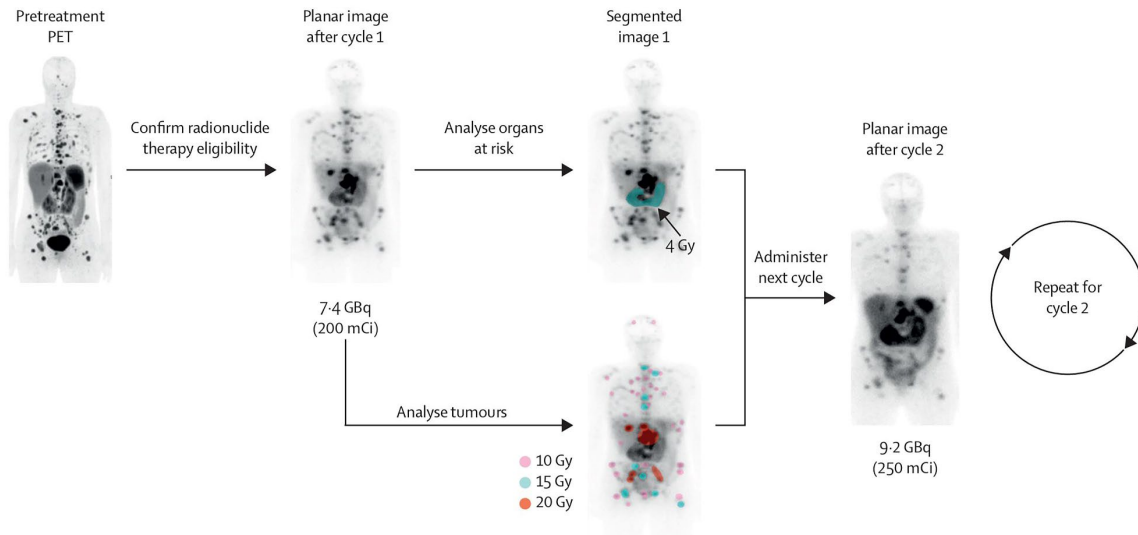


Figure 14 Hypothetical per-cycle dosimetry scheme for ^{177}Lu -DOTATATE NET treatment. Patients are first selected for treatment via ^{68}Ga -DOTATATE. Planar imaging or SPECT/CT can be performed at one timepoint (less accurate, but simpler) or multiple timepoints (more accurate, more time-consuming). On posttreatment imaging, tumors and organs of interest can be contoured to calculate absorbed dose. Administered activity for cycle 2 can then be modulated for a particular dosimetry approach or another fixed dose given if appropriate. Imaging following cycle 2 can be used in the same process to inform cycle 3. Image reproduced from Lawhn-Heath et al, 2022.

Lesional dosimetry involves delivery of a predetermined radiation dose to the tumor, as a tumor dose-response relationship has emerged in several patient TRT trials [10, 136]. This approach is most frequently used for ^{90}Y selective internal radiation therapy (SIRT), in which ^{90}Y -loaded microspheres are injected into the hepatic artery to selectively irradiate unresectable liver tumors or hepatic colorectal tumor metastases [137]. In this context, a dose-response relationship has been firmly established [138], and the phase II DOSISPHERE-01 trial (NCT02582034) indicated that patients receiving personalized lesional dosimetry for SIRT demonstrated a significantly enhanced objective response rate than those receiving a predetermined dose to the

perfused lobe [139]. As TRT is given systemically, delivery of the prescribed dose to each tumor will result in off-target toxicities, so a trade-off of less aggressive dosing for reduced toxicity in particular patients will be necessary. As mentioned previously, synergy of TRT and ICI has been demonstrated preclinically for a prescribed tumor absorbed dose (2.5 - 5 Gy) [98]. In this work, lesional dosimetry to determine the administered activity needed for the equivalent tumor absorbed dose was performed for combination with ICI, as detailed in later sections.

Maximum targeted activity (MTA) dosimetry seeks to administer the highest activity achievable while preventing toxicity to non-target tissues [8]. Pharmacokinetics from imaging is used to estimate radiation doses to sensitive organs, namely the kidneys, or the whole-body dose. This is much more difficult for distributed tissues that may not have significant discrete uptake (ex. bone marrow) than for ‘distinct’ organs (ex. the kidneys). Frequently, serial measurement of blood or plasma radioactivity as part of a multicompartiment model containing contributions from the whole body imaging and representative bone (ex. femur) activities has been used as a proxy for bone marrow [140]. There is no consensus about the maximum dose limits for specific organs [8]. These dose limits may be drawn from clinical toxicity studies with ^{131}I in thyroid cancer patients performed in the 1960s [141] with or without adjustment for more recent dosimetry data [142], or they may be taken from the clinical radiotherapy literature [143] such that they are not suitable for TRT. For instance, an often-cited dose limit borrowed from radiotherapy for the kidney is 23 Gy, but in a trial where more than 170 patients who received ^{177}Lu -DOTATATE had this limit exceeded, none demonstrated significant kidney toxicity [144]. By contrast, bone marrow toxicity is common after the standard ^{177}Lu -DOTATATE regimen (7.4 GBq (200 mCi) x 4 cycles) [55] although the accepted 2-3 Gy marrow dose is rarely reached [8]. As aforementioned, bone marrow toxicity due to PRRT is generally mild and reversible, although in rare cases chronic but

delayed marrow dysfunction (myelodysplastic syndrome, myelosuppression, acute myeloid leukemia) can emerge at marrow doses greatly below these limits [57, 145]. However, PRRT trials with dosimetry-informed activity adjustment have used the MTA approach for maximum dose to the kidney rather than the bone marrow [9, 135, 146]. This is for three main reasons: marrow dose is much less straightforward to determine from imaging than kidney dose, renal toxicity is more likely to be permanent, and earlier precedent as PRRT with ^{90}Y demonstrated more renal toxicity than ^{177}Lu PRRT [57, 145].

1.3.4 Phantom (OLINDA) vs Radiation Transport Dosimetry (ex. Torch)

Organ Level Internal Dose Assessment/Exponential Modeling (OLINDA/EXM) utilizes user-supplied biokinetic data to simulate TRT pharmacokinetics and calculate doses experienced by particular organs. TIA coefficients, or the total number of disintegrations in the source organs, are used as inputs. Organ level S-values particular to a source-target organ pair and radionuclide previously determined from Monte Carlo simulation within standardized anthropomorphic phantoms of humans (adults, children, pregnant women) and rodents (mice, rats) are sourced from lookup tables. Dose to each organ is calculated as the product of the TIA coefficient and S-values, acknowledging spill-in from the other organs. Radioactivity is assumed to be distributed homogeneously within an organ, and tumors are modeled as separate unit-density spheres (only ‘self-dose’ is considered). Decay data for more than 1200 radionuclides are adapted from the International Commission on Radiological Protection (ICRP) Publication 107. Extensive discussion of the mechanisms and phantoms involved in the software has been detailed elsewhere [147].

Internal dosimetry software utilizing Monte Carlo simulation of radiation transport such as Torch performs dose calculations within ROIs determined from subject images. The heterogeneous distribution of the agent is captured as 3D dose distributions are calculated at the voxel level. Dose spill-in to the tumor and the tumor contribution to doses experienced by other organs is considered. As such, this improves the prediction quality of metrics more meaningful to understanding the tumor dose response to TRT than the absorbed dose, such as the biological effective dose (BED) [148]. Further, therapy dose selection from imaging can be conducted rationally using the actual organ geometries of the mice of interest. Details regarding Torch functionality and validation are provided in the following section.

1.3.5 Radiation Dosimetry Software Packages

For simplicity, the following discussion of dosimetry software includes only those that are commercially available and excludes OLINDA/EXM and products specific for SIRT dosimetry. They are listed in alphabetical order.

1.3.5.1 GE Dosimetry Toolkit and Q.Thera AI (GE Healthcare)

The GE Dosimetry Toolkit utilizes serial whole-body planar scans, SPECT/CT images, or hybrid SPECT/planar scanning to determine patient organ TIAs and mean absorbed doses [149]. It is suitable for ^{131}I thyroid cancer therapy, ^{177}Lu therapies, and ^{90}Y SIRT. SPECT/CT images are first reconstructed, with correction for patient movement and soft tissue artifacts (attenuation, scattering). The serial images are then registered to a reference image either semiautomatically or manually, followed by contouring to define ROIs for activity and TIA calculations. Time-activity

curves are fit to exponential functions and can be output as Microsoft Excel files or for use in OLINDA/EXM.

Q.Thera AI performs automatic registration and contouring of organs and tumors and provides their uptake as percent injected dose. The time-activity curves of the ROIs are fit to exponential functions that are integrated either analytically or via the trapezoidal method. Absorbed doses per organ are calculated for the radionuclide, reference phantom model (from newborn to adults), source-region TIAs, and if desired, organ volumes. Normalization for patient body mass occurs by scaling of the reference phantom total body and internal organ masses. Absorbed dose contribution from distant blood and other organs (self-irradiation) can be calculated as unit-density spheres.

1.3.5.2 MIM Software

MIM software for image viewing and analysis contains a dosimetry program (MIM SurePlan) optimized for SPECT/CT. Attenuation and scatter correction are applied in image reconstruction, and ROI contouring for absorbed dose determination can be performed automatically with an artificial intelligence algorithm that is FDA-approved [149]. From longitudinal SPECT images, a composite image is formed by aligning information within and surrounding contoured areas. The composite image is validated against manual registration of the images such that the TIAs for the ROIs are within 1% of one another. With β^- -emitters that lack γ emissions (^{90}Y), dosimetry can be conducted using bremsstrahlung SPECT (photons produced by β^- interaction with tissue) or PET images. Either the local deposition method (emissions in the voxel stay in the voxel, the absorbed dose per voxel is the product of the activity concentration and a constant [150]) or voxel S-value dose kernel convolution can be used. Standard SPECT/CT

with ^{131}I , ^{177}Lu , and others enables S-value voxel dose kernel convolution dosimetry. This can be conducted with a single SPECT/CT, longitudinal SPECT/CT scans, or hybrid SPECT/planar scans. TIAs are calculated via one of several exponential functions or trapezoidal integration with exponential terms. For longitudinal SPECT/CT scans, integration can be applied at either the voxel or organ levels. For hybrid SPECT/planar imaging, the planar data is used for integration, with scaling from SPECT. Planar imaging can be corrected for attenuation, scattering, and background. Towards avoiding the difficulties for both patients and clinicians required for multiple-timepoint dosimetry, MIM is developing two tools for single-timepoint dosimetry with ^{177}Lu -DOTATATE – the *a priori* information approach and the Hänscheid approach. The *a priori* approach uses time-activity curves generated from longitudinal SPECT/CT scans of the patient during a previous therapy cycle, whereas the Hänscheid approach assumes an exponential time-activity curve from a pretherapy scan [151].

1.3.5.3 PLANET Dose (DOSIsoft)

PLANET Dose is FDA-approved for ^{90}Y SIRT and CE (Conformité Européenne, abides by health and safety standards of the European Union)-marked for particular isotopes (^{90}Y , ^{177}Lu , ^{131}I) in TRT protocols [149]. Compatible imaging modalities include CT, PET/SPECT, and γ -cameras, as well as MRI (magnetic resonance imaging). Images can be corrected to reduce partial volume effects, an unavoidable phenomenon in PET and SPECT in which the observed intensity and activity distribution of an ROI differs from reality due to signal spillover and limited image spatial resolution possible with the detector [152]. Registration of sets of CT and PET or SPECT images and their associated ROIs is achieved by either the rigid or deformable method. Rigid registration involves the superposition of the input image (ex. PET, SPECT) to the reference image

(ex. CT) according to shared points or surfaces such that the pixel-to-pixel relationship is unchanged by transformations [153]. Deformable registration allows for the pixel-to-pixel relationship to change, apt for cases of anatomical variation (tumor regression, weight loss, apparent changes in organ shape). Registration can be performed either manually or semiautomatically with the selection of anatomic reference points guided by fiducial markers in the field of view. Integration of time-activity curves can be conducted by fitting to exponential or affine functions for integration or can be integrated by the trapezoidal method. Voxel S-values are used to calculate absorbed doses, with correction for variation in tissue densities available. This correction is to compensate for the assumption of uniform tissue density required for efficient calculation speed with the dose point kernel used [128].

1.3.5.4 PMOD (PMOD Technologies LLC)

PMOD is designed to perform automated preprocessing of serial images to determine input values for dosimetry analysis [149]. The images are first merged, followed by the creation of organ ROIs either from an isocontour (line formed from voxels with the same value), manual or semiautomatic (ex. thresholding) contouring, or from the matched anatomical image. ROIs can individually be attributed to a particular reference phantom, and their activity concentrations are modeled as time-activity curves. These time-activity curves are then integrated by either rectangular or trapezoidal integration prior to radionuclide decay, which is modeled as exponential functions and/or analytic integration. Output TIAs are compatible with OLINDA/EXM as well as IDAC, a similar program that instead utilizes specific absorbed fractions (fraction of energy emitted from the source region absorbed by the target region, divided by the target mass) and calculation methods proposed by the ICRP rather than the MIRD framework [154].

1.3.5.5 Rapid

Rapid's proprietary RPTDose software is suitable for both phantom and patient-specific 3D dosimetry, underpinned by a Monte Carlo-based algorithm to determine activity distribution and pharmacokinetics [149]. It consists of two main packages, one that performs SPECT reconstruction with attenuation and scatter correction, and one that performs electron γ -shower Monte Carlo simulations within patient CT-defined anatomies, with quantitative activity data from longitudinal SPECT. The first has been validated for a substantial number of radionuclides (^{90}Y , $^{99\text{m}}\text{Tc}$, ^{111}In , ^{131}I , ^{223}Ra , and ^{227}Th , among others) from both Monte Carlo simulations and actual phantoms. The dose mapping program determines dose rates per ROI, which are fit by the non-least squares method to model functions, and absorbed doses are derived as the area under the dose rate curve from 0 to infinity.

Rapid has also created and validated the web-based dosimetry software 3D-RD-S, which is currently pending FDA clearance. 3D-RD-S utilizes phantoms, radionuclide decay data for more than 1200 isotopes, and specific absorbed fractions for numerous source and target regions – all proposed in ICRP publications. Tumors are modeled as spheres, and tumor self-dose can be determined for 5 compositions and 10 diameters up to 12 cm. Intriguingly, the program allows for dose calculation of α -emitters and their daughters, and the user can indicate whether the daughters have the same assumed distribution as the parent, a distribution scaled to it, or an unrelated distribution. Currently, Rapid is developing another package for SPECT reconstruction of therapeutic radionuclides not amenable to imaging, namely α -emitters. These data then could be directly loaded to 3D-RD-S.

1.3.5.6 Torch (Voximetry Inc)

Torch is currently the only commercially available software that performs full 3D Monte Carlo simulation of radiation transport (contributions from electrons and photons) [155], enabled by a proprietary parallel processing algorithm run through a graphics processing unit to expedite calculations [149]. An image dataset or datasets per timepoint are first imported, registered automatically (although this is adjustable by the user), and are populated by ROIs defined elsewhere. If using multiple-timepoint dosimetry, the user can import ROI sets for each timepoint or the first timepoint ROI set can be propagated to the other timepoints via proprietary deformable registration algorithms. Torch received FDA 510(k) clearance on November 28, 2022.

TIA calculation from time-activity curves is conducted with the Akaike information criterion [149], a statistical metric that aims to optimize model selection for a particular dataset by minimizing both prediction error and the number of model parameters [156]. Torch automatically determines the best-fitting function and its parameters, which the user can accept or adjust.

Monte Carlo dose planning utilizing the TIAs occurs next. Electron transport is modeled via the condensed history method, in which many electron collisions are approximated as a ‘step’ over a specified path length [157], and energy transfer is modeled differently according to its magnitude (high or low). Following each step, electron distribution is determined from multiple scattering theory, which describes the dispersion of a wave through a set of obstacles. Photon transport is encompassed in such a way that particle physics phenomena are accounted for. The calculated distribution can then be assessed by dose statistics and dose-volume histograms (relationship of absorbed dose to tissue volume). Dose volumes may be output in formats compatible for visualization in other software, such as those used in EBRT.

Torch has been thoroughly benchmarked with both physical and computational phantoms. The algorithm was validated against the widely used Monte Carlo Geant4 code for both voxel S-value dose kernels in water and patient data with a number of isotopes, namely ^{90}Y , ^{131}I , ^{177}Lu , and ^{223}Ra . Data from the OpenDose collaboration, an open-access resource for dosimetry data and Monte Carlo calculation programs [158], has also been implemented to benchmark Torch. Further, calculated values in Torch for ICRP-sourced adult male and female phantoms for various isotopes have demonstrated within 5% agreement for all source-target region pairs. Estimates from Torch and measurements with radiochromic film for ^{90}Y dose distributions in a water phantom have also shown impressive agreement.

1.4 Motivation and Specific Aims

As stated previously, TRT has demonstrated profound potential for the selective treatment of cancer, as exemplified by the clinical adoption of ^{177}Lu -DOTATATE (Lutathera®) and ^{177}Lu -PSMA-617 (Pluvicto™). This is enhanced even further by combination with ICI therapies, which can allow for substantial responses in patients who do not respond to either alone. However, the development of individualized treatment TRT regimens has lagged, as in the clinic TRT is usually given at a standardized dose for a predetermined number of cycles. This likely subjects patients either to unnecessary toxicity or results in undertreatment. Dosimetry utilizing the MIRD formalism (OLINDA/EXM) of S-values (absorbed dose rate per unit activity) has been adopted in some clinical settings but is likely inadequate as it relies on the assumption of standardized organ masses and homogenous activity distribution in organs. Monte Carlo simulation of radiation transport (calculations based on particle interactions) is better suited to patient-specific tumor and

organ geometries as it accounts for heterogenous activity distribution and secondary particle generation. Several dedicated software packages are available.

Melanoma is a life-threatening form of skin cancer that accounts for only 1% of diagnosed skin cancers but is responsible for the vast majority of skin cancer morbidity and mortality [159]. In the United States, melanoma incidence has more than tripled from 1975 to 2018, mainly among fair-skinned populations. An estimated 90,000 new cases were diagnosed in 2022, with an approximate 10% mortality rate [160]. Although patients have favorable outcomes with surgical excision when localized [75], melanoma often metastasizes preferentially to the lungs, liver, and brain [161]. As such, the 5-year survival rate falls from 99% when localized to 30% when disseminated, according to American Cancer Society figures [162]. ICI, particularly dual ICI (nivolumab anti-PD-1 and ipilimumab anti-CTLA-4) has demonstrated substantial benefit in melanoma [163-165], yet up to 40% of patients may not respond to dual ICI [163]. Approximately 50% of clinical melanomas express the BRAF^{V600E} mutation, which causes hyperactivity of the B-raf proto-oncogene serine/threonine kinase, leading to constitutive activation of the protumor mitogen-activated protein kinase (MAPK) signaling pathway [166]. The BRAF mutation is druggable with targeted small molecule therapies, and combination with inhibitors to MEK, a related kinase of the MAPK pathway, improves response rate and median survival [167, 168]. However, responses are short-lived due to acquired resistance [169]. Due to evidence of proinflammatory effects with BRAF and MEK inhibitors, triple BRAF inhibitor + MEK inhibitor + ICI combination trials have been conducted, with extension of median progression-free survival from about 11 months to about 16 months [170, 171]. Those receiving ICI following progression on combined BRAF and MEK inhibitors demonstrated minimal disease control (stable disease or

better) [172], although treatment sequencing is an area of investigation. Given this, new salvage options must be explored for the subset of patients that progress on both targeted therapy and ICI.

The objective of this dissertation is to validate the use of image-guided dosimetry leveraging the theranostic $^{64/67}\text{Cu}$ pair towards more individualized TRT. To further enhance TRT effectiveness, TRT doses determined from dosimetry are paired to dual ICI (anti-CTLA-4 and anti-PD-L1). The VLA-4 targeted peptidomimetic LLP2A conjugated to the copper chelator TE1A1P is administered in a subcutaneous mouse model of BRAF^{V600E}-mutant melanoma labeled for either pretherapy imaging or TRT. Our previous work with ^{64}Cu -TE1A1P-LLP2A (^{64}Cu -LLP2A) for melanoma PET/CT imaging involved the widely used B16F10 line [77], which expresses wild-type BRAF [173], among other differences from more clinically-relevant models. Instead, two BRAF^{V600E} cell lines that better recapitulate human melanoma and that have attained resistance to the BRAF inhibitor dabrafenib in culture are used. As the parental cell line BPR lacks the β_1 subunit of VLA-4, the BPR line was transduced with the α_4 subunit to simulate a more aggressive VLA-4^{hi} clone (BPR α). This dissertation hypothesizes that image-guided TRT with LLP2A as a vector is achievable in a model of aggressive, therapy-resistant clinical melanoma, with therapeutic benefit further increased with ICI.

To evaluate this central hypothesis, this dissertation examined the following Specific Aims:

1.4.1 Specific Aim 1

Overall Goal: Validate differential ^{64}Cu -LLP2A uptake and PET signal in BRAF^{V600E} mouse melanoma models that vary in VLA-4 expression

Hypothesis: ^{64}Cu -LLP2A uptake is selective for the VLA-4⁺ BPR α model and much more prominent relative to the VLA-4⁻ BPR model

Objectives of Specific Aim 1:

- 1) Compare selectivity and binding metrics of LLP2A for VLA-4⁻ BPR parent and transduced derivative line BPR α (intact VLA-4) *in vitro*
- 2) Determine *in vitro* whether intact VLA-4 is required for internalization of ⁶⁴Cu-LLP2A by the melanoma lines, and compare to the BRAF wild-type B16F10 line
- 3) Quantify and compare ⁶⁴Cu-LLP2A pharmacokinetics in murine subcutaneous BPR and BPR α tumor models via PET imaging and biodistribution assays

1.4.2 Specific Aim 2

Overall Goal: Compare therapeutic efficacy of ⁶⁷Cu-LLP2A TRT + dual ICI at two TRT dose levels informed from ⁶⁴Cu-LLP2A PET/CT imaging and evaluate TRT toxicity.

Hypothesis: ⁶⁷Cu-LLP2A dosimetry using Torch software is well-matched to the ⁶⁷Cu-LLP2A biodistribution results. Tumor dose delivery of 2.5 Gy (700 μ Ci administered) is optimal for efficacy with minimized toxicity when combined with dual ICI.

Objectives of Specific Aim 2:

- 1) Evaluate ⁶⁷Cu-LLP2A dosimetry (prescribed dose) to the tumor and organs of interest from ⁶⁴Cu-LLP2A PET/CT images via the voxelized Monte Carlo software Torch. Compare the results to the more widely-used and phantom-based OLINDA software.
- 2) Perform ⁶⁷Cu-LLP2A biodistribution assay in a subcutaneous BPR α model to compare to the Aim 1 ⁶⁴Cu-LLP2A biodistribution and to corroborate dosimetry.
- 3) Utilize the Torch prescribed dose from Subaim 1 to deliver two levels of ⁶⁷Cu-LLP2A tumor absorbed dose in a subcutaneous BPR α model as part of a therapy study in combination with dual ICI.

2.0 Specific Aim 1: Validate differential ^{64}Cu -LLP2A uptake and PET signal in BRAF^{V600E} mouse melanoma models that vary in VLA-4 expression

As stated previously, this work was published in *Molecular Imaging and Biology*: **Bellavia, M.C.**, et al., *PET Imaging of VLA-4 in a New BRAF(V600E) Mouse Model of Melanoma*. *Mol Imaging Biol*, 2022. **24**(3): p. 425-433.

2.1 Introduction

Over the last decade, immune checkpoint blockade has drastically altered the prognosis and medical management of patients with metastatic melanoma. Response rates to dual checkpoint blockade are as high as 50-70% in treatment-naïve melanoma patients, with approximately 25% of patients achieving durable complete responses [163, 164, 174]. In addition to checkpoint blockade, small molecule therapies targeting activating mutations in the BRAF kinase (i.e. BRAF^{V600E}, identified in approximately 50% of cases) have been commonly applied [166]. Combining BRAF inhibitors (BRAFi) (vemurafenib, encorafenib) with inhibitors to MEK (binimetinib, trametinib), another kinase of the MAPK signaling cascade, substantially improves response rates in treatment-naïve patients [167, 168]. Despite these advances in immunotherapies and targeted therapies for the treatment of metastatic melanoma, tumor escape, drug resistance, and treatment-associated toxicities remain problematic for many patients [175, 176]. Notably, patients with BRAFi-resistant melanomas display low response rates to immune checkpoint

blockade [177, 178] and there remains a major unmet clinical need to improve outcomes in this patient population.

Very late antigen-4 (VLA-4, integrin $\alpha_4\beta_1$) is a surface adhesion protein that facilitates the growth and metastasis of melanomas and other malignancies by enhancing tumor angiogenesis and the extravasation of circulating tumor cells into pre-metastatic niches [179]. In melanoma patients, upregulated tumor expression of VLA-4 is a prognostic marker for metastasis [74]. As VLA-4 is also involved in lymphocyte differentiation, trafficking, and homing (via binding to VCAM-1 expressed on the vascular endothelium [180]) in addition to its immunomodulatory properties [181], VLA-4 is a particularly attractive target for imaging and therapeutic intervention.

We previously demonstrated that progressively-growing murine BRAF wild-type VLA-4⁺ B16F10 melanomas readily take up the VLA-4 specific peptidomimetic LLP2A (IC₅₀: 2 pM [41]) labeled with radioisotopes Ga-68 and Cu-64 for PET and that LLP2A labeled with the β^- -emitter Lu-177 mediates anti-tumor efficacy as a therapeutic agent in this model [42, 77, 78]. However, B16F10 does not exhibit common oncogenic mutations/deletions associated with the development of most human melanoma [173]. For example, these cells express wild-type *PTEN*, whose loss from chromosome 10 is implicated in human melanomagenesis [182]. Hence, to test LLP2A-based therapeutic agents in translational models that more faithfully recapitulate human disease, we have now developed BRAF^{V600E}PTEN^{-/-}, BRAFi-resistant melanoma models with or without substantial expression of the target antigen VLA-4 (i.e. BPR and BPR α). These BRAFi-resistant melanoma models are expected to support translational research advances and the development of novel imaging and targeted radiotherapeutic approaches for more effective treatment and monitoring of patients with advanced-stage disease.

2.2 Materials and Methods

All chemicals were purchased from Sigma-Aldrich (St. Louis, MO) or Fisher Scientific (Waltham, MA), unless otherwise specified. Reagents, instrumentation, and additional characterization procedures are detailed in Appendix A.

2.2.1 Cell Line Generation

BPR cells were selected from the BRAF^{V600E} PTEN^{-/-} BP melanoma line [183] kindly provided by Dr. Jennifer Wargo (University of Texas M.D. Anderson Cancer Center, Houston, TX), that acquired stable resistance to the BRAF inhibitor (BRAFi) dabrafenib (20 μ M) after 1 month *in vitro* culture [184]. As flow cytometry analyses conducted in the Storkus lab indicated that BPR cells were deficient in VLA-4 expression (BPR cells only express CD29, the β_1 subunit), they were transduced to express high levels of the α_4 subunit (CD49d) via infection with a recombinant lentiviral vector (Itga4 (NM_010576), CAT#: MR211489L1V, OriGene Technologies, Rockville, MD), generating the BPR α cell line. The cell lines were authenticated by IDEXX BioAnalytics (Columbia, MO) and verified as Mycoplasma-free by in-house PCR. Cells were maintained in DMEM culture medium supplemented with 10% FBS with (BPR, BPR α) or without (B16F10) additional 1% L-glutamine. BPR α cells were selected for purity by flow sorting based on expression of CD49d using a BD FACSAria IIu (BD Biosciences, San Jose, CA).

2.2.2 Peptide Synthesis and Radiolabeling

Cy3-LLP2A synthesis was conducted as reported previously [185]. Cy3-LLP2A (Figure 15) was synthesized by the Molecular Interactions Core at the University of Missouri. CB-TE1A1P-PEG₄-LLP2A was radiolabeled with Cu-64 (⁶⁴Cu-LLP2A) at a specific activity of 1 mCi/μg. The reactants were combined in 0.5 M NH₄OAc buffer pH 6.5 and incubated at 70°C for 30 min under shaking.

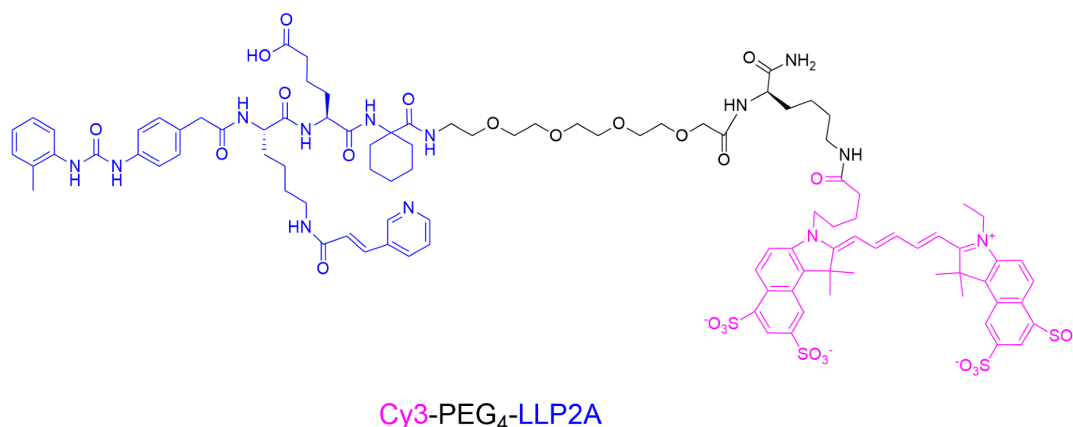


Figure 15 Molecular structure of Cy3-PEG₄-LLP2A, the fluorescent counterpart to ⁶⁴Cu-LLP2A.

2.2.3 Flow Cytometry Validation of Cy3-LLP2A

Cells in culture were harvested with trypsin and large clumps were excluded via 70 μm cell strainers (Fisher Scientific, Waltham, MA). BPR and BPR α cells (1×10^5) in 0.1 mL ice-cold flow buffer (1x PBS, 0.1% BSA) received either 1 μg Cy3-LLP2A, 0.25 μg anti-CD49d-PE, or isotype control (both BioLegend, San Diego, CA) in 50 μL staining buffer (1x PBS, 1% BSA, 1 mM Mn²⁺). Cells were incubated on ice for 30 min and washed in flow buffer twice prior to analysis.

2.2.4 Cell Binding Assays

To discern differences in the binding affinity of ^{64}Cu -LLP2A to BPR and BPR α cells, cell binding assays were performed as previously described [77], with modifications. Briefly, cells were seeded in 12-well plates (1×10^5 per well) for 24h after the plates were coated with 0.1% gelatin to allow cell adherence to the plate. Multiple wells coated with 0.1% gelatin without cells were included as background for protein quantification. Subsequently, the cells were washed twice with 1 mL HBSS, followed by addition of 0.5 mL of binding medium (HBSS, 0.1% BSA, 1 mM Mn^{2+}) per well. For both cell lines, 15 μg LLP2A-PEG₄ was used as a cold block to estimate *in vitro* nonspecific binding, and ^{64}Cu -LLP2A was added in increasing concentrations (1 nM - 100 nM). The plates were incubated on ice for 2h and the radioactive medium was removed. Cell pellets were dissolved in 0.5% sodium dodecyl sulfate (SDS) solution after rinsing twice with 1 mL of ice-cold binding buffer. Bound radioactivity following incubation was measured by γ -counting (PerkinElmer 2470 WIZARD², Waltham, MA). The protein content of the cell lysates was determined by BCA assays (Pierce BCA Protein Assay Kit, ThermoFisher Scientific, Waltham, MA) and cell protein content was calculated by subtracting the protein content of 0.1% gelatin in the absence of the cells from the protein content in the presence of the cells and 0.1% gelatin. Lysate radioactivity was normalized to the amount of cellular protein present (fmol/mg). Experiments were conducted in triplicate in different 12-well plates. The dissociation constant K_d and total receptor number B_{max} were determined with GraphPad Prism 9 software (San Diego, CA).

2.2.5 ⁶⁴Cu-LLP2A Internalization Assays

Internalization assays were performed to compare the uptake of ⁶⁴Cu-LLP2A in VLA-4⁻ BPR and VLA-4⁺ BPR α and B16F10 cells. For each cell line, 1 x 10⁵ cells were seeded per well in 12-well plates and incubated 24h prior to the experiment. Cells were first washed twice with 1 mL DMEM and then received 1 mL assay media (DMEM, 1% BSA, 1 mM Mn²⁺). To quantify non-specific internalization, triplicate wells per cell line were blocked with excess (10 μ g) LLP2A-PEG₄ and incubated for 15 min at 37°C. Cells received 0.44 MBq (12 μ Ci; 3.43 MBq/nmol) ⁶⁴Cu-LLP2A per well prior to incubation at 37°C. At each time point (15 min, 2h, 4h), the assay media was removed, and cells were washed twice with DMEM. The surface-bound fraction was removed by the addition of DMEM containing 20 mM sodium acetate (pH 4.0) followed by incubation of the plates for 10 min at 37°C. Total cellular protein was harvested for analysis by dissolution in 1 mL 0.5% SDS. Sample radioactivity per cell pellet was determined by γ counting (PerkinElmer 2470 WIZARD²). Internalized activity was corrected for background, activity in the corresponding blocked sample, and time-dependent decay. The corrected activity was then normalized to total cellular protein collected (fmol/mg protein) after quantification of the cellular lysate protein via BCA assay.

2.2.6 Animal Studies

Four- to six-week-old male and female C57BL/6 mice were obtained from the Jackson Laboratory (Bar Harbor, ME). All applicable institutional and/or national guidelines for the care and use of animals were followed. For PET/CT imaging and biodistribution experiments, mice

were inoculated subcutaneously in the right flank with 5×10^5 BPR or BPR α cells mixed with an equal volume of Matrigel (Corning Life Sciences, Tewksbury, MA).

2.2.7 PET/CT Imaging and Analysis

C57BL/6 mice bearing subcutaneous BPR or BPR α tumors (n=9 each, 3m/6f) were injected intravenously (lateral tail vein) with ^{64}Cu -LLP2A (7.4 MBq [200 μCi]; 57.2 MBq/nmol). At 4 and 24h post-injection, mice were anesthetized with 2% isoflurane, and small animal PET/CT images were acquired as static images collected over 10 min with an Inveon PET/CT scanner (Siemens Medical Solutions, Knoxville, TN). PET and CT images were co-registered and PET images were reconstructed with an Ordered Subsets Expectation Maximizing 3D algorithm (OSEM-3D) with Inveon Research Workstation (IRW) software (Siemens Medical Solutions, Knoxville, TN). Regions of interest (ROI) were drawn from CT images, and the corresponding PET activities were calculated using IRW software. Standard uptake values (SUVs, normalization of region activity to volume, generally body weight) at time t were calculated via the formula: $\text{SUV}(t) = \text{image-derived activity concentration (Bq/mL)} \times [\text{animal weight (g)/injected dose (Bq)}]$.

2.2.8 Biodistribution Experiments

Immediately following the 24h PET/CT imaging time point, BPR and BPR α tumor-bearing mice (n=6; 3m/3f) were euthanized. To observe the time course of the tracer biodistribution in BPR α , BPR α tumor-bearing mice were euthanized at 4h (n=3) and 48h (n=4) post-tracer injection at an equivalent dose in separate experiments (Appendix A). Blood, muscle (gastrocnemius of

uninvolved leg), bone, heart, lungs, spleen, kidney, liver, intestines, thymus, and tumor were harvested, weighed, and the activity counted with a γ counter (PerkinElmer 2470 WIZARD²). The percent injected activity per gram of tissue (%IA/g) was calculated by decay correction of each sample normalized to a standard of known weight containing activity corresponding to the injected dose.

2.2.9 Statistics

Statistical analyses were performed using GraphPad Prism 9 software (San Diego, CA). Groups were compared using two-tailed student t-test or one-way ANOVA with Tukey's HSD for multiple comparisons. A p-value < 0.05 was considered statistically significant. Outliers as determined by two-sided Grubbs' test ($\alpha = 0.05$) [186] were removed from analysis.

2.3 Results

2.3.1 Generation of BPR α and Flow Cytometry Validation of Cy3-LLP2A

BPR cells only express the β_1 subunit (CD29) of VLA-4, so to simulate a more aggressive variant of these BRAFⁱ-resistant melanomas, the cells were transduced with the α_4 subunit (CD49d) using recombinant lentiviral particles to express high levels of VLA-4 (BPR α). To verify α_4 induction and to isolate transduced clones, flow sorting was conducted. Approximately 70% of the resulting cells stained positively for both CD49d (α_4) and CD29 (β_1) and were collected for further propagation as the stable cell line designated BPR α (Figure 16). LLP2A selectivity to the

parental and transduced lines was assessed using Cy3-LLP2A as a flow cytometry probe on BPR α vs. BPR cells. Although some staining of the probe was observed for VLA-4⁻ BPR cells, the median fluorescence intensity of staining on BPR α cells was significantly greater ($p < 0.0001$, Figure 17).

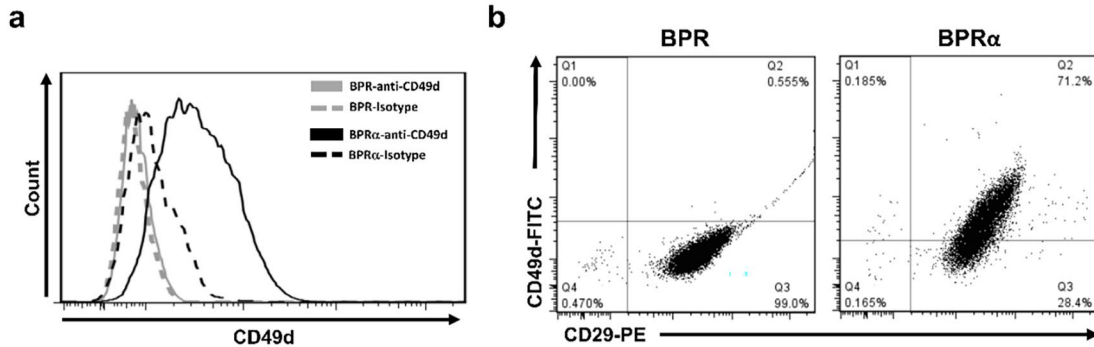


Figure 16 BPR α cells were selected by flow cytometry. (a) Transduction of CD49d into BPR melanoma cells. Murine BPR (Braf^{V600E}/Pten^{-/-}/dabrafenib-resistant) melanoma cells were transduced with a lentiviral vector (OriGene Technologies) encoding the mouse integrin α_4 subunit (CD49d), generating BPR α cells. BPR wild-type (gray) and BPR α (black) cells were stained with FITC-labeled anti-CD49d (solid line) or isotype control (dashed line) antibodies. The expression of CD49d on the cell surface was then analyzed by flow cytometry. (b) The BPR and BPR α cells were stained with FITC-labeled anti-CD49d and PE-labeled anti-CD29 antibodies and analyzed for VLA-4 (CD49d⁺CD29⁺) expression by flow cytometry. BPR cells are CD49d⁻CD29⁺ whereas approximately 70% of BPR α cells are CD49d⁺CD29⁺ (VLA-4 positive).

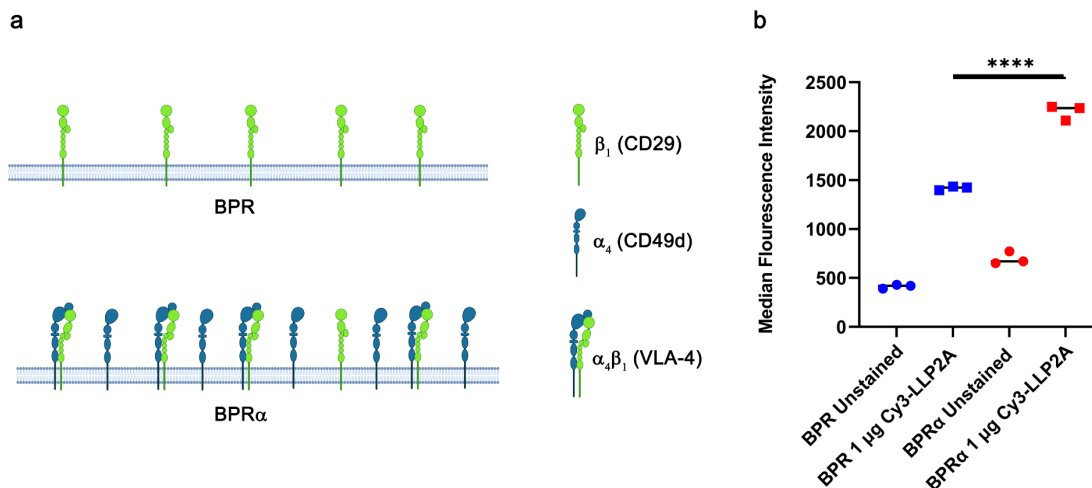


Figure 17 Cy3-LLP2A staining of BPR and BPR α cells by flow cytometry. (a) BPR cells natively express only the β_1 subunit (CD29) of VLA-4; however, both α_4 and β_1 subunits are required for LLP2A binding. Therefore, BPR cells were transduced with the α_4 subunit of VLA-4 (CD49d) to generate BPR α (VLA-4/integrin $\alpha_4\beta_1^+$). (b) Flow cytometry indicates that LLP2A requires intact VLA-4 for appreciable binding. Median fluorescence intensity of Cy3-LLP2A-stained and unstained BPR and BPR α . At least 10,000 events were analyzed per replicate, and each point represents an individual sample. ****: $p < 0.0001$, by unpaired t-test.

2.3.2 Radiolabeling Chemistry

The radiochemical purity of ^{64}Cu -LLP2A was >99% (Figure 18) and a molar activity of 57.2 MBq/nmol (1 mCi/ μg LLP2A) was utilized for all applicable studies. We have previously demonstrated ^{64}Cu -LLP2A stability in human serum, with negligible binding of the conjugate to plasma proteins [77].

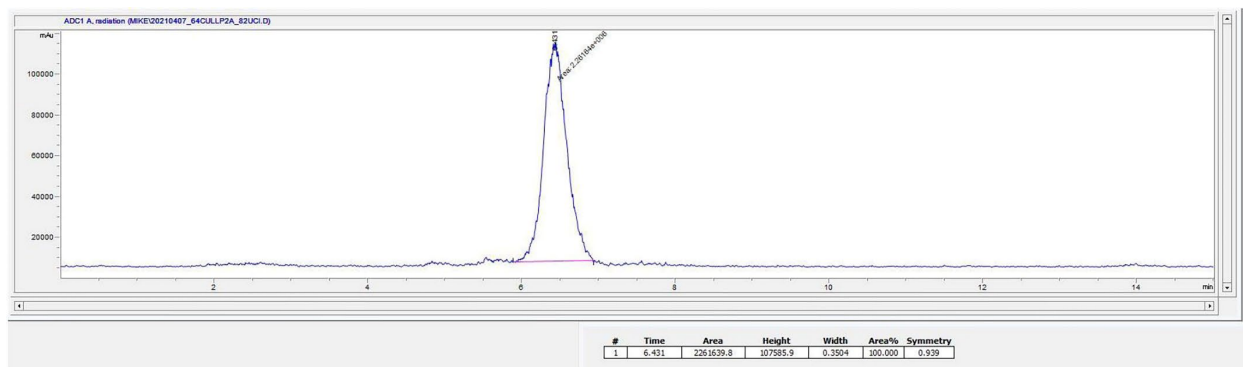


Figure 18 Radio-HPLC chromatogram of ^{64}Cu -LLP2A (82 μCi , blue line). The range of peak interpolation is indicated by the pink line. For this column and protocol, free ^{64}Cu would appear around 2 min.

2.3.3 ^{64}Cu -LLP2A Cell Binding Assays in BPR and BPR α Cells

To interrogate differences in LLP2A binding affinity to BPR and BPR α cells, saturation binding assays were conducted by Dr. Van Ho, then a postdoctoral associate under Dr. Carolyn Anderson. ^{64}Cu -LLP2A was competed with PEG₄-LLP2A at 4°C. Representative saturation binding curves of ^{64}Cu -LLP2A to BPR and BPR α cells (Figure 19) indicate significant binding affinity to the VLA-4⁺ BPR α cells (K_d : 1.4 ± 0.45 nM), whereas in VLA-4⁻ BPR cells, no saturation occurs, as total binding cannot be differentiated from non-specific (blocked) binding. The BPR α B_{max} was 145 ± 8.8 fmol/mg, while the BPR B_{max} was not interpretable (although metrics can be calculated, the model fit is poor; $R^2=0.0002$). These observations suggest that α_4 is not present in BPR and that LLP2A binding is specific only to BPR α cells given their expression of intact VLA-4.

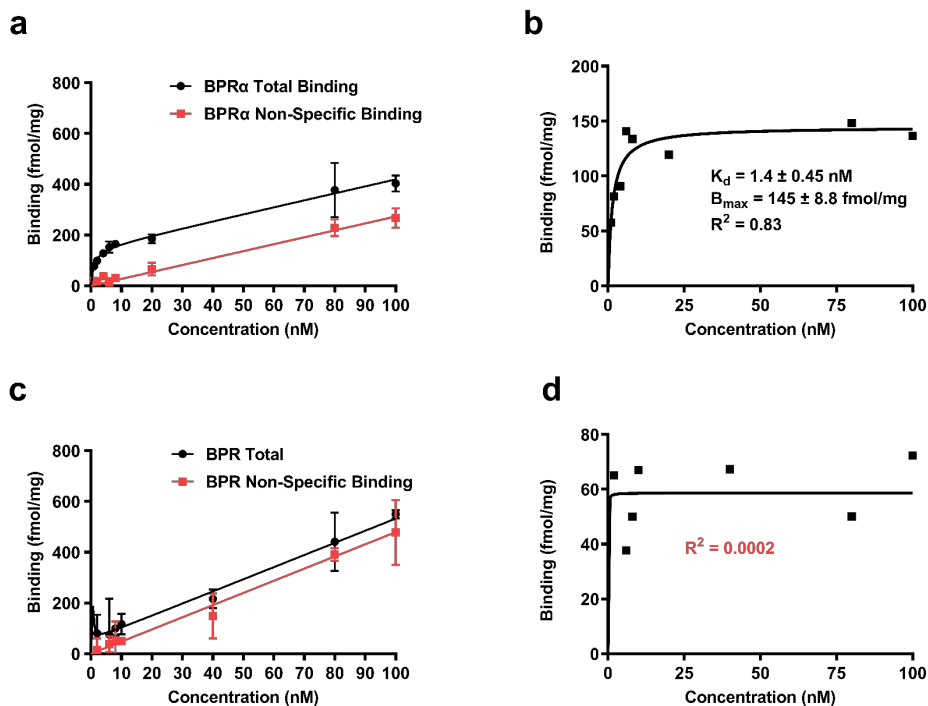


Figure 19 Saturation binding data of ^{64}Cu -LLP2A in (a,b) BPR α and (c,d) BPR. (a) Overall and (b) specific binding isotherms of BPR α . (c) Saturation is not reached for BPR, as total (non-specific + specific) and non-specific binding alone are essentially indistinguishable. (d) A specific binding isotherm cannot be properly fitted for BPR. In both cell lines, non-specific binding refers to the off-target binding that occurs despite prior blocking of receptors with excess unlabeled LLP2A (PEG₄-LLP2A). Radioligand concentrations were evaluated in triplicate.

2.3.4 Internalization of ^{64}Cu -LLP2A in BPR and BPR α Cells

We next sought to compare the extent of ^{64}Cu -LLP2A internalization in BPR and BPR α cells relative to VLA-4⁺ B16F10 melanoma cells, as LLP2A internalization in B16F10 has previously been demonstrated [77]. The presence of cell surface VLA-4 is likely required for appreciable tracer uptake as internalization significantly increased ($p < 0.05$ - $p < 0.0001$) relative to baseline only for BPR α and B16F10 (Figure 20A). Furthermore, blocking VLA-4 with excess unlabeled LLP2A prior to introducing ^{64}Cu -LLP2A prevented binding of the radiolabeled agent (Figures 20B, C). The tracer was readily internalized by BPR α and B16F10 within 15 min ($10 \pm$

1.3 fmol/mg and 9.2 ± 1.4 fmol/mg, respectively), increasing to a peak value at 2h of incubation for both cell lines. Beyond this point, uptake plateaued in both cell lines (no statistical difference in B16F10 2h vs. 4h). Greater tracer accumulation occurs in BPR α , which became statistically significant relative to B16F10 at 4h ($p=0.008$). Only internalized tracer was considered, as a control condition without the stripping of surface-bound material (wells received PBS) displayed greatly increased activity for BPR α and B16F10 but not BPR (Appendix A).

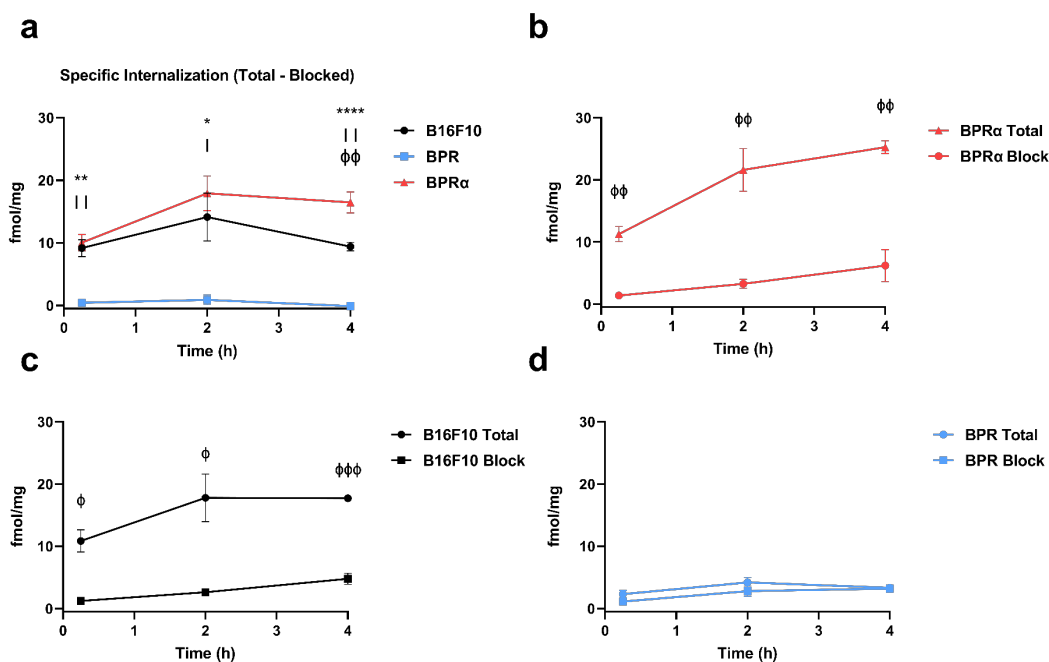


Figure 20 VLA-4 expression is required for ^{64}Cu -LLP2A internalization. (a) Time-dependent specific uptake (unblocked minus blocked internalization) of ^{64}Cu -LLP2A in B16F10, BPR, and BPR α cells. BPR α vs. BPR: *: $p < 0.05$, **: $p < 0.01$, ***: $p < 0.001$. B16F10 vs. BPR: I: $p < 0.05$, I I: $p < 0.01$. Total binding and blocking of ^{64}Cu -LLP2A in (b) BPR α , (c) B16F10, and (d) BPR cells. $n=3$ per time point. ϕ : $p < 0.05$, $\phi\phi$: $p < 0.01$, $\phi\phi\phi$: $p < 0.001$, by unpaired t-test.

2.3.5 Biodistribution of ^{64}Cu -LLP2A in BPR and BPR α Tumor Models

The biodistribution of ^{64}Cu -LLP2A was determined in BPR and BPR α tumor-bearing mice at 24h post-injection of the tracer (Figure 21, Appendix A). There was notable uptake of the

tracer in each tumor type, with significantly increased uptake in BPR α vs. BPR tumors (BPR: $1.7 \pm 0.2\%$ IA/g and BPR α : $2.8 \pm 0.2\%$ IA/g, $p < 0.0001$). As we have previously observed over both shorter (up to 4h) [77] and longer (up to 96h) [42] timescales in B16F10 melanoma, LLP2A accumulates in organs enriched in VLA-4 given its role in lymphocyte maturation, leukocyte homeostasis, and/or hematopoiesis - namely the thymus (BPR: $3.5 \pm 0.9\%$ IA/g and BPR α : $4.2 \pm 4.0\%$ IA/g), spleen (BPR: $8.1 \pm 4.4\%$ IA/g and BPR α : $6.0 \pm 1.9\%$ IA/g), and bone marrow (BPR: $2.2 \pm 0.4\%$ IA/g and BPR α : $1.6 \pm 0.5\%$ IA/g). Apart from the tumor, there was no significant difference in LLP2A uptake per organ examined in the BPR and BPR α models.

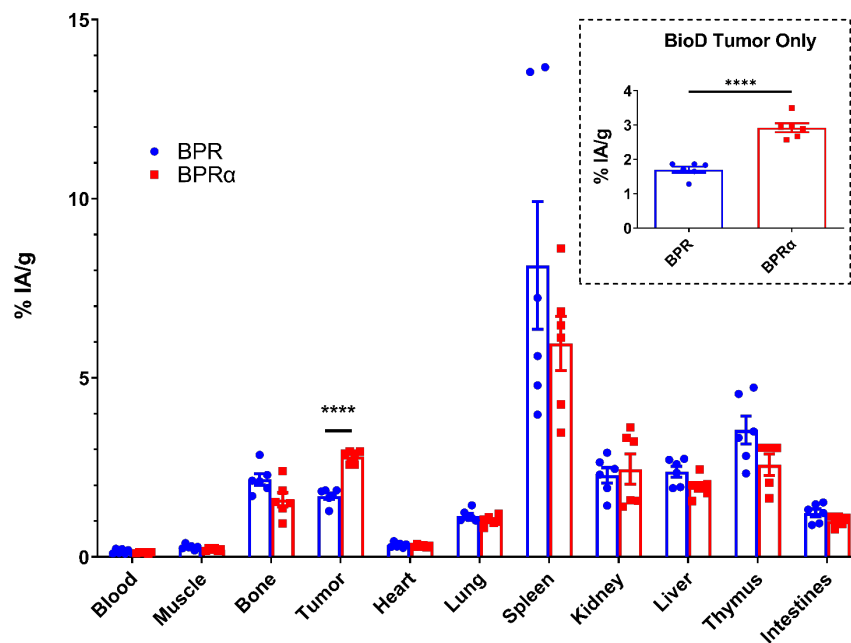


Figure 21 Biodistribution of ⁶⁴Cu-LLP2A in mice bearing BPR and BPR α tumors at 24h post-injection (n=6). **Inset:** comparison of tumor uptake only. Data are presented as % injected activity per gram of tissue. **** $p < 0.0001$ by unpaired t-test.

2.3.6 PET/CT Imaging of BPR and BPR α Tumor Models

At 4h post-injection of ^{64}Cu -LLP2A, there was a significant increase ($p=0.0021$) in tumor uptake in BPR α relative to BPR (Figure 22A, B), which likely reflects the addition of VLA-4 $^+$ tumor cells to the VLA-4 $^+$ immune cell component infiltrating the baseline tumor microenvironment. In both models, we observed marked uptake in the thymus, spleen, and bone marrow, in accordance with the biodistribution results. Notable activity was also seen in the bladder, indicating rapid renal clearance of the tracer. These observations parallel our previous studies using LLP2A in B16F10 melanoma [42, 77]. Unlike BPR tumors, BPR α tumor uptake remained detectable at 24h. The tumor-to-muscle ratio of BPR α was significantly greater than BPR at 4h ($p=0.0005$) but not at 24h ($p=0.2715$).

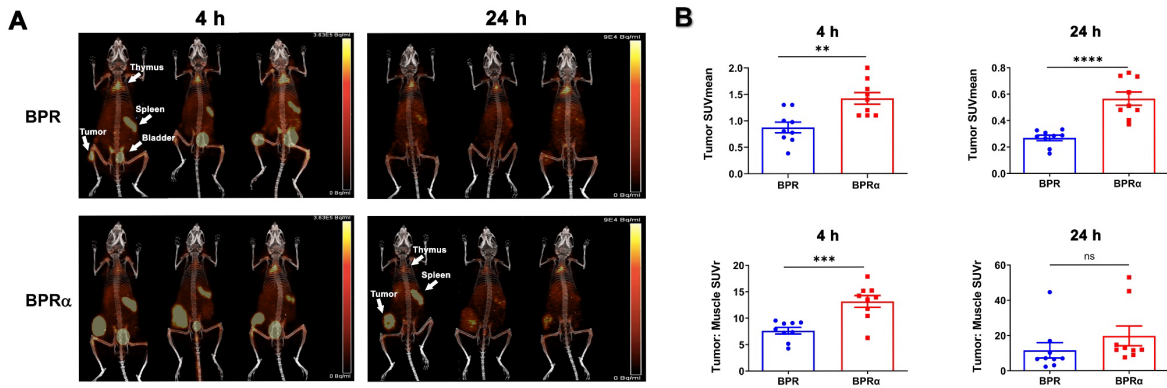


Figure 22 Representative ^{64}Cu -LLP2A PET images and image quantification in subcutaneous BPR and BPR α tumor models. (A) ^{64}Cu -LLP2A PET/CT images at 4h (left) and 24h (right) and (B) Tumor mean standard uptake values (SUV) and tumor-to-muscle (gastrocnemius of uninvolved leg) SUV ratios of BPR and BPR α tumor-bearing mice at 4h and 24h post-injection ($n=9$). ** $p<0.01$, *** $p<0.001$, **** $p<0.0001$ by unpaired t-test.

2.4 Discussion

Although immune checkpoint inhibitors and targeted therapy (BRAFi, MEKi) are potent additions to the therapeutic arsenal against metastatic melanoma, not all patients benefit, and the development of treatment resistance is common. As such, new therapeutic targets must be explored. Expression of VLA-4 (integrin $\alpha_4\beta_1$), an adhesion molecule that facilitates circulating tumor cell extravasation among other tumor-potentiating functions, is correlated to the development of metastatic disease in patients. Further, upregulated VLA-4 expression in melanoma often portends a more aggressive, metastatic phenotype [74]. As early-stage melanoma is generally well-managed by surgical resection [75], the capability to selectively image and stage disease progression via biomarkers such as VLA-4 may improve treatment outcomes. We have previously demonstrated that ^{64}Cu -TE1A1P-PEG₄-LLP2A (^{64}Cu -LLP2A) is readily taken up in VLA-4⁺ BRAF^{wt} B16F10 melanomas *in vivo*, providing good image contrast [77]. However, to our knowledge LLP2A has not been evaluated in a melanoma model that recapitulates aspects of aggressive patient tumors - namely high VLA-4 expression [74] and the presence of common underlying oncogenic driver mutations that are characteristic of human disease.

Here, we generated and investigated a novel matched pair of drug-resistant BRAF-mutant, PTEN-null cell lines (VLA-4⁻ and VLA-4⁺) for their differential targeting by LLP2A towards establishing their wider use in translational melanoma research. BRAF^{V600E} BP cells with acquired resistance to dabrafenib (BPR) were successfully transduced with the α_4 subunit of VLA-4 (BPR α). This was verified directly by specific antibody staining (Figure 16) and was also suggested by the substantially increased binding of the Cy3-LLP2A probe to BPR α vs. BPR cells (Figure 17). Despite the purported selectivity of LLP2A to intact VLA-4 [41] (BPR cells only

express the β_1 subunit paired to other integrins), there remains a detectable degree of staining to BPR cells. This is likely nonspecific, as a relatively high degree of interaction between Cy3 dye and lipid bilayers has been reported [187]. Although LLP2A fails to bind to other heterodimeric integrins containing the β_1 subunit (ex. $\alpha_2\beta_1$) or to $\alpha_4\beta_1$ with anti- α_4 blocking [41], to our knowledge LLP2A binding to β_1 alone has never been observed.

Saturation binding and internalization assays were performed with ^{64}Cu -LLP2A for both the BPR and BPR α cell lines. As expected, LLP2A displays high binding affinity to BPR α cells (K_d : 1.4 ± 0.45 nM), but its binding to BPR cells is not distinguishable from control (blocked) conditions. Similarly, the number of receptor sites bound by LLP2A was indeterminate in BPR cells - values can be calculated via the least squares method for one-site binding, but the model is very poorly fitted. The binding affinity of ^{64}Cu -LLP2A in BPR α is comparable (1.4 ± 0.45 vs 0.28 ± 0.03 nM) and the B_{max} roughly half (145 ± 8.8 fmol/mg vs 300 ± 4.5 fmol/mg) that of what we have previously reported for B16F10 melanoma cells [77]. These results are somewhat surprising given the significantly greater tracer internalization in BPR α vs. B16F10 after 4h (Figure 20). We hypothesize that these observations may be due to reduced tracer efflux from BPR α . BPR α displays a similar uptake pattern to B16F10, with internalization reaching a peak at 2h, followed by a plateau. Total and specific uptake in BPR are indistinguishable. Blocking of BPR α and B16F10 with excess LLP2A-PEG₄ renders internalization negligible, mirroring total BPR uptake. Taken together, these data indicate that internalization requires VLA-4 and that the low level of LLP2A binding to BPR seen in flow cytometry does not lead to significant uptake.

The biodistribution results show a strong increase in tumor LLP2A accumulation in BPR α vs. BPR tumors *in vivo* ($p < 0.0001$), with notably lower uptake in BPR α for organs enriched in VLA-4 (spleen, thymus, bone marrow) at 24h, although none of these comparisons reached

statistical significance. Similar observations emerged in a separate study interrogating tracer biodistribution in BPR α tumor mice conducted at 4, 24, and 48h post-injection, with time-dependent clearance (Appendix A). Notably, kidney activity appears to increase over time, though the extent of this is inflated by an extreme value at 48h. This observation underscores the importance of individual patient dosimetry for the clinical use of LLP2A in radionuclide therapy.

PET/CT demonstrates greater ^{64}Cu -LLP2A uptake and retention in BPR α tumors relative to BPR tumors, despite considerable clearance by 24h. Image quantification analysis corroborates the PET/CT observations, with higher tumor SUV and tumor-to-muscle SUV ratios in BPR α versus BPR at both time points. These differences are statistically significant except for the tumor-to-muscle SUV at 24h, when most of the tracer has cleared. Compared to the dynamics we previously determined for B16F10, BPR α demonstrates reduced tracer uptake by tumor: muscle SUV ratio at 4h, with uptake increasing to be nearly equivalent by 24h (Appendix A).

B16F10 has been a conventional model in cancer research since the 1970s due to its aggressiveness and tendency to spontaneously metastasize to the lungs [188]. However, B16F10 does not express the common oncogenic driver mutations/genetic deletions found in human melanomas. BP, the parent cell line to BPR and BPR α , was isolated from an immunocompetent BRAF $^{\text{V600E}}$ PTEN $^{-/-}$ genetically-engineered mouse model after induction with tamoxifen [183]. These lines, which more accurately simulate developing melanomas in humans [189], can be transplanted onto MHC-matched immunocompetent mice, allowing for the testing of interventional treatment protocols for future translation into the clinic.

2-deoxy-2-[^{18}F]fluoro-D-glucose (^{18}F -FDG) PET/CT is widely utilized clinically for metastatic melanoma detection, staging, and evaluation of response to treatment [190, 191]. However, ^{18}F -FDG PET/CT is often unable to detect subclinical lesions less than 1 cm in diameter

[192] that appear in preferential metastatic sites (brain, lungs, liver) due to non-disease background [193, 194]. We have previously demonstrated that ^{64}Cu -LLP2A can effectively delineate B16F10 lung metastases with high contrast [77]. Further, as ^{18}F -FDG signal reflects glucose metabolism, which is elevated in inflamed tissue and increases with immunotherapy, ^{18}F -FDG may not resolve tumor from regions of immune infiltration [195]. Numerous small molecules (ex. benzamide derivatives [196-198]), antibodies (ex. anti-GD2 [199, 200]), and peptides that circumvent these issues have been generated to image metastatic melanoma, and these typically bind overexpressed surface antigens (ex. MC1R) or melanin [201]. Intriguingly, VLA-4 has been shown to prompt extravasation of circulating tumor cells only when in the activated state [202]. As such, LLP2A may be especially well-suited to indicate the aggressiveness of melanomas, which is not possible with currently employed tracers.

A limitation of the study is that transduction of the α_4 subunit to increase VLA-4 may not recapitulate the VLA-4 cell surface copy number/density observed in clinical melanoma specimens. In this regard, a genetic model of drug-resistant BRAF^{V600E} VLA-4⁺ melanoma would be ideal; however, these are not available for use. BPR α graft models can serve as faithful approximations of human disease by their genetic and cell surface protein expression profile. Although we would predict that BPR α cells would have greater metastatic potential versus BPR cells *in vivo*, this was not formally tested in the current report but is planned for future studies.

3.0 Specific Aim 2: Compare therapeutic efficacy of ^{67}Cu -LLP2A TRT + dual ICI at two TRT dose levels informed from ^{64}Cu -LLP2A PET/CT imaging and evaluate TRT toxicity

3.1 Introduction

Central to the validation of any therapeutic is to first demonstrate efficacy and safety in preclinical models. In this context, it must be shown that TRT dosing can be predicted from corresponding PET/CT in a separate cohort, and not induce unnecessary toxicity. The absorbed dose distributions estimated from software must parallel the results of a biodistribution assay, in which actual TRT is given and organs of interest are harvested for radioactivity measurement. Should there be notable discrepancies, it is unlikely that the dosimetry software predictions are reliable. Subject-specific Monte Carlo dosimetry for theranostic pairs has been conducted in mice [98, 203, 204] and in patients [132, 205], although generally using the well-established $^{124/131}\text{I}$ PET/TRT pair. To our knowledge, subject-specific $^{64/67}\text{Cu}$ dosimetry with Monte Carlo simulation has not been reported. Instead, others have performed ^{67}Cu dosimetry directly from tissue samples and observed ^{64}Cu uptake following therapy [29] or have utilized OLINDA/EXM [206]. The latter was conducted as part of a first-in-human trial with $^{64/67}\text{Cu}$ -SARTATE (MeCOSar chelator-octreotate) in unresectable meningioma reported in late 2022. Both agents were well-tolerated and demonstrated overlapping tumor uptake by PET and SPECT (^{67}Cu emits photons suitable for SPECT), but imaging was not used to inform therapy doses. Here, we use Torch to perform fully Monte Carlo ^{67}Cu dose pharmacokinetic simulation from subject ^{64}Cu PET/CT images such that the tumor receives at least approximately 2.5 Gy. It has been previously demonstrated preclinically

for several immunogenically ‘cold’ tumor models that 2.5-5 Gy of tumor dose is sufficient for immunomodulation of the tumor microenvironment to enhance the efficacy of ICI [98]. In unpublished observations with the parent line BPR, anti-PD-L1 did not significantly delay tumor growth (data not shown). Anti-CTLA-4 has not been tested in either the BPR or BPR α model.

A seminal study by Twyman-Saint Victor and colleagues published in 2015 demonstrated in both mice and patients that EBRT + anti-CTLA-4 led to regression of both irradiated and unirradiated melanoma metastases [87]. EBRT was shown to expand the T cell repertoire in the TME, and anti-CTLA-4 polarized the T cell population to favor antitumor efficacy. However, resistance often occurred due to upregulation of PD-L1 on melanoma cells and accompanying T cell exhaustion, indicating a complementary role for anti-PD-L1, though not evaluated. Given the shortcomings of EBRT delivery and counterproductive immune suppression for metastatic disease, we previously conducted a therapy study in B16F10 for ^{177}Lu -LLP2A with single (anti-CTLA-4, anti-PD-1, or anti-PD-L1) or dual (anti-CTLA-4 with anti-PD-1 or anti-PD-L1) ICI [78]. TRT + dual ICI showed significant extension of median survival relative to either treatment alone, with slight benefit to TRT + anti-CTLA-4 + anti-PD-L1 compared to the combination with anti-PD-1. Further, in BRAF-mutant melanoma, PD-L1 overexpression is associated with acquired resistance to targeted therapy [207]. From the KEYNOTE-001 (NCT01295827) trial, patients scoring higher for PD-L1 expression demonstrated the highest objective response rate ($\approx 60\%$) and had the longest progression-free and overall survival when treated with anti-PD-L1 (pembrolizumab) [208]. For these reasons, anti-PD-L1 was paired with anti-CTLA-4 for the therapy study rather than anti-PD-1.

3.2 Materials and Methods

Procedures detailing the bounds for the contouring of PET/CT images and their import into the dosimetry software Torch are provided in Appendix B.

3.2.1 BPR α Tumor Model

All animal studies were conducted under an approved institutional animal care and use committee (IACUC) protocol at the University of Pittsburgh or the University of Missouri. Four- to six-week-old male and female C57BL/6 mice were obtained from the Jackson Laboratory (Bar Harbor, ME). For PET/CT imaging to inform dosimetry, BPR α tumors were inoculated by subcutaneous flank injection of 5×10^5 cells mixed with an equal volume of Matrigel (Corning Life Sciences, Tewksbury, MA). For the biodistribution assay and therapy study, 5- to 6- week-old mice were inoculated with 1×10^6 BPR α cells in saline. Tumor volume was approximated as $L \times W \times D$ from caliper measurement. Tumors were measured twice weekly and randomized for therapy at day 13 post-inoculation (average volume 18 mm^3), and TRT or saline was given on day 15. Mice were sacrificed if any of the following conditions were met: tumor diameter $\geq 15 \text{ mm}$ or ulceration, tumor burden large enough to restrict ambulatory movement, animal distress (hunched posture, lethargy, scruffy coat, 20% weight loss), or per veterinary recommendation.

3.2.2 PET/CT Imaging and Contouring of BPR α Tumors

TE1A1P-PEG₄-LLP2A (LLP2A) was radiolabeled with ^{64}Cu (^{64}Cu -LLP2A) at a specific activity of $1 \text{ mCi}/\mu\text{g}$ as in Aim 1. At the time of imaging, tumors were about 800 mm^3 mean

volume. Mice (2m/2f) bearing subcutaneous BPR α tumors received $\approx 330 \mu\text{Ci}$ (12.5 MBq; 57.2 MBq/nmol) ^{64}Cu -LLP2A intravenously through the lateral tail vein and static PET/CT images were acquired at 4 timepoints: 2, 4, 24, and 48h post-injection. At each timepoint, mice were anesthetized with 2% isoflurane, and small animal PET/CT images were acquired as static images collected over 10 min (2h, 4h) or 40 min (80 million coincidence events sought; 24h, 48h) with an Inveon PET/CT scanner (Siemens Medical Solutions, Knoxville, TN). PET and CT images were co-registered and PET images were reconstructed with an Ordered Subsets Expectation Maximizing 3D algorithm (OSEM-3D) with Inveon Research Workstation (IRW) software (Siemens Medical Solutions, Knoxville, TN). To define ROIs for dosimetry, contours were drawn manually per mouse at each timepoint from CT images or when necessary, from PET images in VivoQuant 2021 software (Invicro, Needham, MA) (Figure 23). To account for unique spill-in from neighboring organs, the left and right lungs and kidneys were drawn separately. The total body ROI for comparison to OLINDA was the full-body ROI from CT with the tumor, tail, and paws excluded.

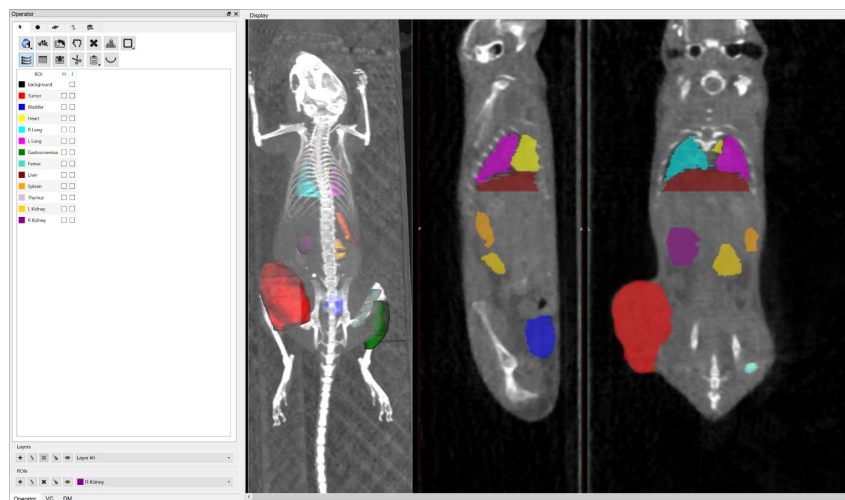


Figure 23 Screenshot of tumor and organ ROIs drawn in VivoQuant 2021, indicated by color.

3.2.3 Dosimetry Calculations

Monte Carlo subject-specific tumor and organ dosimetry for ^{67}Cu -LLP2A was evaluated with Torch v 1.1.0.122 (Voximetry Inc, Madison, WI). Longitudinal ^{64}Cu -LLP2A PET/CT imaging informed the time-dependent change in the estimated biodistribution of ^{67}Cu -LLP2A, accounting for the different decay rates of ^{64}Cu ($t_{1/2} = 12.7\text{h}$) and ^{67}Cu ($t_{1/2} = 2.6\text{d}$). The anatomical and activity distributions were delineated by CT and PET volumes for each mouse per timepoint, respectively. The ^{67}Cu -LLP2A pharmacokinetics within tumor and organ ROIs were quantified to determine absorbed doses within the bounds of the volumes imported from VivoQuant 2021. As activity integration in this iteration of Torch removes non-overlapping portions of corresponding ROIs across time, activity integration can substantially reduce ROI volume. Instead, a workaround for dose rate integration was devised (Appendix B). Mean ^{67}Cu -LLP2A absorbed dose in each ROI was calculated for a single timepoint with an end criterion of $\leq 2\%$ uncertainty. These values were normalized by the ^{67}Cu dose rate, integrated with a hybrid trapezoidal-exponential approach, and summed per mouse to determine the total absorbed dose in Microsoft Excel. The prescribed dose (in units of mGy/MBq) is the ROI absorbed dose per injected activity.

For corresponding values from OLINDA 2.2.3 (Hermes Medical Solutions, Stockholm, SE), tumors were modeled as water spheres, with absorbed dose coefficients scaled to those of built-in OLINDA tumor model sizes and averaged across timepoints. For all other ROIs, functions were fit to the measured data and integrated to determine time-integrated activity (TIA) in Matlab software (MathWorks, Natick, MA). The TIA was then used as input for the OLINDA 25g laboratory mouse phantom (MOBY). Administered activity was adjusted via a whole-body weight ratio to account for size differences between the mouse and mouse phantom, as detailed elsewhere [209].

3.2.4 Copper-67 Radiolabeling of TE1A1P-LLP2A

TE1A1P-LLP2A was added to $^{67}\text{CuCl}_2$ in 0.5M ammonium acetate pH 6.5 buffer for a specific activity of 350 $\mu\text{Ci}/\mu\text{g}$ (molar activity 542 $\mu\text{Ci}/\text{nmol}$) in all experiments. To avoid radiolysis, a minute amount of gentisic acid was added to the reaction, and the vial was incubated at 70°C for 30 min under shaking. Radiochemical purity was assessed by radio-HPLC.

3.2.5 ^{67}Cu -LLP2A Biodistribution

At day 19 post-tumor inoculation, mice bearing BPR α tumors (n=4; 2m/2f) received approximately 12 μCi (0.4 MBq) ^{67}Cu -LLP2A via the lateral tail vein and were euthanized at 4, 24, 48, and 72h post-injection. Blood, muscle (gastrocnemius of uninvolved leg), bone (femur of uninvolved leg), heart, spleen, kidneys, intestines, lungs, liver, stomach, thymus, and tumor were extracted, weighed, and the activity measured with a γ counter (Wallac Wizard 3" 1480, PerkinElmer, Waltham, MA). To assess the quality of the injections, the tail was isolated and activity counted.

3.2.6 Therapy Study Treatments and Timeline

^{67}Cu -TE1A1P-LLP2A (at 700 μCi or 1 mCi [25.9 or 37 MBq] per mouse) or saline was administered intravenously via the lateral tail vein on treatment 'day 0'. Armenian hamster anti-mouse CTLA-4 (IgG, clone UC10-4F10-11) and rat anti-mouse PD-L1 (IgG2b, clone 10F.9G2) were purchased from BioXCell (Lebanon, NH). Antibodies or their respective isotype controls

(BioXCell) were administered intraperitoneally (200 µg each) on days 3, 6, and 10. The study treatment groups and timeline are detailed in Figure 24.

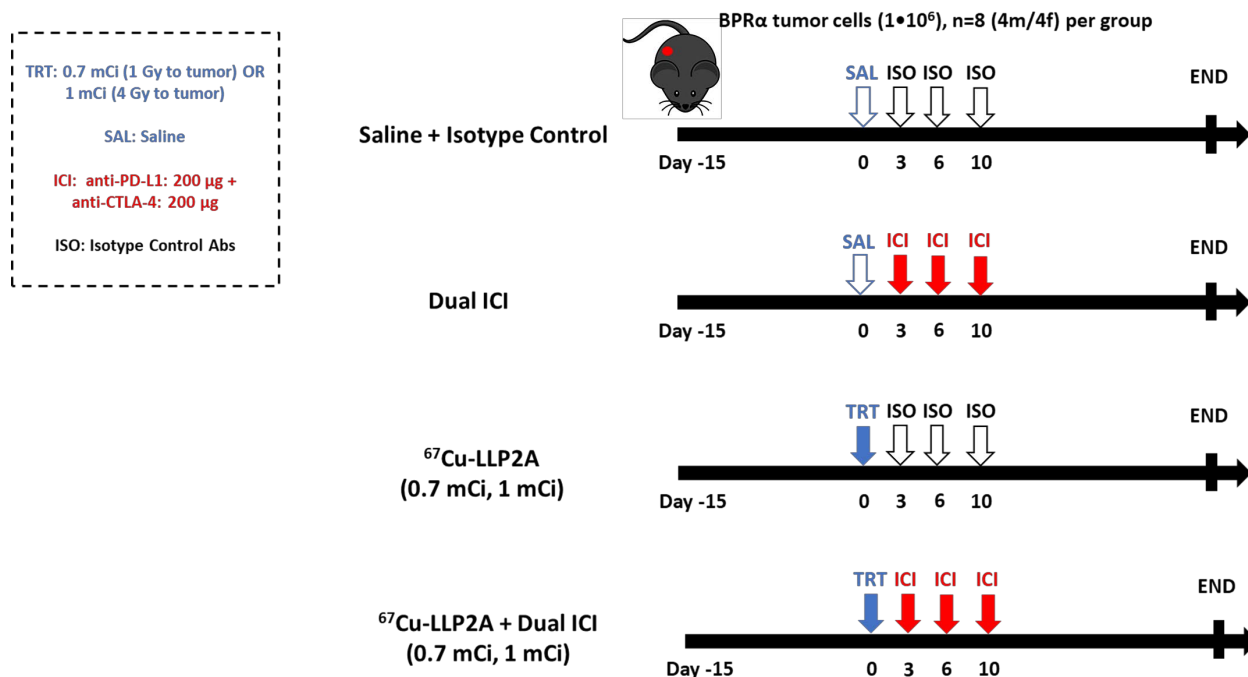


Figure 24 BPR α therapy study treatments and timeline. TRT: ^{67}Cu -LLP2A, ISO: isotype control, SAL: saline (vehicle control), ICI: dual anti-CTLA-4 + anti-PD-L1.

3.2.7 Toxicity Evaluation

Beginning the week following TRT and over the course of the therapy study, blood was drawn weekly by tail vein nick into EDTA-coated tubes for CBC analysis with a VetScan VS2 hematology analyzer (Abaxis, Union City, CA). Blood counts were compared to naïve mice (no tumor or treatment, n=7, 4m/3f). As each animal exited the study, the mice were sacrificed for a blood chemistry panel (Zoetis, Parsippany-Troy Hills, NJ).

3.2.8 Statistics

Prescribed dose estimates were compared amongst the ROIs with one-way ANOVA and Tukey's HSD for multiple comparisons. Survival was plotted with Kaplan-Meier curves, and overall differences between the survival curves and between group survival curves were assessed by the logrank test. Statistical analyses were performed with GraphPad Prism 9.4.

3.3 Results

3.3.1 ^{67}Cu -LLP2A Dosimetry and Biodistribution Studies

As we have previously demonstrated substantial and selective uptake of ^{64}Cu -LLP2A for PET imaging in the BRAF^{V600E} BPR α model [2], we next sought to leverage the imaging data to guide therapeutic dosing with the same-element β^- -emitter (^{67}Cu -LLP2A). To do so, we employed the Monte Carlo dosimetry calculation software Torch, which determines time-resolved dose distributions from subject-specific images and can predict absorbed doses with a corresponding therapy isotope by adjusting for differences in decay rate. Serial PET/CT was conducted to observe LLP2A uptake in the tumor and normal tissues at 2, 4, 24, and 48h following IV administration of ^{64}Cu -LLP2A. From maximum intensity projection PET/CT images, there was notable tumor uptake and retention, in addition to organs enriched in VLA-4 (thymus, bone marrow, spleen, Figure 25). Dosimetry calculations for ^{67}Cu -LLP2A (Figure 26A) demonstrated highly significant ($p < 0.0001$) tumor dose relative to non-lymphatic normal tissues, sparing the radiosensitive kidneys. Dose delivery to the tumor was also significantly increased versus non-target lymphatic

tissues (thymus: $p = 0.014$, spleen: $p = 0.018$), though to a lesser extent. The biodistribution study with ^{67}Cu -LLP2A (Figure 26B) demonstrates rapid accumulation mainly in spleen, tumor, and the femur (bone), followed by progressive washout in the tumor but washout that stabilizes after 24h in the other tissues. Interestingly, uptake in the spleen is dramatic after 4h ($23.2 \pm 2.7\%$ IA/g, mean \pm SEM), which shows a similar trend but greater magnitude relative to tumor uptake as with ^{64}Cu -LLP2A (Appendix B). Unlike what may be assumed from dosimetry, uptake in the thymus was low and increased only slightly over time. Bone uptake also appears to counter the dosimetry results. Encouragingly, kidney uptake was low. Values per tissue per timepoint are in Appendix B.

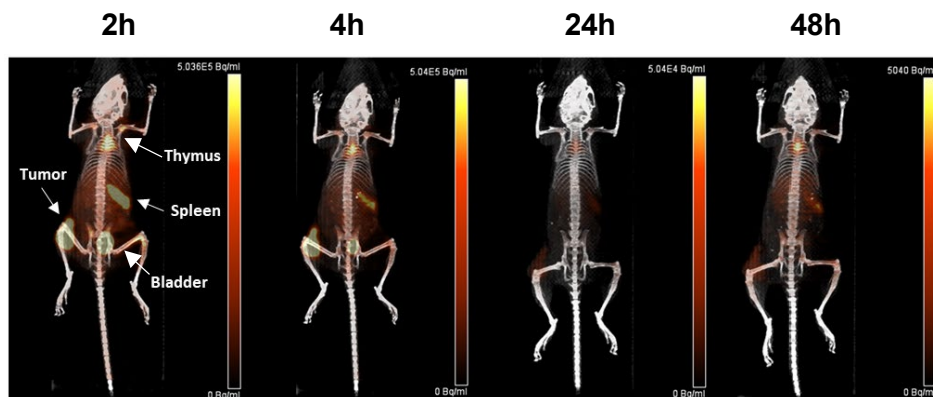


Figure 25 Representative timecourse of ^{64}Cu -LLP2A in BPR α tumor model. Shown are PET/CT maximum-intensity projections.

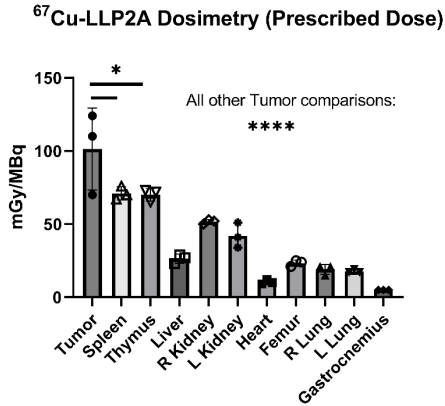
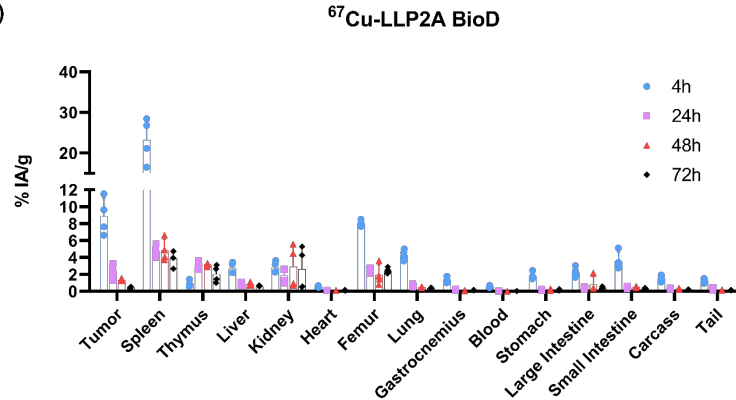
A.**B.**

Figure 26 Comparison of ⁶⁷Cu-LLP2A dosimetry and biodistribution results. (A) Prescribed dose (absorbed dose per injected activity) dosimetry for ⁶⁷Cu-LLP2A with subject-specific Monte Carlo simulation from serial ⁶⁴Cu-LLP2A PET/CT imaging (n=3). (B) Actual ⁶⁷Cu-LLP2A *ex vivo* biodistribution assay data acquired over time (n=4, 2m/2f). * p < 0.05, ** p < 0.001).**

3.3.2 Comparison of Subject-Specific and Phantom-Based ⁶⁷Cu-LLP2A Dosimetry

OLINDA is the predominant software platform used to assess radiation dose for nuclear medicine, both preclinically and clinically. However, it relies upon standardized phantoms to simulate organs and models tumors as spheres of uniform density. As such, OLINDA absorbed dose predictions may deviate substantially from those calculated with subject-specific methods [131, 210], particularly without mass scaling. To observe the extent of the difference between the two methods, ⁶⁷Cu-LLP2A dosimetry estimates to deliver a standard 2 Gy dose were compared for the tumor and other organs shared in the MOBY phantom. Table 2 provides prescribed doses using the OLINDA MOBY phantom or Torch necessary for 2 Gy dose delivery to the tumor in each mouse (M1, M3, M4). OLINDA values for the injected dose are consistently greater by a substantial margin, with a percent difference range of nearly 50% to nearly 75%. The ranking according to the tumor absorbed dose is the same in both platforms. This is likely due to mass scaling. Notably, M4, the smallest tumor, has a mass less than half that of the other two and

approximately twice the prescribed dose. This parallels earlier observations in a study utilizing a similar Monte Carlo software for ^{90}Y doses from ^{86}Y PET images with an alkylphosphocholine analog, in which larger tumors absorbed greater doses per injected activity [98]. We expect that this is due to the increased extent of the crossfire effect of β^- -emitters as more of the agent can bind in larger tumors.

Table 2 Prescribed activity for 2 Gy tumor dose for each mouse from OLINDA and Torch. Percent difference

$$= \frac{|AD_{OLINDA} - AD_{Torch}|}{\left(\frac{AD_{OLINDA} + AD_{Torch}}{2}\right)} \cdot 100.$$

Tumor	OLINDA Sphere 2 Gy Injected Activity (MBq)	Torch 2 Gy Injected Activity (MBq)	% Difference
M1	26.3	16.1	48.1
M3	31.9	18.2	54.7
M4	61.5	28.6	73.0

Even with mass scaling to account for organ weight differences between the test mice and mouse phantom, OLINDA mean dose predictions to the clearance organs (kidneys, spleen, liver, bladder) are vastly lower (Table 3). Both kidneys individually are expected to receive markedly more dose in Torch than as a composite in OLINDA. This is particularly important as the kidney dose is often dose-limiting, and OLINDA predictions could lead to excessive administered activity and severe toxicities. Due to motion artifacts, preclinical CT may not properly determine tissue densities with high accuracy [203]. For this reason, the agreement between OLINDA measurements for the lungs and the sum of the individual lungs in Torch is surprising. Further, the limited resolution of the preclinical PET imager results in unavoidable partial volume effects, which are intensified for smaller volumes. The most striking difference occurs for the bladder (88%). This is somewhat expected due to changes in volume with bladder refilling and voiding as well as scattering artifacts [211] that are reflected in Torch but not OLINDA. Although calculations in both the OLINDA

MOBY phantom and Torch are subject to partial volume effects, they may be more pronounced in Torch as it uses non-uniform activity distributions.

Table 3 Comparison of ROI prescribed mean doses \pm standard deviation (SD) for the OLINDA MOBY phantom and Torch.

Organ/ROI	OLINDA Mean (mGy/MBq) \pm SD	Torch Mean (mGy/MBq) \pm SD	% Difference in Mean
Kidneys	30.2 \pm 13.2	42.0 \pm 8.5 (L) 51.7 \pm 1.5 (R) 93.7 \pm 9.3 (Comb.)	32.8 (L) 52.6 (R) 102.5 (Comb.)
Spleen	42.5 \pm 15.7	71.0 \pm 4.6	50.3
Liver	19.1 \pm 4.0	26.3 \pm 3.1	31.7
Heart	14.3 \pm 2.5	10.3 \pm 1.5	32.3
Lungs	35.1 \pm 16.4	17.7 \pm 1.2 (L) 19.0 \pm 3.5 (R) 36.7 \pm 4.2 (Comb.)	65.9 (L) 59.5 (R) 4.5 (Comb.)
Bladder	86.1 \pm 49.1	222 \pm 70.1	88.2
Total Body (Tumor Excluded)	12.1 \pm 2.6	12.7 \pm 2.1	4.8

3.3.3 ^{67}Cu -LLP2A + Dual ICI Therapy in Subcutaneous BPR α Model

Torch dosimetry results for the tumor absorbed dose were utilized to stratify mice into two dose tiers for synergy with ICI as suggested from Patel et al. [98]. Male and female C57BL6 mice (n=8 per group, 4m/4f) bearing subcutaneous BPR α tumors were randomized to receive approximately 700 μCi (2.5 Gy to the tumor, 0.1 Gy/MBq injected, 25 MBq \approx 675 μCi) or about 1 mCi ^{67}Cu -LLP2A (4 Gy to tumor, 40 MBq \approx 1081 μCi) alone or in combination with dual ICI. No treatment resulted in tumor regression, yet 1 mCi ^{67}Cu -LLP2A + dual ICI best slowed tumor progression (Figure 27A, H). However, saline (vehicle control) also paradoxically appears to slow tumor growth more substantially than all other remaining treatments, undermining conclusions about which is best. This is most likely an experimental artifact, and future studies will be

conducted to confirm. In several groups, one or more mice did not demonstrate appreciable tumor growth after treatment administration and were removed from analysis. Notably, all four of these mice were male. Sex-based differences in treatment response are explored in a following section. No significant difference in survival exists amongst the groups ($p = 0.333$; Figure 27B, Figure 28A).

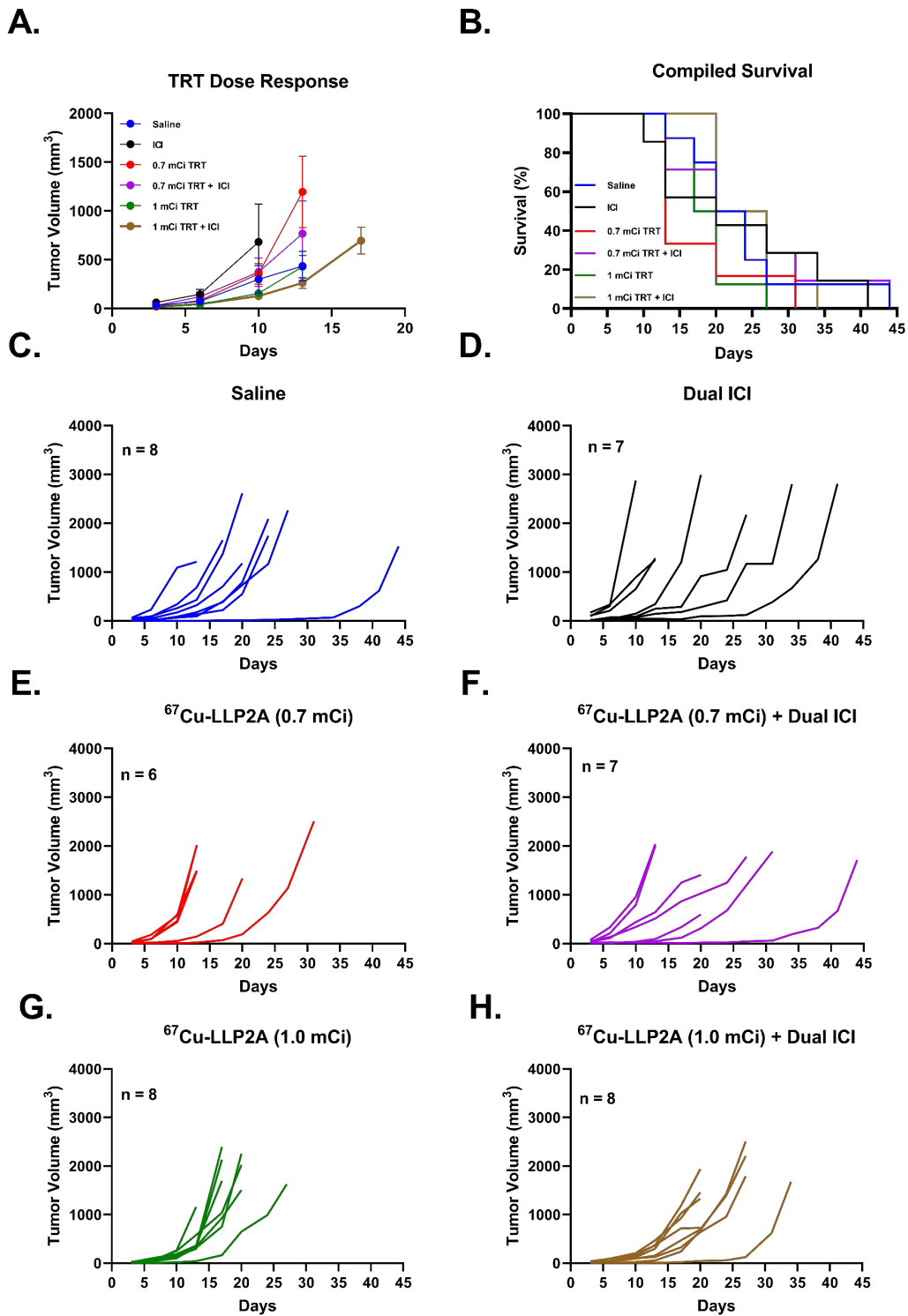


Figure 27 Compiled and individual tumor growth curves (A, C-H) as well as survival (B) for all treatment groups. Days refer to days post-injection of TRT or vehicle control (saline). Data shown in A as mean \pm SEM.

To better interrogate differences amongst the group survival curves as well as any potential benefit of adding dual ICI to TRT, per group median survival and relevant group survival curves were compared (Figure 28). There are no notable differences between the survival curves for saline and dual ICI ($p = 0.787$, Figure 28B) or for dual ICI versus either TRT dose + dual ICI (0.7 mCi + ICI $p = 0.689$, 1 mCi + TRT + ICI $p = 0.979$; C, D). However, the curve for dual ICI added to 1 mCi TRT is significantly different than that for 1 mCi TRT alone ($p = 0.025$), whereas this is not true of 0.7 mCi TRT ± ICI ($p = 0.262$; E, F). In short, 1 mCi TRT ± ICI is the only treatment group to show benefit relative to dual ICI, though modest, and indicates the sought improvement of adding dual ICI to TRT.

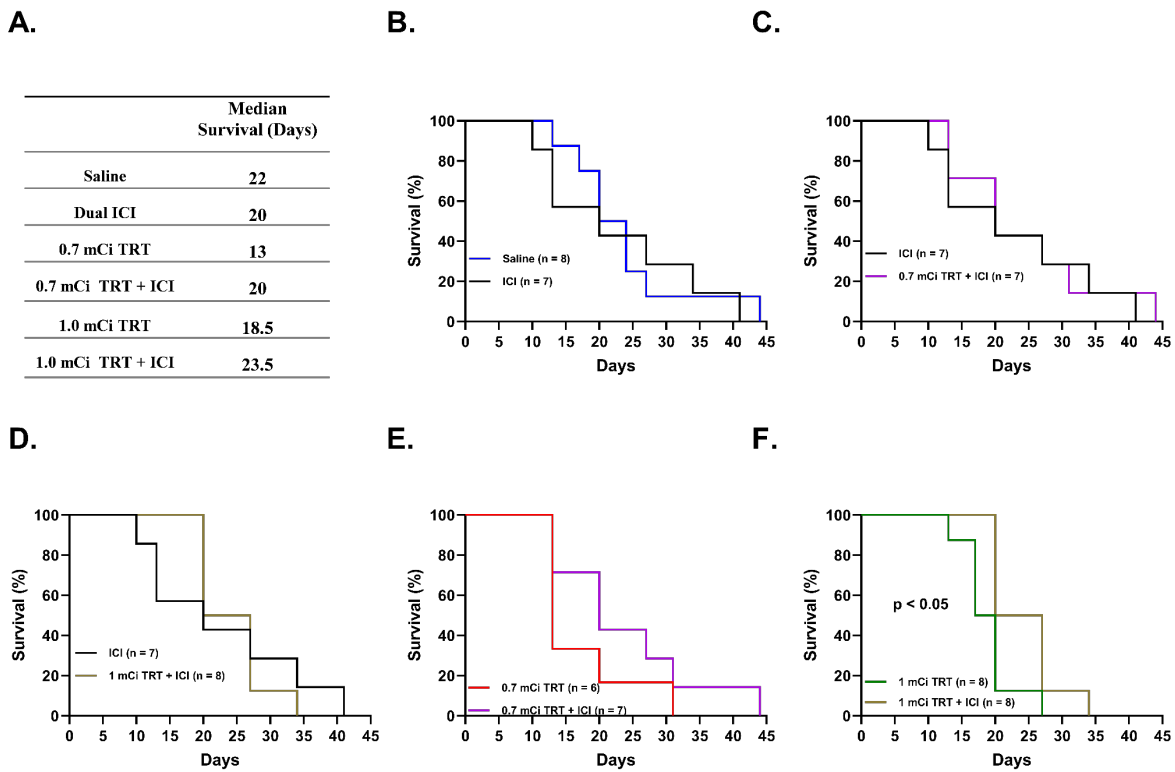


Figure 28 Median survival (A) and relevant survival curve pairings (B-F) for treatment groups. Significance determined by logrank test.

3.3.4 Sex Differences in Response to ^{67}Cu -LLP2A TRT + ICI Treatments

By color-coding the individual mouse tumor growth curves by sex (Figure 29) and grouping survival by sex (Figure 30), an intriguing improvement prognosis for male mice is evident in all TRT \pm ICI groups apart from the 0.7 mCi TRT group (Figures 29C, 30C). Here, two of the four males did not grow tumors, so these trends may hold at this dose as well upon repetition. From the male versus female survival plots, males in all groups except 0.7 mCi TRT are more resilient. Curiously, statistical differences between male and female survival curves only occur for TRT + ICI groups (0.7 mCi + TRT: $p = 0.019$, 1 mCi + TRT: 0.008; Figure 30D, F), with an increased magnitude of the effect for the higher TRT dose. The reason for these observations is unknown but will be investigated in future work.

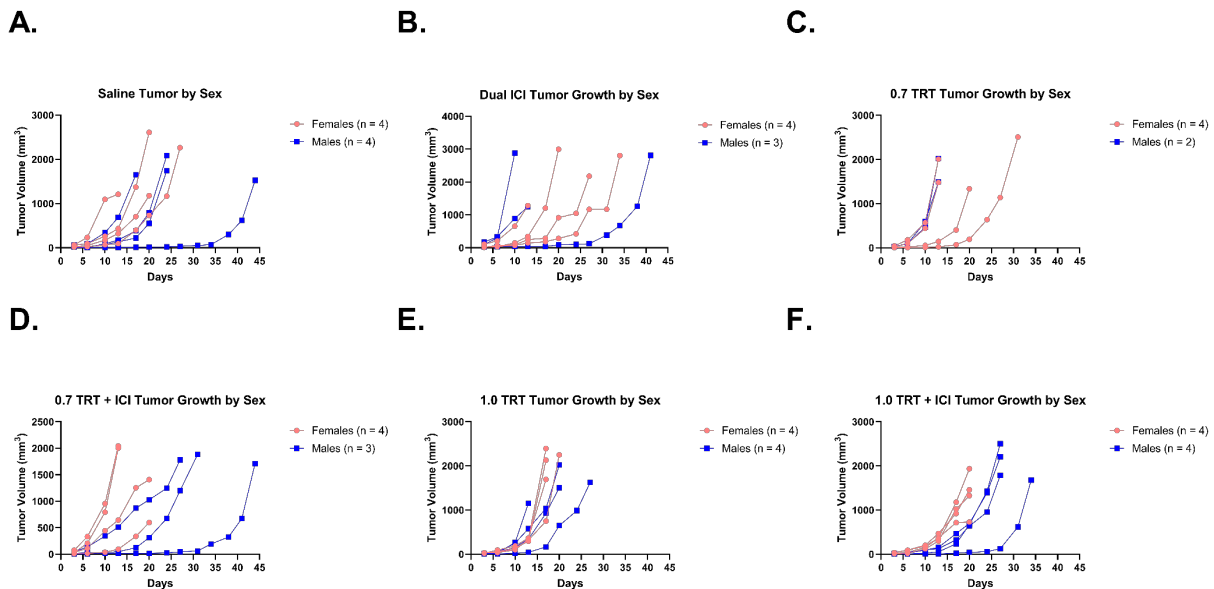


Figure 29 Tumor growth curves from the ^{67}Cu -LLP2A TRT + ICI therapy study color-coded by mouse sex. Each data point represents when a tumor volume measurement was taken.

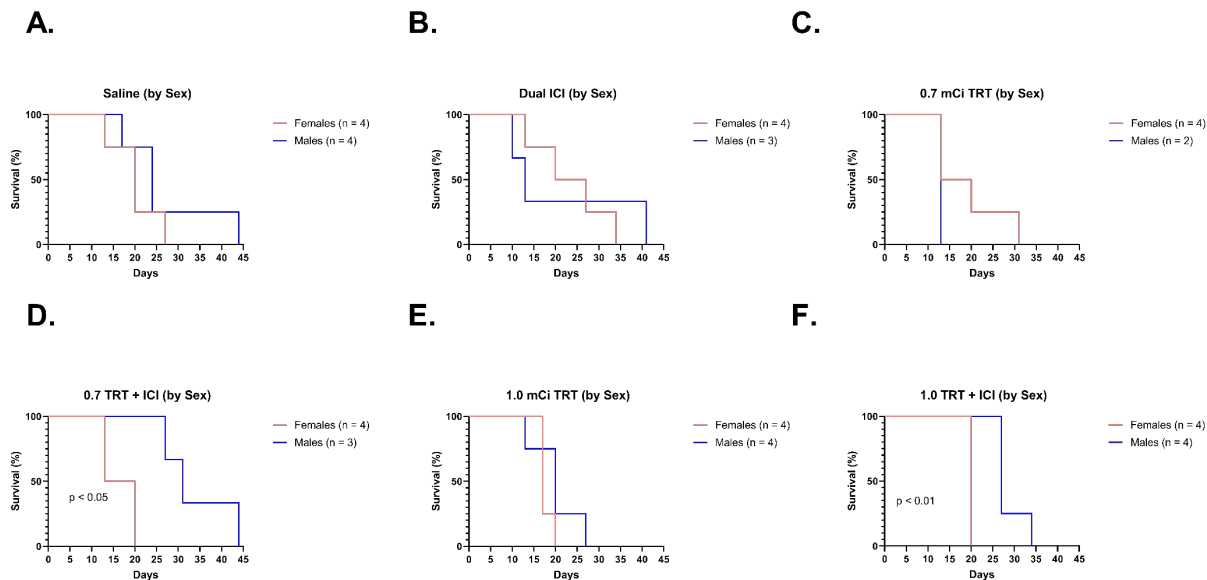


Figure 30 Survival curves per treatment group plotted according to sex. Significance was determined with the logrank test.

3.3.5 Toxicity of ⁶⁷Cu-LLP2A + Dual ICI Treatments

Key to the synergy of TRT with ICI is that the former does not induce significant bone marrow suppression or lymphopenia due to radiation that would hinder antitumor immunity. As part of the therapy study, complete blood count was performed for all mice prior to TRT and then weekly from half the mice per group (aiming for n=4), alternating the mice each time. Data shown in Figure 31 tracks particular blood metrics through 11 d post-injection – beyond this point, sample size decreased too greatly to be statistically viable in the 1.0 mCi TRT group (n=1 at day 18). Although moderate decreases in all blood metrics occurred shortly after TRT, this was followed by an expected rebound at day 11. There were no statistical differences compared to saline in leukocyte (WBC) or lymphocyte (LYM) count for any treatment at any timepoint, suggesting that TRT does not induce lymphopenia. Anemia and bone marrow suppression were avoided as there

were no observed differences in red blood cell (RBC) count, hemoglobin (HGB), platelets (PLT), or body weight. All groups were compared to blood controls, which are untreated naïve mice of the same strain and age. These were included for reference. Surprisingly, there is substantial variation in the CBC metrics of the blood controls with time, which may point to an issue with analyzer calibration.

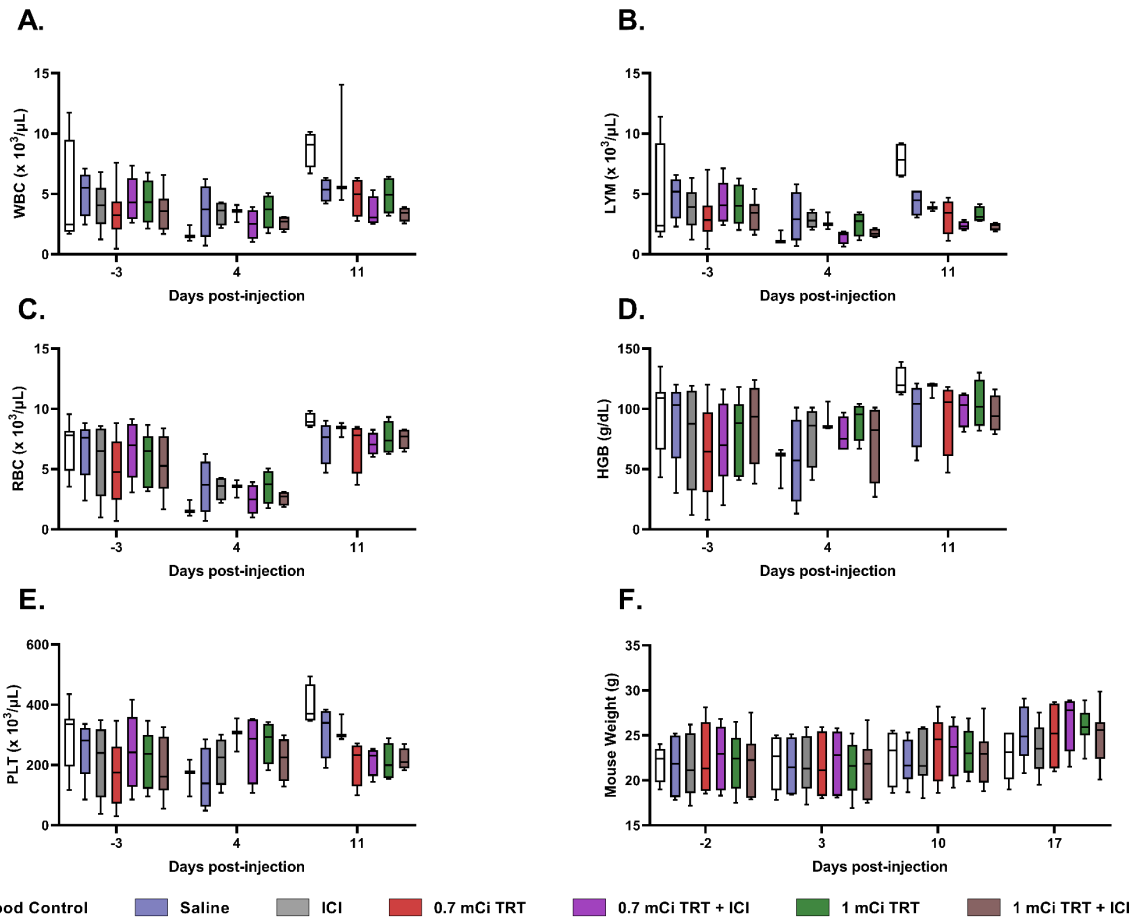


Figure 31 Metrics of hematological toxicity in therapy study mice. Complete blood count was performed weekly prior to and for the first several weeks following TRT administration. (A-E) Leukocytes (WBC) and lymphocytes (LYM), red blood cells (RBC), hemoglobin (HGB), and platelets (PLT) were tracked. (F) Mouse weight was also measured. For all treatments, n = 8 at day -3, n = 3-4 for all later timepoints.

3.4 Discussion

The central aim of the studies within this chapter was to leverage subject-specific tumor lesional dosimetry towards optimized therapeutic efficacy with the combination of corresponding TRT and dual ICI. To our knowledge, this marks the first such trial with the $^{64/67}\text{Cu}$ theranostic pair and in a model that more closely simulates clinical melanoma than the standard B16F10. BPR α is targeted therapy-resistant (dabrafenib) and overexpresses VLA-4 similarly to more aggressive/metastatic melanomas [74]. ICI has not previously been tested in BPR α , but the parent line BPR has been observed by the Storkus Lab to resist anti-PD-L1 alone and in combination with STING agonists (data not shown). Here, longitudinal ^{64}Cu -LLP2A PET/CT imaging in the BPR α model was used to quantify a prescribed dose (tumor absorbed dose per injected activity) of ^{67}Cu -LLP2A by Monte Carlo simulation of ^{64}Cu -LLP2A pharmacokinetics with corrections for the decay rate and emission profile of ^{67}Cu . To determine whether this dosimetry process could select efficacious therapy dosing for combination with ICI, two tumor absorbed doses within the range specified for synergy with ICI in cold tumors [98] were chosen. TRT was given with and without dual ICI (anti-PD-L1 + anti-CTLA-4), as this is the current clinical standard of care and targeted therapy resistance is associated with PD-L1 upregulation [207].

From Monte Carlo dosimetry (Figure 26A), the prescribed dose (absorbed dose per injected activity) was greatest for the tumor of all ROIs and was significantly increased relative to lymphatic organs enriched in VLA-4 (thymus, spleen; $p < 0.01$) and highly significantly increased relative to the VLA-4-dense bone marrow (femur; $p < 0.0001$). Importantly, tumor prescribed dose was nearly double and highly significantly increased ($p < 0.0001$) relative to either of the kidneys, which are often dose-limiting. Comparing the subject-specific tumor results from Torch to the unit density spheres of the widely used OLINDA software, the latter suggested substantially increased

injected activity. Similarly, mean doses to all shared ROIs except the liver, lungs, and heart were substantially greater in Torch versus the standardized OLINDA phantom (differences of 32.8-88.2%). As such, OLINDA predictions would likely lead to excessive administered activity and toxicities. The ^{67}Cu -LLP2A biodistribution assay (Figure 26B) largely replicated the trends of the merged ^{64}Cu -LLP2A biodistribution – namely greater accumulation in the spleen (23.2 ± 2.7 % IA/g at 4h) versus the tumor (8.9 ± 1.1 % IA/g at 4h) as well as markedly longer retention (comparison in Appendix B). Further, there was decreased thymic uptake and increased bone (femur) uptake compared to what might be predicted from the Torch dosimetry. Deviations between the dosimetry and actual ^{67}Cu -LLP2A biodistribution results may be due in part to the use of much larger tumors (mean volume 800 mm^3) for the imaging than those used for the biodistribution (mean volume $\leq 50 \text{ mm}^3$). Our tumor dosimetry results and those previously published [98] show that larger tumors absorb a greater fraction of the absorbed dose.

The results of the therapy study are mixed. On the one hand, the highest TRT dose sufficient for a tumor absorbed dose of 4 Gy (1 mCi TRT + ICI) best impedes tumor growth, and the addition of ICI shows survival benefit to TRT alone, but no treatment option led to tumor regression (Figures 27, 28). More worrisome is the seeming effectiveness of the saline (vehicle) control. This experiment will ultimately be repeated for the saline group to test the veracity of this observation. Intriguingly, males demonstrate greater benefit from treatment, and notably their survival curves are significantly different than those of females for both TRT + ICI doses, with greater effect at 1 mCi (Figures 29, 30). This is likely a byproduct of the tumor model and will be investigated further. No significant changes in CBC metrics (leukocytes, lymphocytes, red blood cells, hemoglobin, and platelets) or body weight loss occurred within the measurement timeframe, suggesting that no treatment results in lymphopenia or bone marrow suppression that manifests as

anemia (Figure 31). However, the variability seen with the blood controls calls into question the reliability of these results somewhat. If repeated, repeatability of measurements for naïve mice CBC will first be ensured for the analyzer.

The disappointing performance of TRT + ICI versus ICI alone may be due to counterproductive T cell depletion because of TRT. We have previously shown in tuberculosis granulomas that LLP2A avidity is greatest for T cells and macrophages of the major immune cell classes [185]. It may also be the case that the BPR and BPR α lines are resistant to this *in situ* vaccination approach due to limited tumor neoantigen recognition by endogenous T cells and/or MHC I loss on tumor cells. A recent thorough meta-analysis of transcriptomic data in mouse and human melanoma for subjects progressing on single or combined targeted therapy found that TIL frequency is reduced upon acquiring drug resistance, and that TIL loss is preceded by the downregulation of MHC I [212]. A major limitation of the work in this chapter is the lack of TME characterization over the course of therapy; this has not yet been systematically studied in these models. This is outside the scope of this dissertation but is planned for future studies.

4.0 Summary and Future Directions

4.1 Overall Summary

The overarching goal of this dissertation was to utilize PET/CT imaging of a targeting agent to rationally select dosing for the same agent labeled with the cognate (same element) therapeutic radioisotope. To maximize therapeutic effect, we added immune checkpoint blockade to this targeted radiopharmaceutical therapy approach, which is gaining increasing traction clinically. We employed the peptidomimetic tracer LLP2A, which binds selectively to a target overexpressed in both hematopoietic and solid tumors. We and others have validated LLP2A extensively in preclinical tumor models, and it has recently been studied for imaging of multiple myeloma in patients. Building off our previous observations involving LLP2A PET/CT in murine melanoma, we used two novel spontaneous melanoma cell lines that are drug-resistant and more closely reproduce features of clinical melanoma than those in traditional use. One was derived from the other but transduced to overexpress the target of LLP2A (it does not natively express the intact target) and therefore simulate a more aggressive melanoma phenotype. The two lines were compared via *in vitro* characterization and *in vivo* PET/CT imaging for their ability to bind and internalize LLP2A. As expected, target expression was required for LLP2A binding and uptake. From longitudinal PET/CT images of mice bearing subcutaneous target-expressing tumors, subject-specific dosimetry was conducted with dedicated software to estimate the absorbed dose per unit activity injected (‘prescribed dose’) to the tumor and organs-of-interest for LLP2A labeled with the cognate therapy isotope. The prescribed dose metric was used to suggest two dose tiers for LLP2A targeted radiotherapy to be paired to immune checkpoint in this same tumor model.

First, we sought to validate LLP2A both *in vitro* and for PET imaging in translational models of BRAF-mutant melanoma that differed in the extent of target expression. We observed that ^{64}Cu -LLP2A demonstrated high binding affinity to the target-overexpressing line (BPR α , $K_d = 1.4$ nM) but indefinite binding to the parental line lacking the intact target, the integrin VLA-4 (BPR). BPR α internalization of LLP2A and its kinetics paralleled that of the traditional VLA-4 $^+$ murine melanoma line B16F10. Appreciable uptake occurred rapidly (by 15 min) in both, reaching a zenith at 2h, followed by a plateau. At 4h, BPR α internalization was significantly greater than that of B16F10 ($p < 0.01$), perhaps due to greater efflux in the latter. Despite some binding to BPR occurring with LLP2A labeled for flow cytometry, internalization was undetectable from the radioassay. From PET/CT, ^{64}Cu -LLP2A exhibited significantly increased uptake in BPR α versus BPR tumors at both 4 ($p < 0.01$) and 24h ($p < 0.0001$) post-injection, with improved retention. An *ex vivo* biodistribution performed immediately following PET/CT imaging at 24h corroborated this finding and indicated reduced LLP2A accumulation in lymphoid organs (spleen, bone marrow, thymus) compared to BPR, although no comparisons reached statistical significance. Lastly, we combined these biodistribution data with previously acquired biodistribution assays performed at 4 and 48h post-injection in BPR α . We noted time-dependent clearance in all organs apart from the kidneys, where several inflated values at 48h give the impression of retention, emphasizing the need for individualized dosimetry for therapeutic use of LLP2A. In short, ^{64}Cu -LLP2A discriminated BPR α (VLA-4 $^+$) versus BPR (VLA-4 $^-$) melanomas *in vivo*, which encourages the use of LLP2A as a theranostic platform towards translation for use in patient care.

To extend ^{64}Cu -LLP2A PET data towards the rational selection of ^{67}Cu -LLP2A TRT dosing in BPR α , longitudinal PET imaging was conducted for individualized TRT dosimetry. Subject- and timepoint-specific image segmentation of the tumor and other organs of interest were

performed such that Monte Carlo simulation of ^{64}Cu -LLP2A radiation transport within these ROIs could be converted to ^{67}Cu -LLP2A absorbed doses. The tumor prescribed dose eclipsed that of all other ROIs and was significantly greater than VLA-4-dense lymphatic organs (thymus, spleen; $p < 0.01$, bone marrow [femur]; $p < 0.001$). Encouragingly, tumor prescribed dose was approximately twice that of the kidneys ($p < 0.0001$). To elucidate differences in subject-specific Torch dosimetry and standardized phantom-based OLINDA, ^{64}Cu -LLP2A TIA coefficients from Torch were input into the OLINDA 25g mouse phantom (non-tumor) or tumor absorbed dose coefficients were scaled according to size relative to those within the OLINDA software. As expected, OLINDA suggested substantially lower tumor doses relative to Torch. For all other shared ROIs except the heart, lungs, and liver, OLINDA mean doses were also markedly lower. Therefore, relying on OLINDA predictions would call for increased administered activity, causing unnecessary toxicity. The mean Torch tumor prescribed dose estimate was converted to the administered activity necessary for 2.5 Gy tumor absorbed dose (700 μCi , 0.7 mCi). A preceding study with a ^{90}Y -labeled small molecule demonstrated optimal therapeutic efficacy in combination with ICI at this dose to 5 Gy tumor dose [98]. For comparison, a higher dose tier (1 mCi, sufficient for 4 Gy tumor absorbed dose) was also included.

Results from the therapy study show that 1 mCi ^{67}Cu -LLP2A + dual ICI best impedes tumor growth in BPR α , but this is undercut by the contradictory performance of the saline control, which is the next best alternative. There appears to be a slight survival duration improvement with the addition of dual ICI at both TRT dose levels, but differences in median survival are not significant. Male mice demonstrated improved resistance to tumor growth with TRT \pm ICI and longer survival with all conditions apart from 0.7 mCi TRT. CBC analyses demonstrate minimal deviation relative to saline in all groups and for all metrics of interest, but only several timepoints

were considered due to precipitous exit of animals in the 1.0 mCi TRT group due to tumor burden. To summarize, TRT + ICI at the therapy doses predicted from dosimetry has thus far shown some but not dramatic efficacy. Further optimization will be necessary but the combination is well-tolerated.

4.2 Summary of Challenges and Limitations

Although these preliminary results with this theranostic approach are intriguing and further investigation is warranted, challenges were encountered that limit the significance of this work somewhat. Regarding the BPR α model, the transduction of the α_4 subunit inherently resulted in variability of intact VLA-4 expression, and this may not replicate the VLA-4 density or cell surface copy number of clinical melanomas. Although a genetic model of BRAF^{V600E} VLA-4⁺ melanoma would be preferable, to our knowledge these are not yet available. Further, transduced BPR α clones were first isolated with flow cytometry rather than with antibiotic selection, and genetic drift may have occurred to cause a reduction in VLA-4 expression. For downstream studies, BPR α should be re-selected or established as a stably transfected line such that observations are reliable. As a result of VLA-4 expression, BPR α should display increased aggressiveness versus BPR, but their growth kinetics have not been systematically evaluated *in vivo*.

A significant challenge in this work was the creation of accurate ROI contours generated in VivoQuant and their translation for analysis in Torch. As each mouse image set was contoured manually, the fidelity of the drawn ROIs is limited by the resolution of the images, generally the CT. This results in variability within the same mouse across time (Appendix B). Atlas-based semiautomatic image segmentation is available in VivoQuant but requires reference images with

matching ROIs. The new images and ROIs are registered to the reference images, with voxel-by-voxel classification for each voxel as part of a ROI if they fall within the probability threshold selected by the user. Future studies could validate manual segmentation followed by atlas segmentation for longitudinal imaging against purely manual segmentation. Emerging automated deep learning techniques for CT analysis have outperformed atlas-based segmentation [213], but these are not yet widely available in commercial software. The Torch workflow requires the creation of ‘plan ROIs’, which are aligned across time for a particular mouse. However, before performing calculations utilizing the plan ROIs, non-overlapping regions are eliminated. This can markedly reduce ROI size, particularly for small ROIs where LLP2A can accumulate (ex. thymus, bone marrow). This issue was circumvented with a summed single-timepoint dosimetry approach per mouse, which accounts only for radionuclide decay and not time-dependent clearance. The integrated activity per timepoint was determined, converted to dose rate, and summed by trapezoidal integration. As such, pharmacokinetic data that may have improved the quality of the prediction is not considered. The next version of Torch will allow for this mean dose rate integration directly without the need to make plan ROIs.

There are also notable limitations with the therapy study and the disease model. Inoculation of tumor cells into syngeneic mice as done here may establish pre-existing immunity that is essential to a response to combined radiation therapy and ICI [214]. Should a similar effect be observed in a spontaneous VLA-4^{hi} melanoma model, this would encourage clinical translation of the combination. The therapy study does not contain single ICI treatment groups, so the relative contribution of anti-CTLA-4 and anti-PD-L1 cannot be determined. Although anti-CTLA-4 + anti-PD-L1 is the current clinical standard of care for metastatic melanoma, the benefit of dual compared to single may depend on the immunogenicity of the tumor model and perhaps the

radioisotope. We have previously shown significant improvement in survival with anti-CTLA-4 + anti-PD-L1 versus anti-PD-L1 alone even prior to addition of ^{177}Lu -LLP2A in B16F10 [78]. Yet Patel *et al* observed no improvement in survival or tumor regression with the addition of anti-PD-L1 to a ^{90}Y -labeled small molecule + anti-CTLA-4 in B78 melanoma [98]. B16F10 and B78 share the same ancestral cell line [215] and both are considered poorly immunogenic. For optimal priming in combination with ICI, radionuclide half-life and tracer retention time are essential factors such that a TRT-stimulated immune response occurs with limited toxicity to incoming TILs. Characterization of the immune cell infiltrate and the expression of immune checkpoint and STING-associated markers in the TME are planned. Due to time restrictions, histology results from TRT with and without ICI are not reported here, although these studies will be included in a future publication of this work.

4.3 Future Directions

Future work in the near-term will include toxicology assessment of the combination therapy and dosing optimization of ^{67}Cu -LLP2A with the updated Torch software. To benchmark actual tumor dose delivery from dosimetry, OLINDA and Torch predictions for a supposed 1 and 4 Gy absorbed dose can be compared to what tumors actually receive by implanting a thermoluminescent dosimeter on the tumor. Later, the combination will be tested in a metastatic melanoma model and further investigation of the immune mechanisms underlying the combination of TRT and ICI will occur. Histology will be performed for ^{67}Cu -LLP2A at both dose tiers with and without dual ICI, with tissues (kidney, bone marrow, spleen, intestines, liver) harvested at several timepoints post-TRT, concluding at 35d post-injection. Prescribed dose estimates with

mean dose rate integration incorporated into Torch software will be compared to those previously determined with the revised methods described previously to ensure limited deviation in the true tumor absorbed dose.

To observe immunomodulation induced by ^{67}Cu -LLP2A alone, in future studies in the Anderson Lab, the tumor immune cell infiltrate will be examined at various timepoints post-injection for each dose tier with flow cytometry. Populations of interest include total immune cells (CD45^+), total myeloid cells (CD11b^+), regulatory ($\text{CD4}^+ \text{CD25}^+ \text{Foxp3}^+$) and effector (CD8^+) T cells, as well as dendritic cells ($\text{CD103}^+ \text{DEC205}^+$), among others. Expression of both PD-1 and PD-L1 on immune cells will also be measured. To correlate TME immune cell populations to antitumor activity and radiotoxicity, the post-radiation cytokine milieu will be characterized. A multiplex bead-based assay will be used to probe the concentration of a panel of cytokines and chemokines associated with the immune/inflammatory response from tumor lysates. These values will be compared to cold LLP2A as well as to ^{67}Cu -LLP2A with ICI. Given the phenotypic heterogeneity that can exist in multifocal melanoma [216], an *in situ* vaccination effect with ^{67}Cu -LLP2A + ICI for tumors with varying VLA-4 expression could be evaluated with a dual BPR-BPR α tumor model (LLP2A does not bind BPR). Another intriguing offshoot would be to evaluate any benefit of concomitant (TRT and ICI separated by 1 day) rather than sequential TRT + ICI, as previously demonstrated in a preclinical colorectal cancer model [49], as well as the associated immune correlates. Future studies could also investigate the same dosimetric approach but with other theranostic pairs such as terbium-155 (γ emissions for SPECT)/terbium-161 (β^- and Auger emission), as well as high LET α -emitters alone (actinium-225) or as part of a pair (lead-203 for SPECT/lead-212). Different therapy isotopes and for α -emitters, their progeny, may induce distinct immunological effects upon tumor cells and/or within the TME. Furthermore, emerging clinical

studies with EBRT demonstrate that greater radiation doses to circulating immune cells, as quantified via multifactorial effective dose to immune cells (EDIC), is associated with poorer overall survival and tumor control prognoses [217, 218]. However, whether this is applicable to TRT and the role of the radioisotope are yet to be explored.

Appendix A ^{64}Cu -LLP2A Imaging in BPR and BPR α Tumor Models

Appendix A.1 Materials and Methods

Appendix A.1.1 Reagents

All chemicals were purchased from Sigma-Aldrich (St. Louis, MO) or Fisher Scientific (Waltham, MA), unless otherwise specified. Sieber amide resin (loading capacity: 0.68 mmol/g) and all fluorenylmethyloxy carbonyl (Fmoc) protected amino acids for the preparation of Cy3-LLP2A were purchased from ChemPep (Wellington, FL). Aqueous solutions were generated with ultrapure water (resistivity: 18.2 M Ω •cm). CB-TE1A1P-PEG₄-LLP2A was purchased from Auspep (Tullamarine, VIC, AU). Sulfo-Cyanine3 (Sulfo-Cy3) was purchased from Lumiprobe (Hallandale Beach, FL). Antibodies for flow cytometry were purchased from BioLegend (San Diego, CA). Copper-64 chloride ($T_{1/2}$ = 12.7 hours, β^+ ; 17.8%, E_{β^+max} = 656 keV, β^- , 38.4%, E_{β^-max} = 573 keV) was purchased from Washington University (St. Louis, MO) and the University of Wisconsin (Madison, WI).

Appendix A.1.2 Instrumentation

Analytical and semipreparative reversed-phase high-performance liquid chromatography (HPLC) were performed on a Waters 1525 Binary HPLC pump (Milford, MA) with a Waters 2489 UV–Vis detector and a model 106 Bioscan radioactivity detector (Bioscan Inc., Washington, DC). Nonradioactive compounds were purified on a semipreparative Jupiter C18 column (Phenomenex,

Torrance, CA). Radiochemistry reaction progress and purity were monitored by radio-HPLC (Agilent Technologies, Santa Clara, CA) with a Luna C18(2) column (Phenomenex, Torrance, CA). Radioactive biodistribution samples were counted with a PerkinElmer 2470 WIZARD² Automatic γ -counter (Waltham, MA). PET/CT data were acquired using an Inveon Preclinical Imaging Station (Siemens Medical Solutions, Knoxville, TN). Flow cytometry analysis was performed on a BD LSRFortessa (BD Biosciences, San Jose, CA) unless otherwise noted. Flow cytometry analysis was conducted with FCS Express 7 (De Novo Software, Pasadena, CA).

Appendix A.1.3 Radio-HPLC Procedure

To determine whether radiolabeling had reached completion, a volume of the ⁶⁴Cu-LLP2A stock sufficient for 80-100 μ Ci was added to radiolabeling buffer (0.5 M ammonium acetate pH 6.8) for HPLC analysis. The volume injected was $\leq 50 \mu$ L. The sample was separated on a reverse phase Luna C18(2) column (5 μ m, 4.6 x 150 mm) via a gradient elution. Mobile phases water (A) and acetonitrile (B), each with 0.1% trifluoroacetic acid were used at ratios: 0-2 min 100% A/0% B, and 2-12 min 10% A/90% B, at a flow rate of 2 mL/min. Prior to each run, the column pressure was allowed to equilibrate. The retention time for the labeled construct is approximately 6 min, whereas free ⁶⁴Cu elutes around 2 min.

Appendix A.1.4 Bichinchoninic Acid (BCA) Procedure for Protein Quantification

Following the internalization assay, cell pellets from each well were individually frozen at -20°C for 10 half-lives to allow for radioactivity to decay. For the assay, cell pellets were thawed at 37°C for 20 min to ensure solubility. The manufacturer (Thermo Fisher Scientific, Waltham,

MA) protocol for a microplate was followed. The working reagent was prepared by adding Reagent B to a 50x volume of Reagent A, both provided as part of a kit (Pierce BCA Protein Assay Kit). A standard curve for the extrapolation of protein content was established for bovine serum albumin (BSA, 0-250 $\mu\text{g/mL}$). Standards and samples were plated in triplicate (50 μL each) in 12-well plates, and 200 μL of the working reagent was added to each well and triturated. The plates were placed in a cell culture incubator at 37°C for 10 min, then allowed to cool to room temperature for 20 min. The reaction product has a strong characteristic absorbance at 562 nm, which was read with a plate reader (BioTek Synergy H1, BioTek, Winooski, VT). Values were background - subtracted for protein content extrapolation and the activity was corrected for decay.

Appendix A.2 Results

Appendix A.2.1 Control Conditions of ^{64}Cu -LLP2A Internalization Experiment

To demonstrate that SDS detergent effectively removed bound but non-internalized LLP2A from the cell surface, a condition without SDS treatment was included ('No Strip') in the internalization assay (Figure 32). BPR shows no reduction compared to any condition that includes activity, whereas there is a marked reduction in internalized activity for BPR α and B16F10. This observation also indicates the necessity of intact VLA-4 for LLP2A internalization, as there is no difference in BPR with or without SDS stripping ('Total Binding' versus 'No Strip'), unlike for VLA-4 $^{+}$ BPR α and B16F10.

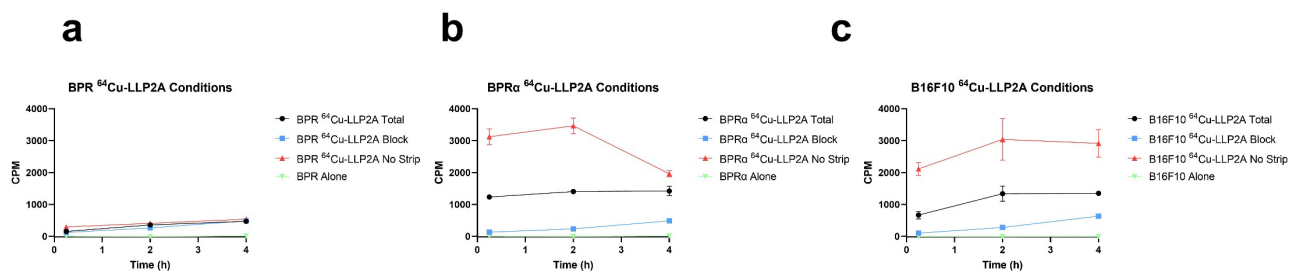


Figure 32 Timecourse of ^{64}Cu -LLP2A activity (counts per minute) internalization for all conditions tested in (a) BPR, (b) BPR α , and (c) B16F10 melanoma cells.

Appendix A.2.2 Biodistribution Timecourse in BPR α Tumors

Combining biodistribution results from several experiments (only the 24h data is presented in Chapter 2), it is unsurprising to see most LLP2A accumulation in the tumor and lymphatic organs (bone marrow, spleen, thymus) at 4h, with rapid washout (Figure 33). The actual values in percent activity per gram (%IA/g) are provided in Table 4. The tracer clears from all organs over time apart from the kidneys; at 48h, there is both a non-statistical outlier and a higher-than-expected value. This variation highlights the potential for substantial physiological differences even within a genetically homogenous population, underscoring the importance of individual dosimetry.

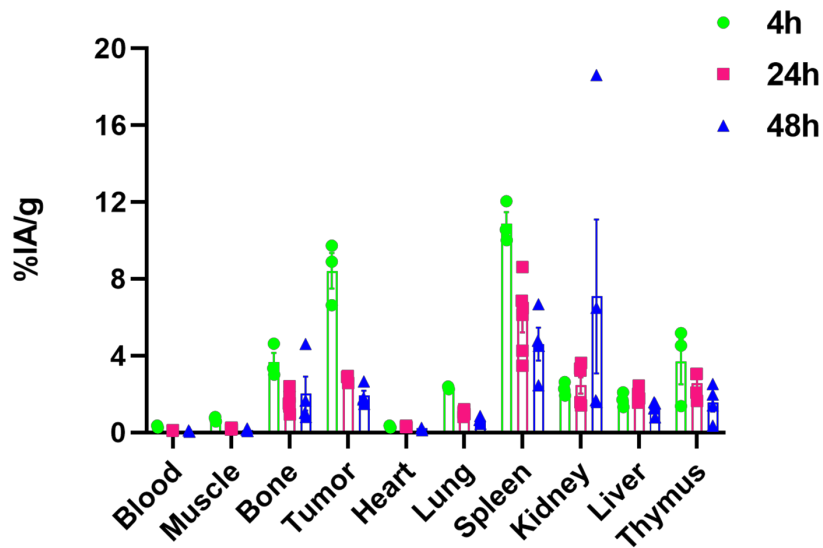


Figure 33 Merged *ex vivo* biodistribution of ^{64}Cu -LLP2A in mice bearing BPR α tumors at 4h (n=3), 24h (n=5-6), and 48h (n=4) post-injection. Values shown are mean \pm SEM.

Table 4 *Ex vivo* biodistribution values for ^{64}Cu -LLP2A in mice bearing BPR α tumors at 4, 24, and 48h post-injection.

%IA/g \pm SEM for ^{64}Cu -LLP2A			
	4h ^a	24h ^b	48h ^c
Blood	0.3 \pm 0.03	0.1 \pm 0.02	0.1 \pm 0.03
Muscle	0.7 \pm 0.07	0.2 \pm 0.04	0.1 \pm 0.03
Bone	3.7 \pm 0.5	1.6 \pm 0.5	2.0 \pm 0.9
Tumor	8.4 \pm 0.9	2.8 \pm 0.2	1.9 \pm 0.3
Heart	0.3 \pm 0.04	0.3 \pm 0.03	0.2 \pm 0.03
Lung	2.3 \pm 0.04	1.0 \pm 0.1	0.6 \pm 0.08
Spleen	10.9 \pm 0.6	6.0 \pm 1.9	4.6 \pm 0.9
Kidney	2.3 \pm 0.2	2.5 \pm 1.0	7.1 \pm 4.0
Liver	1.7 \pm 0.2	2.0 \pm 0.3	1.3 \pm 0.2
Thymus	3.7 \pm 1.2	4.2 \pm 4.0	1.6 \pm 0.5

^a: n=4, ^b: n=5-6, and ^c: n=4

Appendix A.2.3 Comparison of ^{64}Cu -LLP2A Tumor-to-Muscle Standard Uptake Value Ratios in BPR α versus Previously Reported Values for B16F10

As we observed differences in binding metrics and internalization in BPR α relative to values our laboratory has previously reported for B16F10, those B16F10 tumor-to-muscle SUV ratios were compared to those from our compiled studies with BPR α . B16F10 uptake is markedly faster, but uptake is comparable by 24h.

Table 5 Comparison of ^{64}Cu -LLP2A tumor-to-muscle standard uptake value ratios in mice bearing syngeneic B16F10 or BPR α tumors at 4 and 24h post-injection

Tumor-to-Muscle (Uninvolved Gastrocnemius) Standard Uptake Value Ratios (SUVr) for ^{64}Cu-LLP2A		
	4h	24h
B16F10^a	19.0 \pm 2.1	18.6 \pm 1.4
BPRα^b	13.1 \pm 1.1	19.7 \pm 5.6

^a: n=3, taken from [77]. ^b: n=9

Appendix B Image-Guided $^{64/67}\text{Cu}$ -LLP2A Therapy in BPR α

Appendix B.1 Materials and Methods

Appendix B.1.1 Reagents

Copper-67 chloride ($T_{1/2} = 2.6$ days, β^- , 100%, mean β^- energy: 141 keV, $E_{\beta\text{-max}} = 562$ keV, γ : 93 keV (16%), 185 keV (49%)) was purchased from the Idaho Accelerator Center at Idaho State University (Pocatello, ID).

Appendix B.1.2 Instrumentation

Analytical HPLC was conducted using a Shimadzu LC-40D HPLC pump (Kyoto, JP) paired with a Shimadzu SPD-40 UV-Vis detector and a LabLogic Flow-RAM™ radio-HPLC detector (Tampa, FL). Radiolabeling and radiochemical purity was assessed with a semipreparative Jupiter C18 column (5 μm , 250 x 4.6 mm; Phenomenex, Torrance, CA) with peak integration performed in Shimadzu LabSolutions software. Biodistribution assay samples were counted with a PerkinElmer Wallac 1480 Wizard 3™ Automatic Gamma Counter (Waltham, MA). Contouring in VivoQuant 2021 and radiation transport Monte Carlo simulation in Torch were performed on a Dell Technologies (Round Rock, TX) Precision 5820 Tower Workstation (64-bit, 128 GB RAM, Intel Core i9 10900X 3.7 GHz processor) with a NVIDIA Quadro RTX 4000 graphics card (Santa Clara, CA).

Appendix B.1.3 Processing of PET/CT Images in VivoQuant

CT image data in IMG (.img) format were imported into VivoQuant 2021, and the PET image data in IMG format were appended. The CT and PET images were co-registered automatically (selected 'Rigid' and 'Fast'). As images were acquired with 4 mice in the bed, they were cropped to isolate a single mouse using the Crop tool. For analysis in Torch, the PET unit was converted from nCi/cc to Bq/mL via the Pre-Processing tool. The single-mouse CT and PET images were each exported in DICOM format (.dcm, single z slice per file) to be used in Torch.

Appendix B.1.4 Contouring Rules

Contouring boundaries from CT were guided by the labeled high resolution CT mouse scan available through IMAIOS (<https://www.imaios.com/en/vet-anatomy/mouse/mouse-whole-body>), a resource for anatomy and radiology education. Volumes were drawn by creating 2D boundaries every several slices on the transverse view in VivoQuant 2021, followed by interpolation in the software to fill the gaps and generate a 3D rendering. The rules used to standardize contouring are listed in Table 6. For use in Torch, all ROIs except the total body remainder (tumor excluded) were selected and exported together as a single file in 8-bit RAW format (unsigned byte). The total body remainder was contoured from the CT in a separate session but exported identically.

Table 6 Contouring Rules for each ROI

Tumor	Defined from CT, 'start' point to 'end point'
Spleen	Doesn't show on CT, contoured from PET, starts several slices after liver until narrowest point. PET range set per timepoint.
Thymus	From PET, starts in hot region where cervical vertebra and vertebral column clearest to diagonal on last slice before heart.
Liver	From CT, lobe first starts after heart reaches narrowest point, swells to fill majority of body cavity until about 4 slices before lungs no longer visible.
Kidneys (L + R)	Discerned from CT as best as possible, with PET adjusted to determine if it falls within boundary.
Heart	From CT, begins 3 slices after point where lower (left) lung first visible, extends to narrowest point (slice before where liver lobe first emerges). Thoracic duct is excluded as best as possible.
Femur	Drawn on CT, from where ilium ends to where femur bone 'coalesces' in left leg.
Lungs (L + R)	From CT, begins 3 slices after each void first visible to 2-3 slices before liver/viscera fills cavity. Accessory lobe included as part of R lung. Thoracic duct and thoracic aorta are excluded.
Gastrocnemius	From CT, drawn from knee to ankle, excludes bone.
Bladder	Readily apparent from CT
Total Body (Tumor Excluded)	For comparison to OLINDA, entire body from CT without the paws, tail, and tumor.

Appendix B.1.5 Torch Analysis Procedure

In the Torch ‘Image Import’ menu, the administration (injection) time was first input and DICOM CT files for an individual mouse at a single timepoint were imported, with Import Options ‘Denoise CT’ and ‘Remove Couch’ deselected. The corresponding DICOM PET files were imported, and the RAW ROIs were added with the ‘Add Indexed ROI Volume’ command (‘Invert X’ and ‘Invert Z’ boxes checked). For the assumption of purely physical decay, the scan time for both CT and PET were set to the time of injection + 1 min. Next, in the ‘Manage ROIs’ menu, the labels for the imported ROIs were corrected and were set as the plan ROIs (‘Create Plan ROIs’ button). Copper-67 was selected as the therapy isotope in the ‘Model Pharmacokinetics’ menu, time-activity curves were generated, and the curves were integrated with voxel scaling (‘Integrate Activity’ button, ‘Voxel Scaling’ radio button selected). The ^{67}Cu -LLP2A cumulative activity dose was calculated in the ‘Compute Dose’ menu (Dose Engine: Monte Carlo, End Criterion: Uncertainty, Uncertainty Goal: 2%). Once the simulation was complete, dose volume histograms (DVHs) were created for the specified injected activity in the ‘Evaluate’ menu. From the ROI DVHs, the mean activity (Gy) was extracted for external calculation of total absorbed activity by mean dose rate integration.

Appendix B.1.6 Mean Dose Rate Integration

Mean ^{67}Cu -LLP2A doses per ROI and per mouse at each timepoint calculated in Torch were multiplied by the ^{67}Cu decay constant λ (the inverse of the half-life) to determine the mean dose rate (MDR) at $t = 0$. For the mean dose rate at $t = \text{timepoint } n$, correction for the difference in imaging (^{64}Cu) and therapy (^{67}Cu) was conducted using the following equation:

$$MDR_{t=n} = MDR_{t=0} e^{\lambda_{Cu-64}t_n} e^{\lambda_{Cu-67}t_n}$$

Dose rate integration was performed with the trapezoidal-exponential method. The curve was approximated with five timepoint intervals: $t_0 - t_1$, $t_1 - t_2$, $t_2 - t_3$, $t_3 - t_4$, $t_4 - t_\infty$, where t_1 , t_2 , t_3 , and t_4 are 2, 4, 24, and 48h respectively. Within each interval except the last one, the dose rate activity (DRA) is:

$$DRA = (MDR_n + MDR_{n-1}) \frac{\Delta t}{2}$$

The final interval ($t_{48h} - t_\infty$) dose rate activity is:

$$DRA_{t_{48h} - t_\infty} = \frac{MDR_{t_{48h}}}{\lambda_{Cu-67}}$$

Finally, the dose rate activity per interval was summed to provide the total absorbed ^{67}Cu -LLP2A dose. The prescribed dose per ROI is the dose (Gy) per activity injected (MBq).

Appendix B.1.7 Radio-HPLC Procedure for ^{67}Cu -LLP2A

To assess radiochemical purity following the radiolabeling reaction, a volume of the ^{67}Cu -LLP2A stock corresponding to 20-25 μCi was added to radiolabeling buffer (0.5 M ammonium acetate pH 6.5) for HPLC analysis. The sample was separated via a gradient elution on a reverse phase Jupiter C18 column (5 μm , 250 x 4.6 mm; Phenomenex, Torrance, CA) with an injected volume of $\approx 25 \mu\text{L}$. Mobile phases water (A) and acetonitrile (B), each with 0.1% trifluoroacetic acid were used at ratios: 0-5 min 95% A/5% B, 5-20 min 5% A/95% B, and then a 5 min hold at

a flow rate of 1 mL/min. Prior to each run, the column pressure was allowed to equilibrate. The retention time for the labeled construct is approximately 15 min, whereas free ^{67}Cu elutes around 5 min.

Appendix B.2 Results

Appendix B.2.1 Characteristics of imaging test mice

Table 7 Imaged mouse characteristics

Mouse ID	Initial Body Weight (g)	Injected Activity (MBq)
M1	19.5	12.5
M3	27.6	11.7
M4	19.8	12.1

Appendix B.2.2 Activity Concentration of ^{64}Cu -LLP2A in Test Mice ROIs

To demonstrate the timecourse and variability of uptake and clearance in ROIs of interest per mouse, the mean activity concentration (% IA/g) was determined for each from ^{64}Cu -LLP2A PET images using VivoQuant software (Figure 34). All ROIs display similar patterns of uptake and time-dependent clearance, yet individual variation exists, most notably for M4 tumor uptake relative to the others.

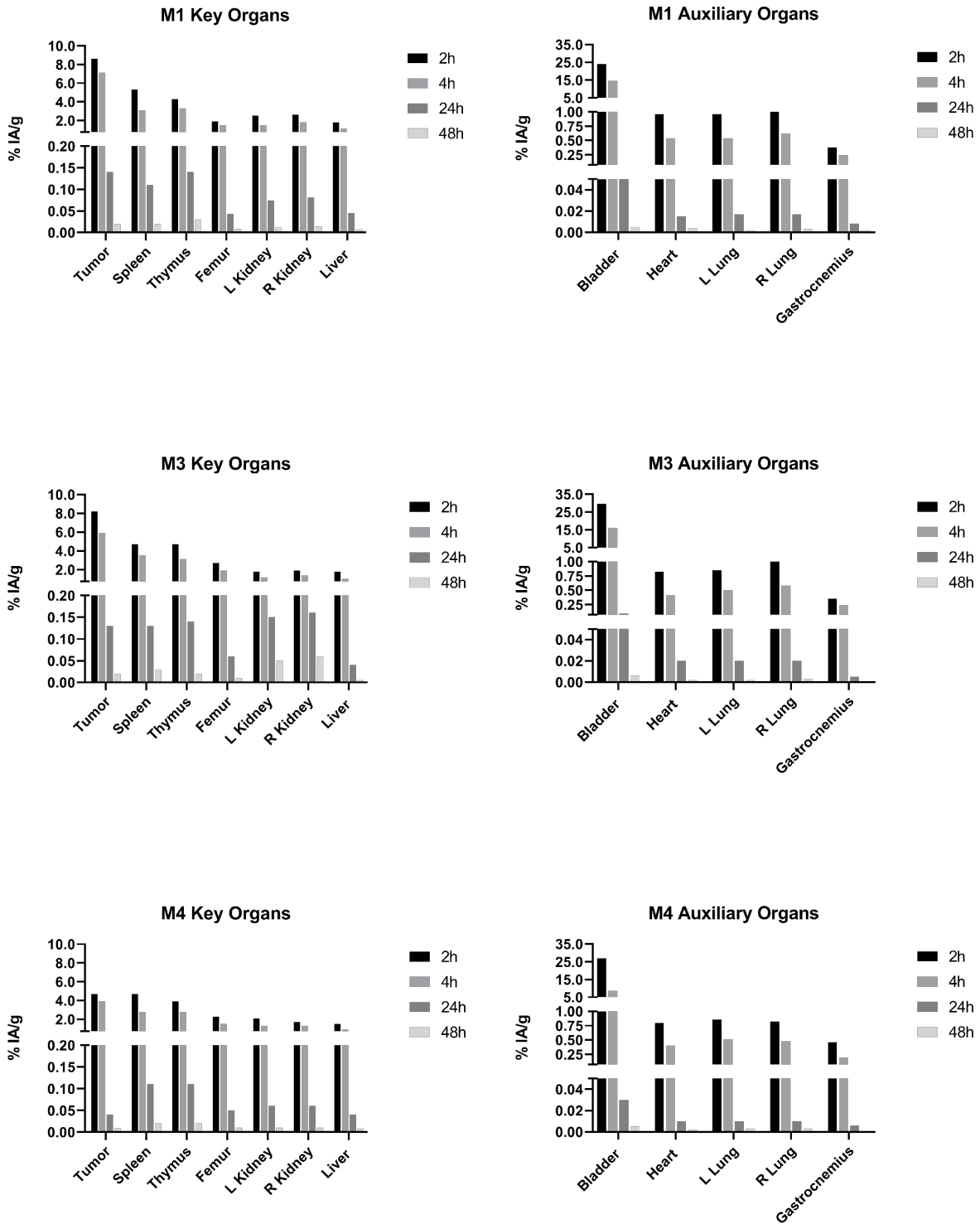
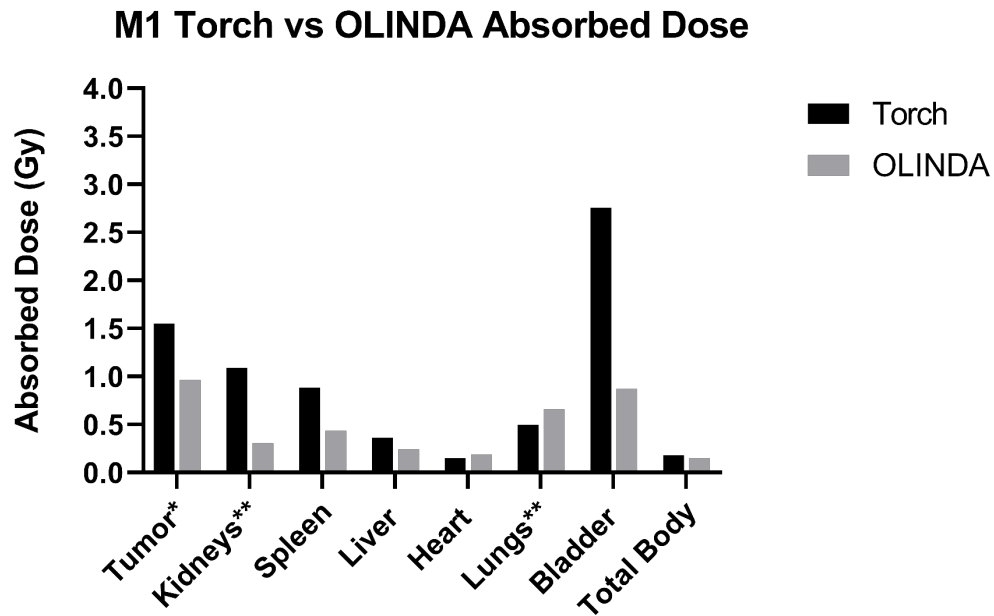


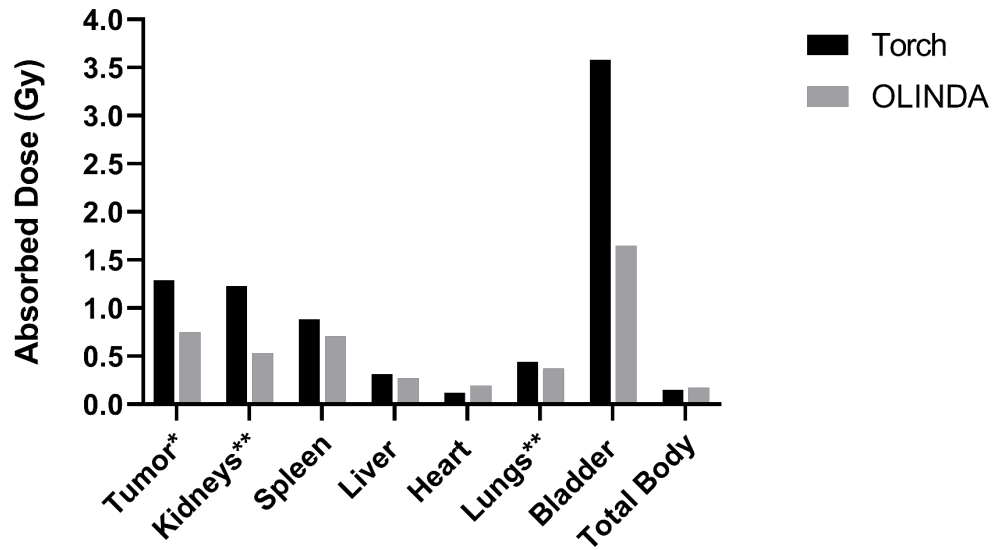
Figure 34 Timecourse of ^{64}Cu -LLP2A in ROIs from imaging for each of the test mice (M1, M3, M4). For the key organ plots, the bottom of the upper segment begins at 0.75. For the auxiliary organ plots, the top of the bottom segment is 0.05 and the bottom of the center segment is 0.07.

Appendix B.2.3 Mean ⁶⁷Cu-LLP2A Absorbed Dose Comparison of Torch and OLINDA in Test Mice

Following ⁶⁴Cu-LLP2A PET imaging, the individual mouse images were registered and ROIs were manually contoured. To visualize the differences in predicted absorbed dose the tumor and other ROIs experience for each software program, the values are plotted per mouse and per ROI (Figure 35).



M3 Torch vs OLINDA Absorbed Dose



M4 Torch vs OLINDA Absorbed Dose

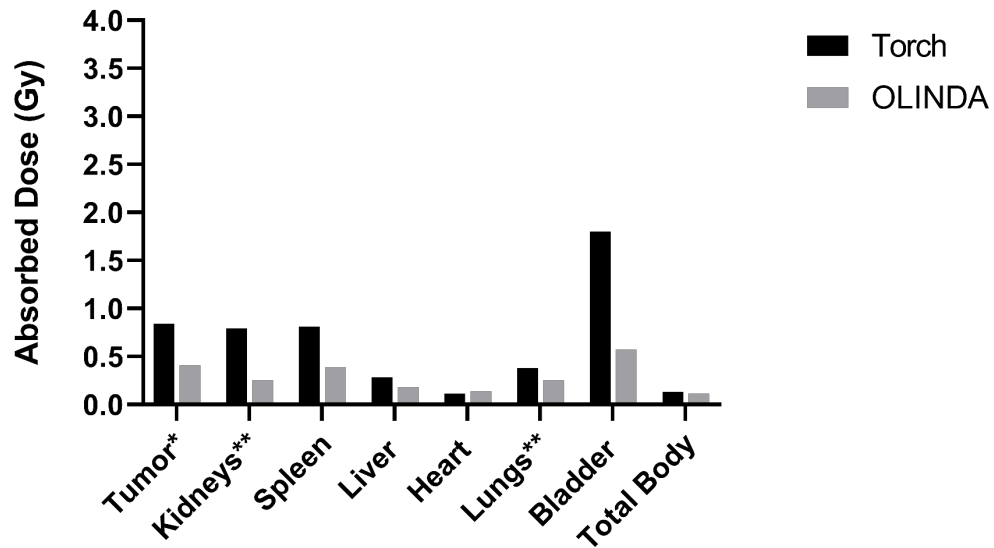


Figure 35 Absorbed ^{67}Cu -LLP2A doses in ROIs shared between Torch and the OLINDA MOBY 25g digital phantom for each of the test mice. *Tumor dose in OLINDA was calculated as the average of the sphere model doses for each of the tumor sizes across time, as determined from VivoQuant software. **Absorbed doses for the individual kidneys and lungs in Torch were summed.

Appendix B.2.4 Organ Masses in Torch and OLINDA

Table 8 Averaged Torch ROI masses (g) compared to those of the 25g OLINDA MOBY phantom

	M1	M3	M4	MOBY
Tumor	0.7	0.8	0.3	-
Kidneys	0.2	0.2	0.2	0.3
Spleen	0.05	0.1	0.1	0.1
Liver	0.4	0.4	0.3	1.7
Heart	0.2	0.3	0.2	0.2
Total Body (No Tumor)	17.9	25.9	18.2	24.1

Appendix B.2.5 Copper-67 Radiolabeling of LLP2A

⁶⁷Cu-LLP2A readily labeled LLP2A using similar conditions established for ⁶⁴Cu-LLP2A. The radiochemical purity of ⁶⁷Cu-LLP2A was routinely > 90% (Figure 36). The labeled construct elutes at approximately 15 min, with free ⁶⁷Cu eluting around 5 min. The two minor peaks around 17 min are caused by detection of emissions from nearby handling of activity during the run.

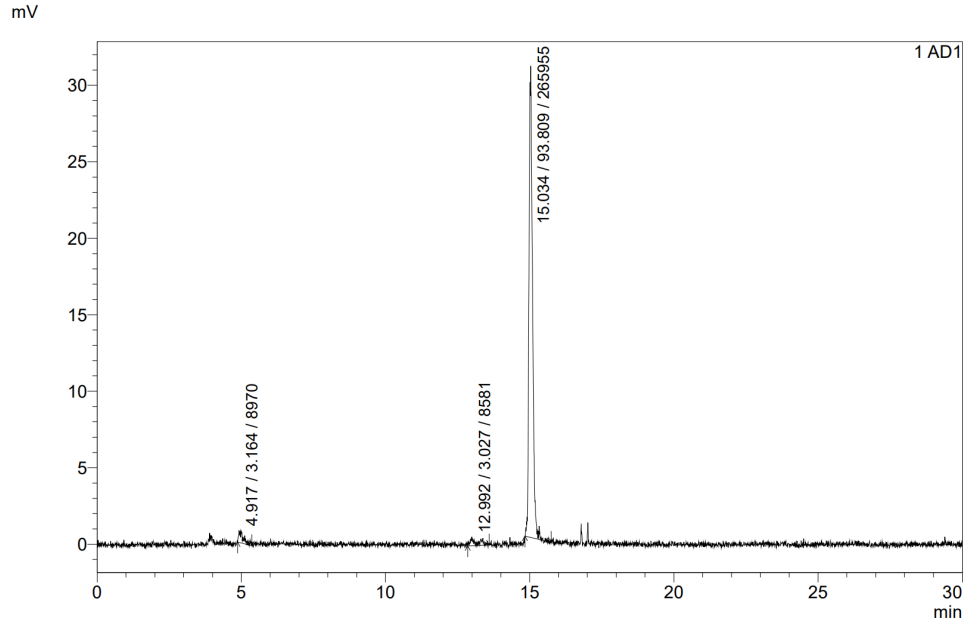


Figure 36 Representative radio-HPLC trace of ^{67}Cu -LLP2A. The first of the annotated numbers refers to the elution time in minutes, and the second is the percentage of the total signal per peak from baseline integration.

Appendix B.2.6 Comparison of $^{64/67}\text{Cu}$ -LLP2A Biodistribution and Torch Dosimetry

To better visualize disparities amongst the ^{64}Cu -LLP2A biodistribution, the predicted ^{67}Cu -LLP2A dosimetry from ^{64}Cu -LLP2A PET/CT, and the actual ^{67}Cu -LLP2A biodistribution, the three are compiled as Figure 37. Uptake per organ in both biodistributions are compared in Table 9.

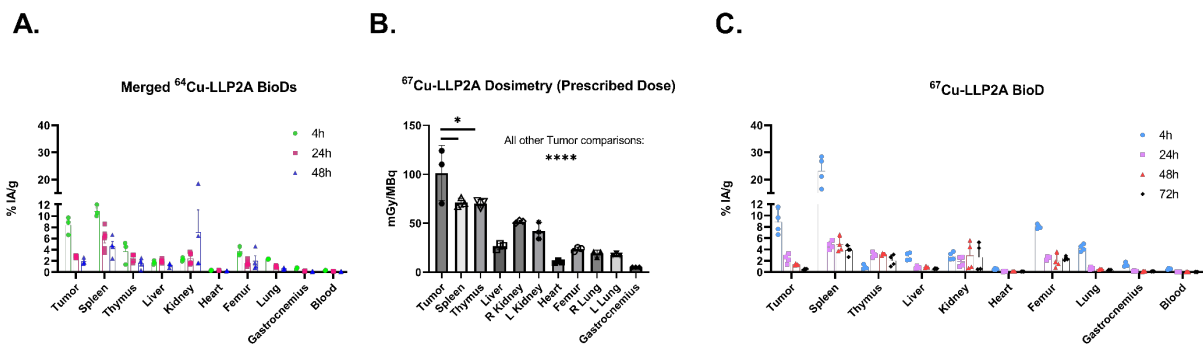


Figure 37 Combined ^{64/67}Cu-LLP2A biodistribution assays and predicted ⁶⁷Cu-LLP2A dosimetry. (A) Merged ⁶⁴Cu-LLP2A biodistribution data (4h: n = 4, 24h: n = 5-6, and 48h: n = 4). (B) Torch ⁶⁷Cu-LLP2A prescribed dose per ROI (n = 3, * p < 0.05, **** p < 0.0001, by one-way ANOVA). (C) ⁶⁷Cu-LLP2A biodistribution data with organs of interest matched to those of the prior ⁶⁴Cu-LLP2A biodistribution (Figure 33).

Table 9 Comparison of ^{64/67}Cu-LLP2A biodistribution results at 4, 24, and 48h post-injection.

	%IA/g ± SEM for ^{64/67} Cu-LLP2A					
	4h		24h		48h	
	⁶⁴ Cu-LLP2A ^a	⁶⁷ Cu-LLP2A	⁶⁴ Cu-LLP2A ^b	⁶⁷ Cu-LLP2A	⁶⁴ Cu-LLP2A ^c	⁶⁷ Cu-LLP2A
Blood	0.3 ± 0.03	0.6 ± 0.1	0.1 ± 0.02	0.04 ± 0.01	0.1 ± 0.03	0.05 ± 0.01
Muscle	0.7 ± 0.07	1.3 ± 0.2	0.2 ± 0.04	0.2 ± 0.04	0.1 ± 0.03	0.2 ± 0.03
Bone	3.7 ± 0.5	8.0 ± 0.2	1.6 ± 0.5	2.5 ± 0.1	2.0 ± 0.9	1.9 ± 0.6
Tumor	8.4 ± 0.9	8.9 ± 1.1	2.8 ± 0.2	2.4 ± 0.4	1.9 ± 0.3	1.4 ± 0.08
Heart	0.3 ± 0.04	0.5 ± 0.06	0.3 ± 0.03	0.1 ± 0.01	0.2 ± 0.03	0.1 ± 0.01
Lung	2.3 ± 0.04	4.3 ± 0.3	1.0 ± 0.1	0.6 ± 0.09	0.6 ± 0.08	0.5 ± 0.03
Spleen	10.9 ± 0.6	23.2 ± 2.8	6.0 ± 1.9	4.8 ± 0.4	4.6 ± 0.9	4.8 ± 0.7
Kidney	2.3 ± 0.2	2.9 ± 0.3	2.5 ± 1.0	1.9 ± 0.4	7.1 ± 4.0	3.0 ± 1.2
Liver	1.7 ± 0.2	2.7 ± 0.3	2.0 ± 0.3	0.8 ± 0.1	1.3 ± 0.2	0.9 ± 0.08
Thymus	3.7 ± 1.2	0.9 ± 0.2	4.2 ± 4.0	3.0 ± 0.2	1.6 ± 0.5	3.2 ± 0.1

^a: n = 4, ^b: n = 5-6, ^c: n = 4. For ⁶⁷Cu-LLP2A, n = 4 for all timepoints.

Bibliography

1. Bellavia, M.C., R.B. Patel, and C.J. Anderson, *Combined Targeted Radiopharmaceutical Therapy and Immune Checkpoint Blockade: From Preclinical Advances to the Clinic*. J Nucl Med, 2022. **63**(11): p. 1636-1641.
2. Bellavia, M.C., et al., *PET Imaging of VLA-4 in a New BRAF(V600E) Mouse Model of Melanoma*. Mol Imaging Biol, 2022. **24**(3): p. 425-433.
3. Baskar, R., et al., *Biological response of cancer cells to radiation treatment*. Frontiers in molecular biosciences, 2014. **1**: p. 24-24.
4. Barcellos-Hoff, M.H., C. Park, and E.G. Wright, *Radiation and the microenvironment - tumorigenesis and therapy*. Nat Rev Cancer, 2005. **5**(11): p. 867-75.
5. Postow, M.A., et al., *Immunologic correlates of the abscopal effect in a patient with melanoma*. N Engl J Med, 2012. **366**(10): p. 925-31.
6. Golden, E.B., et al., *An abscopal response to radiation and ipilimumab in a patient with metastatic non-small cell lung cancer*. Cancer immunology research, 2013. **1**(6): p. 365-372.
7. Abuodeh, Y., P. Venkat, and S. Kim, *Systematic review of case reports on the abscopal effect*. Curr Probl Cancer, 2016. **40**(1): p. 25-37.
8. Lawhn-Heath, C., et al., *Dosimetry in radionuclide therapy: the clinical role of measuring radiation dose*. Lancet Oncol, 2022. **23**(2): p. e75-e87.
9. Garske-Román, U., et al., *Prospective observational study of (177)Lu-DOTA-octreotate therapy in 200 patients with advanced metastasized neuroendocrine tumours (NETs): feasibility and impact of a dosimetry-guided study protocol on outcome and toxicity*. Eur J Nucl Med Mol Imaging, 2018. **45**(6): p. 970-988.
10. Violet, J., et al., *Dosimetry of (177)Lu-PSMA-617 in Metastatic Castration-Resistant Prostate Cancer: Correlations Between Pretherapeutic Imaging and Whole-Body Tumor Dosimetry with Treatment Outcomes*. J Nucl Med, 2019. **60**(4): p. 517-523.
11. Ellsworth, S.G., *Field size effects on the risk and severity of treatment-induced lymphopenia in patients undergoing radiation therapy for solid tumors*. Advances in radiation oncology, 2018. **3**(4): p. 512-519.
12. Wong, C.H., K.W. Siah, and A.W. Lo, *Estimation of clinical trial success rates and related parameters*. Biostatistics, 2018. **20**(2): p. 273-286.
13. Gill, M.R., et al., *Targeted radionuclide therapy in combined-modality regimens*. Lancet Oncol, 2017. **18**(7): p. e414-e423.
14. Sgouros, G., et al., *Radiopharmaceutical therapy in cancer: clinical advances and challenges*. Nature Reviews Drug Discovery, 2020. **19**(9): p. 589-608.

15. Das, T. and S. Banerjee, *Theranostic Applications of Lutetium-177 in Radionuclide Therapy*. Curr Radiopharm, 2016. **9**(1): p. 94-101.
16. Tarasov, V.A., et al., *Production of No-Carrier Added Lutetium-177 by Irradiation of Enriched Ytterbium-176*. Curr Radiopharm, 2015. **8**(2): p. 95-106.
17. Zimmermann, R.G., *Why are investors not interested in my radiotracer? The industrial and regulatory constraints in the development of radiopharmaceuticals*. Nucl Med Biol, 2013. **40**(2): p. 155-66.
18. Sahu, S.K., et al., *Intrathecal 5-[125I]iodo-2'-deoxyuridine in a rat model of leptomeningeal metastases*. J Nucl Med, 1997. **38**(3): p. 386-90.
19. Costantini, D.L., et al., *Antitumor effects and normal-tissue toxicity of 111In-nuclear localization sequence-trastuzumab in athymic mice bearing HER-positive human breast cancer xenografts*. J Nucl Med, 2010. **51**(7): p. 1084-91.
20. Ku, A., et al., *Auger electrons for cancer therapy – a review*. EJNMMI Radiopharmacy and Chemistry, 2019. **4**(1): p. 27.
21. Baidoo, K.E., K. Yong, and M.W. Brechbiel, *Molecular pathways: targeted α -particle radiation therapy*. Clin Cancer Res, 2013. **19**(3): p. 530-7.
22. Poty, S., et al., *α -Emitters for Radiotherapy: From Basic Radiochemistry to Clinical Studies-Part I*. J Nucl Med, 2018. **59**(6): p. 878-884.
23. Parker, C., et al., *Alpha emitter radium-223 and survival in metastatic prostate cancer*. New England Journal of Medicine, 2013. **369**(3): p. 213-223.
24. Morris, Z.S., A.Z. Wang, and S.J. Knox, *The radiobiology of radiopharmaceuticals*. Semin Radiat Oncol, 2021. **31**(1): p. 20-27.
25. Walicka, M.A., et al., *Survival and DNA damage in Chinese hamster V79 cells exposed to alpha particles emitted by DNA-incorporated astatine-211*. Radiat Res, 1998. **150**(3): p. 263-8.
26. Enger, S.A., et al., *Cross-fire doses from beta-emitting radionuclides in targeted radiotherapy. A theoretical study based on experimentally measured tumor characteristics*. Phys Med Biol, 2008. **53**(7): p. 1909-20.
27. Behling, K., et al., *Vascular Targeted Radioimmunotherapy for the Treatment of Glioblastoma*. J Nucl Med, 2016. **57**(10): p. 1576-1582.
28. White, J.M., F.E. Escorcia, and N.T. Viola, *Perspectives on metals-based radioimmunotherapy (RIT): moving forward*. Theranostics, 2021. **11**(13): p. 6293-6314.
29. Keinänen, O., et al., *Harnessing (64)Cu/(67)Cu for a theranostic approach to pretargeted radioimmunotherapy*. Proceedings of the National Academy of Sciences of the United States of America, 2020. **117**(45): p. 28316-28327.
30. Witzig, T.E., et al., *Randomized controlled trial of yttrium-90-labeled ibritumomab tiuxetan radioimmunotherapy versus rituximab immunotherapy for patients with relapsed or refractory low-grade, follicular, or transformed B-cell non-Hodgkin's lymphoma*. J Clin Oncol, 2002. **20**(10): p. 2453-63.

31. Kaminski, M.S., et al., *131I-tositumomab therapy as initial treatment for follicular lymphoma*. N Engl J Med, 2005. **352**(5): p. 441-9.
32. Sachpekidis, C., D.B. Jackson, and T.G. Soldatos, *Radioimmunotherapy in Non-Hodgkin's Lymphoma: Retrospective Adverse Event Profiling of Zevalin and Bexxar*. Pharmaceuticals (Basel), 2019. **12**(4).
33. Jain, R.K. and L.T. Baxter, *Mechanisms of heterogeneous distribution of monoclonal antibodies and other macromolecules in tumors: significance of elevated interstitial pressure*. Cancer Res, 1988. **48**(24 Pt 1): p. 7022-32.
34. van Osdol, W., K. Fujimori, and J.N. Weinstein, *An analysis of monoclonal antibody distribution in microscopic tumor nodules: consequences of a "binding site barrier"*. Cancer Res, 1991. **51**(18): p. 4776-84.
35. Song, H. and G. Sgouros, *Radioimmunotherapy of solid tumors: searching for the right target*. Curr Drug Deliv, 2011. **8**(1): p. 26-44.
36. Boerman, O.C., et al., *Pretargeted radioimmunotherapy of cancer: progress step by step*. J Nucl Med, 2003. **44**(3): p. 400-11.
37. Jallinoja, V.I.J. and J.L. Houghton, *Current Landscape in Clinical Pretargeted Radioimmunoimaging and Therapy*. Journal of Nuclear Medicine, 2021. **62**(9): p. 1200-1206.
38. Rondon, A., et al., *Pretargeted radioimmunotherapy and SPECT imaging of peritoneal carcinomatosis using bioorthogonal click chemistry: probe selection and first proof-of-concept*. Theranostics, 2019. **9**(22): p. 6706-6718.
39. Xenaki, K.T., S. Oliveira, and P.M.P. van Bergen en Henegouwen, *Antibody or Antibody Fragments: Implications for Molecular Imaging and Targeted Therapy of Solid Tumors*. Frontiers in Immunology, 2017. **8**.
40. Sachdeva, S., et al., *A Rational Approach for Creating Peptides Mimicking Antibody Binding*. Scientific Reports, 2019. **9**(1): p. 997.
41. Peng, L., et al., *Combinatorial chemistry identifies high-affinity peptidomimetics against alpha4beta1 integrin for in vivo tumor imaging*. Nat Chem Biol, 2006. **2**(7): p. 381-9.
42. Beaino, W., J.R. Nedrow, and C.J. Anderson, *Evaluation of (68)Ga- and (177)Lu-DOTA-PEG4-LLP2A for VLA-4-targeted PET Imaging and treatment of metastatic melanoma*. Molecular pharmaceuticals, 2015. **12**(6): p. 1929-1938.
43. Chen, H., et al., *Clinical application of radiolabeled RGD peptides for PET imaging of integrin $\alpha v \beta 3$* . Theranostics, 2016. **6**(1): p. 78-92.
44. Stott Reynolds, T.J., et al., *Characterization and evaluation of DOTA-conjugated Bombesin/RGD-antagonists for prostate cancer tumor imaging and therapy*. Nucl Med Biol, 2015. **42**(2): p. 99-108.
45. Hedhli, J., et al., *Synthesis, Chemical Characterization and Multiscale Biological Evaluation of a Dimeric-cRGD Peptide for Targeted Imaging of $\alpha v \beta 3$ Integrin Activity*. Scientific Reports, 2017. **7**(1): p. 3185.

46. Ogawa, K., et al., *Radiotheranostics Coupled between an At-211-Labeled RGD Peptide and the Corresponding Radioiodine-Labeled RGD Peptide*. ACS Omega, 2019. **4**(3): p. 4584-4591.
47. Zhang, J., et al., *Safety, pharmacokinetics, and dosimetry of a long-acting radiolabeled somatostatin analog (177)Lu-DOTA-EB-TATE in patients with advanced metastatic neuroendocrine tumors*. J Nucl Med, 2018. **59**(11): p. 1699-1705.
48. Däpp, S., et al., *PEGylation of (99m)Tc-labeled bombesin analogues improves their pharmacokinetic properties*. Nucl Med Biol, 2011. **38**(7): p. 997-1009.
49. Chen, H., et al., *Integrin $\alpha(v)\beta(3)$ -targeted radionuclide therapy combined with immune checkpoint blockade immunotherapy synergistically enhances anti-tumor efficacy*. Theranostics, 2019. **9**(25): p. 7948-7960.
50. Hausner, S.H., et al., *The Effects of an Albumin Binding Moiety on the Targeting and Pharmacokinetics of an Integrin $\alpha(v)\beta(6)$ -Selective Peptide Labeled with Aluminum [(18)F]Fluoride*. Mol Imaging Biol, 2020. **22**(6): p. 1543-1552.
51. Eychenne, R., et al., *Overview of Radiolabeled Somatostatin Analogs for Cancer Imaging and Therapy*. Molecules, 2020. **25**(17): p. 4012.
52. Sheppard, M., et al., *Metabolic Clearance and Plasma Half-Disappearance Time of Exogenous Somatostatin in Man**. The Journal of Clinical Endocrinology & Metabolism, 1979. **48**(1): p. 50-53.
53. Bodei, L., et al., *Radiolabeled Somatostatin Analogue Therapy Of Gastroenteropancreatic Cancer*. Semin Nucl Med, 2016. **46**(3): p. 225-38.
54. Esser, J.P., et al., *Comparison of [(177)Lu-DOTA(0),Tyr(3)]octreotate and [(177)Lu-DOTA(0),Tyr(3)]octreotide: which peptide is preferable for PRRT?* Eur J Nucl Med Mol Imaging, 2006. **33**(11): p. 1346-51.
55. Strosberg, J., et al., *Phase 3 Trial of 177Lu-Dotatate for Midgut Neuroendocrine Tumors*. New England Journal of Medicine, 2017. **376**(2): p. 125-135.
56. Strosberg, J., et al., *Health-Related Quality of Life in Patients With Progressive Midgut Neuroendocrine Tumors Treated With 177Lu-Dotatate in the Phase III NETTER-1 Trial*. Journal of Clinical Oncology, 2018. **36**(25): p. 2578-2584.
57. Bodei, L., et al., *Long-term tolerability of PRRT in 807 patients with neuroendocrine tumours: the value and limitations of clinical factors*. Eur J Nucl Med Mol Imaging, 2015. **42**(1): p. 5-19.
58. Reidy-Lagunes, D., et al., *Phase I Trial of Well-Differentiated Neuroendocrine Tumors (NETs) with Radiolabeled Somatostatin Antagonist (177)Lu-Satoreotide Tetraxetan*. Clin Cancer Res, 2019. **25**(23): p. 6939-6947.
59. Delpassand, E., et al., *First clinical experience using targeted alpha-emitter therapy with 212Pb-DOTAMTATE (AlphaMedix™) in patients with SSTR(+) neuroendocrine tumors*. Journal of Nuclear Medicine, 2019. **60**(supplement 1): p. 559-559.
60. Ballal, S., et al., *Survival Outcomes in Metastatic Gastroenteropancreatic Neuroendocrine Tumor Patients Receiving Concomitant 225Ac-DOTATATE-Targeted α -Therapy and*

- Capecitabine: A Real-World-Scenario Management-Based Long-Term Outcome Study.* Journal of Nuclear Medicine, 2023. **64**(2): p. 211-218.
61. Delpassand, E., et al., *Targeted alpha-emitter therapy with ²¹²Pb-DOTAMTATE in neuroendocrine tumor subjects who progressed following prior ¹⁷⁷Lu/90Y-PRRT.* Journal of Clinical Oncology, 2022. **40**(16_suppl): p. 4128-4128.
 62. Ballal, S., et al., *Broadening horizons with (225)Ac-DOTATATE targeted alpha therapy for gastroenteropancreatic neuroendocrine tumour patients stable or refractory to (177)Lu-DOTATATE PRRT: first clinical experience on the efficacy and safety.* Eur J Nucl Med Mol Imaging, 2020. **47**(4): p. 934-946.
 63. Ling, X., et al., *Preclinical dosimetry, imaging, and targeted radionuclide therapy studies of Lu-177-labeled albumin-binding, PSMA-targeted CTT1403.* Mol Imaging Biol, 2020. **22**(2): p. 274-284.
 64. El Fakiri, M., et al., *PSMA-Targeting Radiopharmaceuticals for Prostate Cancer Therapy: Recent Developments and Future Perspectives.* Cancers, 2021. **13**(16): p. 3967.
 65. Matthias, J., et al., *Cytoplasmic Localization of Prostate-Specific Membrane Antigen Inhibitors May Confer Advantages for Targeted Cancer Therapies.* Cancer Research, 2021. **81**(8): p. 2234-2245.
 66. Sartor, O., et al., *Lutetium-177-PSMA-617 for metastatic castration-resistant prostate cancer.* New England Journal of Medicine, 2021. **385**(12): p. 1091-1103.
 67. Kim, Y.J. and Y.I. Kim, *Therapeutic responses and survival effects of ¹⁷⁷Lu-PSMA-617 radioligand therapy in metastatic castrate-resistant prostate cancer: a meta-analysis.* Clin Nucl Med, 2018. **43**(10): p. 728-734.
 68. Current, K., et al., *Investigating PSMA-targeted radioligand therapy efficacy as a function of cellular PSMA levels and intratumoral PSMA heterogeneity.* Clinical Cancer Research, 2020. **26**(12): p. 2946-2955.
 69. Scott, A.M. and L. Bodei, *Pharmacogenomics in Radionuclide Therapy: Impact on Response to Theranostics.* J Nucl Med, 2021. **62**(7): p. 884-885.
 70. Stuparu, A.D., et al., *Mechanisms of Resistance to Prostate-Specific Membrane Antigen-Targeted Radioligand Therapy in a Mouse Model of Prostate Cancer.* J Nucl Med, 2021. **62**(7): p. 989-995.
 71. Zang, J., et al., *First-in-human study of (177)Lu-EB-PSMA-617 in patients with metastatic castration-resistant prostate cancer.* Eur J Nucl Med Mol Imaging, 2019. **46**(1): p. 148-158.
 72. Feurecker, B., et al., *Activity and adverse events of actinium-225-PSMA-617 in advanced metastatic castration-resistant prostate cancer after failure of lutetium-177-PSMA.* European Urology, 2021. **79**(3): p. 343-350.
 73. Sathekge, M., et al., *Predictors of overall and disease-free survival in metastatic castration-resistant prostate cancer patients receiving (225)Ac-PSMA-617 radioligand therapy.* J Nucl Med, 2020. **61**(1): p. 62-69.

74. Schadendorf, D., et al., *Association with clinical outcome of expression of VLA-4 in primary cutaneous malignant melanoma as well as P-selectin and E-selectin on intratumoral vessels*. J Natl Cancer Inst, 1995. **87**(5): p. 366-71.
75. Higgins, H.W., 2nd, et al., *Melanoma in situ: Part II. Histopathology, treatment, and clinical management*. J Am Acad Dermatol, 2015. **73**(2): p. 193-203; quiz 203-4.
76. Switzer, B., et al., *Managing Metastatic Melanoma in 2022: A Clinical Review*. JCO Oncology Practice, 2022. **18**(5): p. 335-351.
77. Beaino, W. and C.J. Anderson, *PET imaging of very late antigen-4 in melanoma: comparison of 68Ga- and 64Cu-labeled NODAGA and CB-TE1AIP-LLP2A conjugates*. J Nucl Med, 2014. **55**(11): p. 1856-63.
78. Choi, J., et al., *Combined VLA-4-targeted radionuclide therapy and immunotherapy in a mouse model of melanoma*. Journal of Nuclear Medicine, 2018. **59**(12): p. 1843-1849.
79. Anderson, C.J. and R. Ferdani, *Copper-64 radiopharmaceuticals for PET imaging of cancer: advances in preclinical and clinical research*. Cancer Biother Radiopharm, 2009. **24**(4): p. 379-93.
80. Ferdani, R., et al., *Synthesis, Cu(ii) complexation, 64Cu-labeling and biological evaluation of cross-bridged cyclam chelators with phosphonate pendant arms*. Dalton Transactions, 2012. **41**(7): p. 1938-1950.
81. Laforest, R., et al., *First-in-Human Evaluation of Safety and Dosimetry of (64)Cu-LLP2A for PET Imaging*. J Nucl Med, 2022.
82. Soodgupta, D., et al., *Ex Vivo and In Vivo Evaluation of Overexpressed VLA-4 in Multiple Myeloma Using LLP2A Imaging Agents*. J Nucl Med, 2016. **57**(4): p. 640-5.
83. Haddad, J., et al., *Molecular Imaging of Very Late Antigen-4 in Acute Lung Injury*. J Nucl Med, 2021. **62**(2): p. 280-286.
84. Perkins, L.A., et al., *Integrin VLA-4 as a PET imaging biomarker of hyper-adhesion in transgenic sickle mice*. Blood Adv, 2020. **4**(17): p. 4102-4112.
85. Sharma, P., et al., *The Next Decade of Immune Checkpoint Therapy*. Cancer Discovery, 2021. **11**(4): p. 838-857.
86. Sharma, P., et al., *Primary, adaptive, and acquired resistance to cancer immunotherapy*. Cell, 2017. **168**(4): p. 707-723.
87. Twyman-Saint Victor, C., et al., *Radiation and dual checkpoint blockade activate non-redundant immune mechanisms in cancer*. Nature, 2015. **520**(7547): p. 373-377.
88. Schoenfeld, A.J. and M.D. Hellmann, *Acquired Resistance to Immune Checkpoint Inhibitors*. Cancer Cell, 2020. **37**(4): p. 443-455.
89. Pilonis, K.A., et al., *Converging focal radiation and immunotherapy in a preclinical model of triple negative breast cancer: contribution of VISTA blockade*. Oncoimmunology, 2020. **9**(1): p. 1830524.
90. Deng, L., et al., *STING-dependent cytosolic DNA sensing promotes radiation-induced type I interferon-dependent antitumor immunity in immunogenic tumors*. Immunity, 2014. **41**(5): p. 843-52.

91. Golden, E.B., et al., *Radiation fosters dose-dependent and chemotherapy-induced immunogenic cell death*. *Oncoimmunology*, 2014. **3**: p. e28518.
92. Burnette, B.C., et al., *The efficacy of radiotherapy relies upon induction of type I interferon-dependent innate and adaptive immunity*. *Cancer Res*, 2011. **71**(7): p. 2488-96.
93. Lugade, A.A., et al., *Local radiation therapy of B16 melanoma tumors increases the generation of tumor antigen-specific effector cells that traffic to the tumor*. *J Immunol*, 2005. **174**(12): p. 7516-23.
94. Reits, E.A., et al., *Radiation modulates the peptide repertoire, enhances MHC class I expression, and induces successful antitumor immunotherapy*. *J Exp Med*, 2006. **203**(5): p. 1259-71.
95. Fujimoto, D., et al., *Alteration of PD-L1 expression and its prognostic impact after concurrent chemoradiation therapy in non-small cell lung cancer patients*. *Scientific Reports*, 2017. **7**(1): p. 11373.
96. Sato, H., et al., *DNA double-strand break repair pathway regulates PD-L1 expression in cancer cells*. *Nature Communications*, 2017. **8**(1): p. 1751.
97. Jagodinsky, J.C., et al., *Temporal analysis of type I interferon activation in tumor cells following external beam radiotherapy or targeted radionuclide therapy*. *Theranostics*, 2021. **11**(13): p. 6120-6137.
98. Patel, R.B., et al., *Low-dose targeted radionuclide therapy renders immunologically cold tumors responsive to immune checkpoint blockade*. *Sci Transl Med*, 2021. **13**(602): p. eabb3631.
99. Rouanet, J., et al., *Immune checkpoint inhibitors reverse tolerogenic mechanisms induced by melanoma targeted radionuclide therapy*. *Cancer Immunol Immunother*, 2020. **69**(10): p. 2075-2088.
100. Jiao, R., et al., *Evaluating the Combination of Radioimmunotherapy and Immunotherapy in a Melanoma Mouse Model*. *International journal of molecular sciences*, 2020. **21**(3): p. 773.
101. Malo, M.E., et al., *Mechanistic Insights into Synergy between Melanin-Targeting Radioimmunotherapy and Immunotherapy in Experimental Melanoma*. *International journal of molecular sciences*, 2020. **21**(22): p. 8721.
102. Lejeune, P., et al., *Immunostimulatory effects of targeted thorium-227 conjugates as single agent and in combination with anti-PD-L1 therapy*. *J Immunother Cancer*, 2021. **9**(10): p. e002387.
103. Foster, A., et al., *Novel theranostic agent for PET imaging and targeted radiopharmaceutical therapy of tumour-infiltrating immune cells in glioma*. *EBioMedicine*, 2021. **71**: p. 103571.
104. Gandini, S., D. Massi, and M. Mandalà, *PD-L1 expression in cancer patients receiving anti PD-1/PD-L1 antibodies: A systematic review and meta-analysis*. *Crit Rev Oncol Hematol*, 2016. **100**: p. 88-98.

105. Capitaio, M., et al., *Anti-tumor efficacy of PD-L1 targeted alpha-particle therapy in a human melanoma xenograft model*. *Cancers*, 2021. **13**(6): p. 1256.
106. Ren, J., et al., *PET imaging facilitates antibody screening for synergistic radioimmunotherapy with a ¹⁷⁷Lu-labeled α PD-L1 antibody*. *Theranostics*, 2021. **11**(1): p. 304-315.
107. Li, M., et al., *Targeted alpha-particle radiotherapy and immune checkpoint inhibitors induces cooperative inhibition on tumor growth of malignant melanoma*. *Cancers (Basel)*, 2021. **13**(15): p. 3676.
108. Czernin, J., et al., *Immune-checkpoint blockade enhances ²²⁵Ac-PSMA617 efficacy in a mouse model of prostate cancer*. *Journal of Nuclear Medicine*, 2021. **62**(2): p. 228-231.
109. Dabagian, H., et al., *PARP targeted alpha-particle therapy enhances response to PD-1 immune-checkpoint blockade in a syngeneic mouse model of glioblastoma*. *ACS Pharmacol. Transl. Sci*, 2021. **4**(1): p. 344-351.
110. Liu, S.-Z., *Nonlinear dose-response relationship in the immune system following exposure to ionizing radiation: mechanisms and implications*. *Nonlinearity in biology, toxicology, medicine*, 2003. **1**(1): p. 71-92.
111. Kasi, P.M., A. Sharma, and M.K. Jain, *Expanding the indication for novel theranostic ¹⁷⁷Lu-DOTATATE peptide receptor radionuclide therapy: proof-of-concept of PRRT in Merkel cell cancer*. *Case Reports in Oncology*, 2019. **12**(1): p. 98-103.
112. Ferdinandus, J., et al., *Response to combined peptide receptor radionuclide therapy and checkpoint immunotherapy with ipilimumab plus nivolumab in metastatic Merkel cell carcinoma*. *J Nucl Med*, 2022. **63**(3): p. 396-398.
113. Sharma, R., et al., *(⁶⁸Ga)-DOTATATE PET/CT parameters predict response to peptide receptor radionuclide therapy in neuroendocrine tumours*. *Radiother Oncol*, 2019. **141**: p. 108-115.
114. Lapa, C., et al., *Somatostatin receptor expression in small cell lung cancer as a prognostic marker and a target for peptide receptor radionuclide therapy*. *Oncotarget*, 2016. **7**(15): p. 20033-40.
115. Kim, C., et al., *Phase I study of the (¹⁷⁷Lu)-DOTA(0)-Tyr(3)-octreotate (lutathera) in combination with nivolumab in patients with neuroendocrine tumors of the lung*. *J. Immunother. Cancer*, 2020. **8**(2): p. e000980.
116. Prasad, V., et al., *First experiences with (¹⁷⁷Lu)-PSMA therapy in combination with pembrolizumab or after pretreatment with olaparib in single patients*. *J Nucl Med*, 2021. **62**(7): p. 975-978.
117. Antonarakis, E.S., et al., *Pembrolizumab for treatment-refractory metastatic castration-resistant prostate cancer: multicohort, open-label phase II KEYNOTE-199 study*. *J. Clin. Oncol.*, 2020. **38**(5): p. 395-405.
118. *ESMO 2021: PRINCE: interim analysis of the phase Ib study of ¹⁷⁷Lu-PSMA-617 in combination with pembrolizumab for metastatic castration resistant prostate cancer*. 2021 [cited 2021 October 31]; Available from: <https://www.urotoday.com/conference-highlights/esmo-2021/esmo-2021-prostate-cancer/132210-esmo-2021-577o-prince->

[interim-analysis-of-the-phase-ib-study-of-177lu-psma-617-in-combination-with-pembrolizumab-for-metastatic-castration-resistant-prostate-cancer-mcrpc.html](https://doi.org/10.1155/2017/16241631)

119. Kratochwil, C., et al., *Targeted α -therapy of metastatic castration-resistant prostate cancer with ^{225}Ac -PSMA-617: dosimetry estimate and empiric dose finding*. Journal of Nuclear Medicine, 2017. **58**(10): p. 1624-1631.
120. Tagawa, S.T., et al., *Phase I study of ^{225}Ac -J591 for men with metastatic castration-resistant prostate cancer (mCRPC)*. Journal of Clinical Oncology, 2021. **39**(15_suppl): p. 5015-5015.
121. Hammer, S., et al., *Preclinical Efficacy of a PSMA-Targeted Thorium-227 Conjugate (PSMA-TTC), a Targeted Alpha Therapy for Prostate Cancer*. Clin Cancer Res, 2020. **26**(8): p. 1985-1996.
122. Sartor, O., et al., *Effect of radium-223 dichloride on symptomatic skeletal events in patients with castration-resistant prostate cancer and bone metastases: results from a phase 3, double-blind, randomised trial*. Lancet Oncol, 2014. **15**(7): p. 738-46.
123. Choudhury, A.D., et al., *Randomized phase II study evaluating the addition of pembrolizumab to radium-223 in metastatic castration-resistant prostate cancer*. Journal of Clinical Oncology, 2021. **39**(6_suppl): p. 98-98.
124. Fong, L., et al., *A phase Ib study of atezolizumab with radium-223 dichloride in men with metastatic castration-resistant prostate cancer*. Clinical Cancer Research, 2021. **27**(17): p. 4746.
125. Sgouros, G., et al., *MIRD Commentary: Proposed Name for a Dosimetry Unit Applicable to Deterministic Biological Effects—The Barendsen (Bd)*. Journal of Nuclear Medicine, 2009. **50**(3): p. 485-487.
126. Wessels, B.W., et al., *MIRD pamphlet No. 20: the effect of model assumptions on kidney dosimetry and response--implications for radionuclide therapy*. J Nucl Med, 2008. **49**(11): p. 1884-99.
127. Stabin, M.G. and J.A. Siegel, *RADAR dose estimate report: a compendium of radiopharmaceutical dose estimates based on OLINDA/EXM version 2.0*. Journal of Nuclear Medicine, 2018. **59**(1): p. 154-160.
128. Dieudonné, A., et al., *Study of the impact of tissue density heterogeneities on 3-dimensional abdominal dosimetry: comparison between dose kernel convolution and direct Monte Carlo methods*. J Nucl Med, 2013. **54**(2): p. 236-43.
129. Marcatili, S., et al., *Model-based versus specific dosimetry in diagnostic context: comparison of three dosimetric approaches*. Med Phys, 2015. **42**(3): p. 1288-96.
130. Besemer, A.E., et al., *Development and validation of RAPID: a patient-specific Monte Carlo three-dimensional internal dosimetry platform*. Cancer Biother Radiopharm, 2018. **33**(4): p. 155-165.

131. Neira, S., et al., *Quantification of internal dosimetry in PET patients II: individualized Monte Carlo-based dosimetry for [18F]fluorocholine PET*. Med Phys, 2021. **48**(9): p. 5448-5458.
132. Seo, Y., et al., *Technical note: simplified and practical pretherapy tumor dosimetry - a feasibility study for (131) I-MIBG therapy of neuroblastoma using (124) I-MIBG PET/CT*. Medical physics, 2019. **46**(5): p. 2477-2486.
133. Bolch, W.E., et al., *MIRD Pamphlet No. 21: A Generalized Schema for Radiopharmaceutical Dosimetry—Standardization of Nomenclature*. Journal of Nuclear Medicine, 2009. **50**(3): p. 477-484.
134. Graves, S.A., R.T. Flynn, and D.E. Hyer, *Dose point kernels for 2,174 radionuclides*. Med Phys, 2019. **46**(11): p. 5284-5293.
135. Del Prete, M., et al., *Personalized (177)Lu-octreotate peptide receptor radionuclide therapy of neuroendocrine tumours: initial results from the P-PRRT trial*. Eur J Nucl Med Mol Imaging, 2019. **46**(3): p. 728-742.
136. Ilan, E., et al., *Dose response of pancreatic neuroendocrine tumors treated with peptide receptor radionuclide therapy using 177Lu-DOTATATE*. J Nucl Med, 2015. **56**(2): p. 177-82.
137. Lewandowski, R.J. and R. Salem, *Yttrium-90 radioembolization of hepatocellular carcinoma and metastatic disease to the liver*. Semin Intervent Radiol, 2006. **23**(1): p. 64-72.
138. Roosen, J., et al., *To 1000 Gy and back again: a systematic review on dose-response evaluation in selective internal radiation therapy for primary and secondary liver cancer*. Eur J Nucl Med Mol Imaging, 2021. **48**(12): p. 3776-3790.
139. Garin, E., et al., *Personalised versus standard dosimetry approach of selective internal radiation therapy in patients with locally advanced hepatocellular carcinoma (DOSISPHERE-01): a randomised, multicentre, open-label phase 2 trial*. The Lancet Gastroenterology & Hepatology, 2021. **6**(1): p. 17-29.
140. Hindorf, C., et al., *EANM Dosimetry Committee guidelines for bone marrow and whole-body dosimetry*. Eur J Nucl Med Mol Imaging, 2010. **37**(6): p. 1238-50.
141. Benua, R.S., et al., *The relation of radioiodine dosimetry to results and complications in the treatment of metastatic thyroid cancer*. Am J Roentgenol Radium Ther Nucl Med, 1962. **87**: p. 171-82.
142. Dorn, R., et al., *Dosimetry-guided radioactive iodine treatment in patients with metastatic differentiated thyroid cancer: largest safe dose using a risk-adapted approach*. J Nucl Med, 2003. **44**(3): p. 451-6.
143. Emami, B., et al., *Tolerance of normal tissue to therapeutic irradiation*. International Journal of Radiation Oncology*Biophysics, 1991. **21**(1): p. 109-122.
144. Bergsma, H., et al., *Nephrotoxicity after PRRT with (177)Lu-DOTA-octreotate*. Eur J Nucl Med Mol Imaging, 2016. **43**(10): p. 1802-11.

145. Cremonesi, M., et al., *Correlation of dose with toxicity and tumour response to (90)Y- and (177)Lu-PRRT provides the basis for optimization through individualized treatment planning*. Eur J Nucl Med Mol Imaging, 2018. **45**(13): p. 2426-2441.
146. Menda, Y., et al., *(90)Y-DOTATOC Dosimetry-Based Personalized Peptide Receptor Radionuclide Therapy*. J Nucl Med, 2018. **59**(11): p. 1692-1698.
147. Stabin, M.G. and J.A. Siegel, *Physical models and dose factors for use in internal dose assessment*. Health Phys, 2003. **85**(3): p. 294-310.
148. Grudzinski, J.J., et al., *The biological effectiveness of targeted radionuclide therapy based on a whole-body pharmacokinetic model*. Phys Med Biol, 2010. **55**(19): p. 5723-34.
149. Capala, J., et al., *Dosimetry for Radiopharmaceutical Therapy: Current Practices and Commercial Resources*. Journal of Nuclear Medicine, 2021. **62**(Supplement 3): p. 3S-11S.
150. Pasciak, A.S., A.C. Bourgeois, and Y.C. Bradley, *A Comparison of Techniques for (90)Y PET/CT Image-Based Dosimetry Following Radioembolization with Resin Microspheres*. Front Oncol, 2014. **4**: p. 121.
151. Hänscheid, H., et al., *Dose Mapping After Endoradiotherapy with (177)Lu-DOTATATE/DOTATOC by a Single Measurement After 4 Days*. J Nucl Med, 2018. **59**(1): p. 75-81.
152. Soret, M., S.L. Bacharach, and I. Buvat, *Partial-Volume Effect in PET Tumor Imaging*. Journal of Nuclear Medicine, 2007. **48**(6): p. 932-945.
153. Oh, S. and S. Kim, *Deformable image registration in radiation therapy*. Radiat Oncol J, 2017. **35**(2): p. 101-111.
154. Andersson, M., et al., *IDAC-Dose 2.1, an internal dosimetry program for diagnostic nuclear medicine based on the ICRP adult reference voxel phantoms*. EJNMMI Research, 2017. **7**(1): p. 88.
155. Voximetry. *Our Software* [cited 2022 December 19]; Available from: <https://voximetry.com/our-software/>.
156. Cavanaugh, J.E. and A.A. Neath, *The Akaike information criterion: Background, derivation, properties, application, interpretation, and refinements*. WIREs Computational Statistics, 2019. **11**(3): p. e1460.
157. Larsen, E.W. and D.R. Tolar. *A "Transport" Condensed History Method*. 2001. Berlin, Heidelberg: Springer Berlin Heidelberg.
158. Chauvin, M., et al., *OpenDose: Open-Access Resource for Nuclear Medicine Dosimetry*. J Nucl Med, 2020. **61**(10): p. 1514-1519.
159. Saginala, K., et al., *Epidemiology of Melanoma*. Med Sci (Basel), 2021. **9**(4).
160. Siegel, R.L., et al., *Cancer statistics, 2022*. CA: A Cancer Journal for Clinicians, 2022. **72**(1): p. 7-33.
161. Damsky, W.E., L.E. Rosenbaum, and M. Bosenberg, *Decoding melanoma metastasis*. Cancers (Basel), 2010. **3**(1): p. 126-63.

162. *Survival Rates for Melanoma Skin Cancer* [cited 2022 December 18]; Available from: <https://www.cancer.org/cancer/melanoma-skin-cancer/detection-diagnosis-staging/survival-rates-for-melanoma-skin-cancer-by-stage.html>.
163. Larkin, J., et al., *Five-Year Survival with Combined Nivolumab and Ipilimumab in Advanced Melanoma*. *New England Journal of Medicine*, 2019. **381**(16): p. 1535-1546.
164. Hodi, F.S., et al., *Combined nivolumab and ipilimumab versus ipilimumab alone in patients with advanced melanoma: 2-year overall survival outcomes in a multicentre, randomised, controlled, phase 2 trial*. *The Lancet Oncology*, 2016. **17**(11): p. 1558-1568.
165. Postow, M.A., et al., *Immunologic Correlates of the Abscopal Effect in a Patient with Melanoma*. *New England Journal of Medicine*, 2012. **366**(10): p. 925-931.
166. Ascierto, P.A., et al., *The role of BRAF V600 mutation in melanoma*. *J Transl Med*, 2012. **10**: p. 85.
167. Dummer, R., et al., *Overall survival in patients with BRAF-mutant melanoma receiving encorafenib plus binimetinib versus vemurafenib or encorafenib (COLUMBUS): a multicentre, open-label, randomised, phase 3 trial*. *The Lancet Oncology*, 2018. **19**(10): p. 1315-1327.
168. Flaherty, K.T., et al., *Combined BRAF and MEK inhibition in melanoma with BRAF V600 mutations*. *N Engl J Med*, 2012. **367**(18): p. 1694-703.
169. Kakadia, S., et al., *Mechanisms of resistance to BRAF and MEK inhibitors and clinical update of US Food and Drug Administration-approved targeted therapy in advanced melanoma*. *OncoTargets and therapy*, 2018. **11**: p. 7095-7107.
170. Gutzmer, R., et al., *Atezolizumab, vemurafenib, and cobimetinib as first-line treatment for unresectable advanced BRAF^{V600} mutation-positive melanoma (IMspire150): primary analysis of the randomised, double-blind, placebo-controlled, phase 3 trial*. *The Lancet*, 2020. **395**(10240): p. 1835-1844.
171. Ferrucci, P.F., et al., *KEYNOTE-022 part 3: a randomized, double-blind, phase 2 study of pembrolizumab, dabrafenib, and trametinib in BRAF-mutant melanoma*. *J Immunother Cancer*, 2020. **8**(2).
172. Kreft, S., et al., *Efficacy of PD-1-based immunotherapy after radiologic progression on targeted therapy in stage IV melanoma*. *Eur J Cancer*, 2019. **116**: p. 207-215.
173. Melnikova, V.O., et al., *Genomic alterations in spontaneous and carcinogen-induced murine melanoma cell lines*. *Oncogene*, 2004. **23**(13): p. 2347-2356.
174. Postow, M.A., et al., *Nivolumab and ipilimumab versus ipilimumab in untreated melanoma*. *N Engl J Med*, 2015. **372**(21): p. 2006-17.
175. Long, G.V., et al., *Overall Survival and Durable Responses in Patients With BRAF V600-Mutant Metastatic Melanoma Receiving Dabrafenib Combined With Trametinib*. *J Clin Oncol*, 2016. **34**(8): p. 871-8.
176. Wolchok, J.D., et al., *Overall Survival with Combined Nivolumab and Ipilimumab in Advanced Melanoma*. *The New England journal of medicine*, 2017. **377**(14): p. 1345-1356.

177. Ribas, A., et al., *Pembrolizumab versus investigator-choice chemotherapy for ipilimumab-refractory melanoma (KEYNOTE-002): a randomised, controlled, phase 2 trial*. The Lancet Oncology, 2015. **16**(8): p. 908-918.
178. Robert, C., et al., *Pembrolizumab versus ipilimumab in advanced melanoma (KEYNOTE-006): post-hoc 5-year results from an open-label, multicentre, randomised, controlled, phase 3 study*. Lancet Oncol, 2019. **20**(9): p. 1239-1251.
179. Holzmann, B., U. Gossler, and M. Bittner, *alpha 4 integrins and tumor metastasis*. Curr Top Microbiol Immunol, 1998. **231**: p. 125-41.
180. Hyun, Y.-M., et al., *Activated Integrin VLA-4 Localizes to the Lamellipodia and Mediates T Cell Migration on VCAM-1*. The Journal of Immunology, 2009. **183**(1): p. 359-369.
181. Yednock, T.A., et al., *Prevention of experimental autoimmune encephalomyelitis by antibodies against alpha 4 beta 1 integrin*. Nature, 1992. **356**(6364): p. 63-6.
182. Bastian, B.C., et al., *Chromosomal gains and losses in primary cutaneous melanomas detected by comparative genomic hybridization*. Cancer Res, 1998. **58**(10): p. 2170-5.
183. Cooper, Z.A., et al., *Response to BRAF Inhibition in Melanoma Is Enhanced When Combined with Immune Checkpoint Blockade*. Cancer Immunology Research, 2014. **2**(7): p. 643-654.
184. Close, D.A., et al., *Unbiased High-Throughput Drug Combination Pilot Screening Identifies Synergistic Drug Combinations Effective against Patient-Derived and Drug-Resistant Melanoma Cell Lines*. SLAS Discov, 2020: p. 2472555220970917.
185. Mattila, J.T., et al., *Positron Emission Tomography Imaging of Macaques with Tuberculosis Identifies Temporal Changes in Granuloma Glucose Metabolism and Integrin $\alpha 4 \beta 1$ -Expressing Immune Cells*. The Journal of Immunology, 2017. **199**(2): p. 806-815.
186. Grubbs, F.E., *Procedures for Detecting Outlying Observations in Samples*. Technometrics, 1969. **11**(1): p. 1-21.
187. Hughes, L.D., R.J. Rawle, and S.G. Boxer, *Choose Your Label Wisely: Water-Soluble Fluorophores Often Interact with Lipid Bilayers*. PLOS ONE, 2014. **9**(2): p. e87649.
188. Kuzu, O.F., et al., *Current State of Animal (Mouse) Modeling in Melanoma Research*. Cancer growth and metastasis, 2015. **8**(Suppl 1): p. 81-94.
189. Dankort, D., et al., *Braf(V600E) cooperates with Pten loss to induce metastatic melanoma*. Nat Genet, 2009. **41**(5): p. 544-52.
190. Tomasi, G. and L. Rosso, *PET imaging: implications for the future of therapy monitoring with PET/CT in oncology*. Current Opinion in Pharmacology, 2012. **12**(5): p. 569-575.
191. Krug, B., et al., *Role of PET in the Initial Staging of Cutaneous Malignant Melanoma: Systematic Review*. Radiology, 2008. **249**(3): p. 836-844.
192. Choi, E.A. and J.E. Gershenwald, *Imaging studies in patients with melanoma*. Surg Oncol Clin N Am, 2007. **16**(2): p. 403-30.
193. Larcos, G. and M.N. Maisey, *FDG-PET screening for cerebral metastases in patients with suspected malignancy*. Nucl Med Commun, 1996. **17**(3): p. 197-8.

194. Strobel, K., et al., *High-risk melanoma: accuracy of FDG PET/CT with added CT morphologic information for detection of metastases*. Radiology, 2007. **244**(2): p. 566-74.
195. Wong, A.N.M., et al., *The Advantages and Challenges of Using FDG PET/CT for Response Assessment in Melanoma in the Era of Targeted Agents and Immunotherapy*. European Journal of Nuclear Medicine and Molecular Imaging, 2017. **44**(1): p. 67-77.
196. Pyo, A., et al., *Ultrasensitive detection of malignant melanoma using PET molecular imaging probes*. Proceedings of the National Academy of Sciences, 2020. **117**(23): p. 12991-12999.
197. Xu, X., et al., *Synthesis and Preclinical Evaluation of (18)F-PEG(3)-FPN for the Detection of Metastatic Pigmented Melanoma*. Mol Pharm, 2017. **14**(11): p. 3896-3905.
198. Garg, P.K., et al., *4-(11)C-Methoxy N-(2-Diethylaminoethyl) Benzamide: A Novel Probe to Selectively Target Melanoma*. J Nucl Med, 2017. **58**(5): p. 827-832.
199. Vāvere, A.L., et al., *⁶⁴Cu-p-NH₂-Bn-DOTA-hu14.18K322A, a PET Radiotracer Targeting Neuroblastoma and Melanoma*. Journal of Nuclear Medicine, 2012. **53**(11): p. 1772-1778.
200. Voss, S.D., et al., *Positron emission tomography (PET) imaging of neuroblastoma and melanoma with ⁶⁴Cu-SarAr immunoconjugates*. Proc Natl Acad Sci U S A, 2007. **104**(44): p. 17489-93.
201. Norain, A. and E. Dadachova, *Targeted Radionuclide Therapy of Melanoma*. Semin Nucl Med, 2016. **46**(3): p. 250-9.
202. Klemke, M., et al., *High affinity interaction of integrin alpha4beta1 (VLA-4) and vascular cell adhesion molecule 1 (VCAM-1) enhances migration of human melanoma cells across activated endothelial cell layers*. J Cell Physiol, 2007. **212**(2): p. 368-74.
203. Bednarz, B., et al., *Murine-specific Internal Dosimetry for Preclinical Investigations of Imaging and Therapeutic Agents*. Health Physics, 2018. **114**(4): p. 450-459.
204. Marsh, I.R., et al., *Preclinical Pharmacokinetics and Dosimetry Studies of (124)I/(131)I-CLRI1404 for Treatment of Pediatric Solid Tumors in Murine Xenograft Models*. Journal of nuclear medicine : official publication, Society of Nuclear Medicine, 2019. **60**(10): p. 1414-1420.
205. Huang, S.Y., et al., *Patient-specific dosimetry using pretherapy [¹²⁴I]m-iodobenzylguanidine ([¹²⁴I]mIBG) dynamic PET/CT imaging before [¹³¹I]mIBG targeted radionuclide therapy for neuroblastoma*. Mol Imaging Biol, 2015. **17**(2): p. 284-94.
206. Bailey, D.L., et al., *⁶⁴Cu Treatment Planning and ⁶⁷Cu Therapy with Radiolabelled SARTATE (⁶⁴Cu/⁶⁷Cu]MeCOSAR-Octreotate) in Subjects with Unresectable Multifocal Meningioma – Initial Results for Human Imaging, Safety, Biodistribution and Radiation Dosimetry*. Journal of Nuclear Medicine, 2022: p. jnumed.122.264586.
207. Jiang, X., et al., *The Activation of MAPK in Melanoma Cells Resistant to BRAF Inhibition Promotes PD-L1 Expression That Is Reversible by MEK and PI3K Inhibition*. Clinical Cancer Research, 2013. **19**(3): p. 598-609.

208. Daud, A.I., et al., *Programmed Death-Ligand 1 Expression and Response to the Anti-Programmed Death 1 Antibody Pembrolizumab in Melanoma*. Journal of Clinical Oncology, 2016. **34**(34): p. 4102-4109.
209. Josefsson, A., et al., *Comparative Dosimetry for (68)Ga-DOTATATE: Impact of Using Updated ICRP Phantoms, S Values, and Tissue-Weighting Factors*. J Nucl Med, 2018. **59**(8): p. 1281-1288.
210. Besemer, A.E., et al., *Pretreatment CLR 124 Positron Emission Tomography Accurately Predicts CLR 131 Three-Dimensional Dosimetry in a Triple-Negative Breast Cancer Patient*. Cancer Biother Radiopharm, 2019. **34**(1): p. 13-23.
211. IAEA, *PET/CT Atlas on Quality Control and Image Artefacts*. 2014, Vienna: INTERNATIONAL ATOMIC ENERGY AGENCY.
212. Yu, J., et al., *Loss of MHC-I antigen presentation correlated with immune checkpoint blockade tolerance in MAPK inhibitor-resistant melanoma*. Frontiers in Pharmacology, 2022. **13**.
213. Chen, W., et al., *Deep learning vs. atlas-based models for fast auto-segmentation of the masticatory muscles on head and neck CT images*. Radiation Oncology, 2020. **15**(1): p. 176.
214. Crittenden, M.R., et al., *Tumor cure by radiation therapy and checkpoint inhibitors depends on pre-existing immunity*. Sci Rep, 2018. **8**(1): p. 7012.
215. García-Martín, A.B., et al., *VLA-4 mediated adhesion of melanoma cells on the blood-brain barrier is the critical cue for melanoma cell intercalation and barrier disruption*. J Cereb Blood Flow Metab, 2019. **39**(10): p. 1995-2010.
216. Rabbie, R., et al., *Multi-site clonality analysis uncovers pervasive heterogeneity across melanoma metastases*. Nat Commun, 2020. **11**(1): p. 4306.
217. Jin, J.Y., et al., *Higher Radiation Dose to the Immune Cells Correlates with Worse Tumor Control and Overall Survival in Patients with Stage III NSCLC: A Secondary Analysis of RTOG0617*. Cancers (Basel), 2021. **13**(24).
218. Xu, C., et al., *The impact of the effective dose to immune cells on lymphopenia and survival of esophageal cancer after chemoradiotherapy*. Radiother Oncol, 2020. **146**: p. 180-186.